Simulation Study for Measurement of CP violation in $B \to \textbf{charmonium} + K_S$ at KEK B-factory

DISSERTATION
Presented in Partial Fulfillment of the Requirements
for the Degree of Doctor of Science
in the Graduate School of Osaka University

Takeo Kawasaki
Osaka University
April 1999

Acknowledgment

First I would like to thank my advisor, Prof. Yorikiyo Nagashima, for his gentle support and supervising my education for high energy physics.

I am deeply thankful to Prof. T. Yamanaka, Dr. M. Takita, Dr. T. Hara, Dr. I. Suzuki and Dr. K. Trabelsi for answering many of my silly and boring questions on high energy physics experiment.

My thanks go to all the members to BELLE SVD and Tracking group for their generous cooperation. I am specially grateful to Prof. J. Haba, Dr. Y. Iwasaki, Dr. H. Tajima, Dr. H. Ozaki, Dr. T. Tsuboyama, Dr. M. Tanaka and Dr. Y. Yamada for their many helps and valuable suggestion.

I also greatly appreciate many discussions with Dr. Y. Tsujita, Mr. K. Sumisawa and Mr. J. Ryuko. They are sharing the hard work and gave me many suggestions for the development of SVD.

I owe thanks to my colleagues Mr. K. Adachi, Dr. K. Hanagaki, Mr. T. Tsuji and Dr. T. Yamaguchi for their kindness and friendship.

I am very much thankful to my colleagues Dr. M. Sadamoto, Mr. K. Senyo, Mr. S. Hidaka, Mr. M. Yoshida, Mr. K. Higuchi, Mr. T. Houjo, Mr. K. Kurebayashi, Mr. K. Mori, Mr. H. Yamada, Mr. K. Hara, Mr. K. Manabe, Mr. H. Miyake and Mr. K. Nitta. I enjoyed the life at the university with them.

I am very much indebted to Ms. S. Tsuzuki for her encouragement and helps.

At the last, I would like to express my special thanks to Dr. Masashi Hazumi, without whose supervision this thesis work wouldn't have finished. I have learnt so many things from him through long hours of discussion. I can't thank him enough for his kindness and useful instruction.

Abstract

The primary goal of KEK B-factory experiment is to observe CP asymmetry in B meson decays at e^+e^- collision at energy on $\Upsilon(4S)$ mass and to perform the test for Standard Model. The decay mode, $B \to$ charmonium$+K_S$, is expected to provide the best information to measure the angle ϕ_1 of the unitarity triangle with less theoretical uncertainty and a small experimental error. We used decay modes $B \to J/\psi K_S$, $B \to \psi(2S)K_S$, $B \to \chi_{c1}K_S$ and $B \to \eta_c K_S$. We performed a simulation of the experiment by treating Monte Carlo events as real data. The value of $\sin 2\phi_1$ and its statistical error were calculated with fitting the proper time distribution of B meson decays. In order to avoid the dependence on Monte Carlo simulation in the real experiment, a method was developed where we didn't use generator information but only reconstructed values. We also estimated systematic errors. Combining all the modes, we obtained 1255 events including 124 ± 17 estimated background events with integrated luminosity of 100fb^{-1} which is the designed annual luminosity. We obtained $\sin 2\phi_1 = 0.632^{+0.080}_{-0.081}(stat.)^{+0.047}_{-0.044}(sys.)$ for the input value of 0.60. With the result of the simulation, it is found that we can observe CP asymmetry with 3σ significance if the value of $\sin 2\phi_1$ is larger than 0.28 with 100fb^{-1}, which covers the entire allowed region given with the present indirect experimental results.

Contents

Chapter 1

Introduction

A major unresolved issue in our understanding of the universe is how the present universe, which is composed entirely of matter, evolved from the matter-antimatter-symmetric Big Bang. The laws of the nature have a high degree of symmetry between matter and antimatter. The excess of matter over antimatter is not an easily explained property of the universe. CP violation is a key piece in the puzzle of the matter dominance in the universe[1].

Since the first observation of CP violation in the neutral kaon system in 1964[2], an enormous amount of theoretical work has been done to try to understand the phenomenon. Many extensions of the Standard Model (SM)[3] have been proposed that incorporate CP violation, such as the multi-Higgs model[4], the left-right symmetry [5], the supersymmetry [6] and so on. In a remarkable paper published in 1973, Kobayashi and Maskawa (KM) noted that CP violation could be accommodated in the framework of the SM only if there were at least six quark flavors, twice the number of quark flavors known at that time[7]. The subsequent discoveries of c, b and t quarks have proven the six-quark KM hypothesis, and KM model for CP violation is now considered to be an essential part of the SM.

However, the KM scheme is not the only model that can accommodate the CP violation and in spite of a considerable amount of experimental effort over the past three decades, there remain other theoretical proposals that are consistent with presently-available experimental data.

In 1980, Sanda and Carter pointed out that the KM model contained the possibility of rather sizable CP violating asymmetries in certain decay modes of the B mesons[8]. The observation of a CP violation in B meson decays would be a confirmation of the KM model. The key to the test of the SM is the measurement of the "unitarity triangle" which shows relations between the KM matrix elements. The KM model provides definitive predictions for three CP angles, ϕ_1, ϕ_2, ϕ_3, which can be extracted from measurements of different CP asymmetries.

The largest observable effects are expected to show up in the difference of the decay rates between B^0 and $\bar{B}^0$ mesons to the same CP eigenstate. Therefore measurements of CP asymmetries using $B^0\bar{B}^0$ pairs from $\Upsilon(4S)$ decays must be derived from comparisons of the time evolution of the B^0 and $\bar{B}^0$ decays, rather than from time-integrated asymmetries[1]. The most favorable experimental situation is the asymmetric e^+e^- storage ring at the $\Upsilon(4S)$ resonance[9]. This would boost the decaying B^0 mesons in the laboratory frame, allowing existing vertex measurement technology to measure the time order of $B^0\bar{B}^0$ decay pairs, even with the short B

[1] The $B^0\bar{B}^0$ pair from $\Upsilon(4S)$ has C=odd state. If one integrates over all decay time, CP asymmetry vanishes. At C=even state, for exsample $\Upsilon(5S) \rightarrow BB^*$, CP asymmetry can be observed even if decay time is integrated. CP asymmetry is, However, diluted by factor $2x/(1+x^2)^2$, where $x = \Delta m_B/\Gamma_B$.

meson flight distance. The proper time difference Δt is given by

$$\Delta t \simeq \Delta z / c\beta\gamma,$$

where $\beta\gamma$ is the Lorentz boost factor due to the asymmetric beam energy and Δz is the distance between the decay vertices of the two B mesons along the beam direction. In addition to the feasibility of the measurement of the proper time distribution, the asymmetric e^+e^- collider on $\Upsilon(4S)$ is expected to provide a large number of $B^0\bar{B}^0$ pairs, 10^7 or more. Hence it will become possible to obtain the sizable number of fully-reconstructed B decays into CP eigenstates each of that has a typical branching ratio of 10^{-5}.

KEK B-factory project is in preparation to achieve the goal specified above. The data taking is expected to start in 1999. The accelerator, referred to as KEKB, promises to provide the luminosity of $10^{34}\mathrm{cm}^{-2}\mathrm{s}^{-1}$ with asymmetric $\Upsilon(4S)$ production at a $\beta\gamma$ of 0.42 (8.0GeV/c electrons on 3.5 GeV/c positrons). In this condition, 10^8 $\Upsilon(4S)$ would be produced a year and the mean decay length of B meson would be $\sim 200\mu$m. It is therefore possible to measure the dependence of the CP asymmetry on the relative decay time of two B mesons, from which one can extract a precise measurement of the CP violating parameters in the KM matrix. For example in $B \to J/\psi K_S$, the asymmetry, A, is related to CP angle ϕ_1 as

$$A(\Delta t) = \frac{\Gamma(B^0(\Delta t) \to J/\psi K_S) - \Gamma(\bar{B}^0(\Delta t) \to J/\psi K_S)}{\Gamma(B^0(\Delta t) \to J/\psi K_S) + \Gamma(\bar{B}^0(\Delta t) \to J/\psi K_S)} = -\sin 2\phi_1 \sin(\Delta m_B \Delta t)$$

where Δt is the time difference of two B meson decay and Δm_B the mass difference of two CP eigenstates of B^0 meson. The resolution of vertex measurement directly affects the accuracy of CP angle measurement. A detector, referred to as BELLE, must be capable of high efficiency reconstruction of extremely rare exclusive final states of B mesons in the presence of combinatoric and accelerator-generated beam backgrounds. This requirement places a premium on solid angle coverage, charged particle momentum resolution and species identification, and photon resolution and detection efficiency. In particular, since BELLE detector must provide precision proper time of B meson decays, Silicon Vertex Detector (SVD) is essential to have a resolution better than $\tau_B/2$, corresponding to a 100 μm resolution for the vertex difference.

Among the three CP angles of unitarity triangle, ϕ_1 is expected to be the most accessible experimentally, and one of the primary goals of B-factory experiment. $B \to J/\psi K_S$ is generally considered to be the cleanest channel for measuring ϕ_1. This is because of its final state, namely $l^+l^-\pi^+\pi^-$, is essentially background free, and its decay diagram is dominated by a single contribution, allowing a straightforward extraction of CP angle. In order to confirm in various decay modes and measure with smaller errors, we need to utilize other decay modes. To this end, it will be crucial to incorporate other similar decay modes such as, $B \to \psi(2S)K_S$, $B \to \chi_{c1}K_S$ and $B \to \eta_c K_S$, all of them provide alternative possibilities for measuring ϕ_1.

The importance of the research of CP violation in B decays is reflected in the number of laboratories. The BaBar[10] experiment at SLAC and the HERAB[11] experiment at DESY are in preparation with competitive schedules with BELLE. Other projects addressing this physics are also planned for the Tevatron collider[12] and have been proposed for LHC[13]. A goal of the BELLE experiment at the first stage is to be the first group to establish the CP violation in B decays.

In this thesis, we present a simulation study for the measurement of a time dependent CP asymmetry and the extraction of $\sin 2\phi_1$ for the decay mode, $B \to \mathrm{charmonium} + K_S$. We developed a experimental technique and estimated the accuracy of measurement of $\sin 2\phi_1$. The basic strategy of the simulation study is to treat generated events as if they were real data. The established chain of the processes will be applicable to real data. In order to justify the simulation , we also performed a test of SVD, which is the most crucial detector component for measurement of $\sin 2\phi_1$, with high energy test beam.

The outline of this thesis is as follows: Physics formalism for CP violation is given in Chapter 2. An overview of the experimental apparatus, KEKB accelerator and BELLE detector, is described in Chapter 3 with a detailed description of the silicon vertex detector (SVD). The testbeam experiment for SVD is given in Chapter 4. The result of this testbeam experiment was indispensable to determine the design of unit sensor of BELLE SVD. The details of software for Monte Carlo simulation are given in Chapter 5. In chapter 6, we describe the estimation of the overall performance of BELLE SVD with Monte Carlo simulation study. We estimated the vertex resolution for B decays and confirmed that the resolution is good enough to measure CP asymmetry in B decays. In Chapter 7, we describe the simulation study for CP violating mode. The event generation, reconstruction and selection technique are explained. Based on the study in Chapter 7, $\sin 2\phi_1$ is finally estimated in Chapter 8. We also evaluate the statistical and systematic errors for measurement of $\sin 2\phi_1$. Chapter 9 is devoted to discussion on the impact of $\sin 2\phi_1$ measurement at BELLE on the elementary particle physics. Finally, the conclusion of this thesis is given in Chapter 10.

Chapter 2

CP violation in B-decays

The violation of CP symmetry is one of the most interesting aspects of high-energy physics. Experimentally, it is one of the least tested properties of the Standard Model. This chapter explains the basic theory of CP violation in B decays and the measurement of the angles of the unitarity triangle. First of all, we explain the discovery of CP violation in K decays in Section 2.1. After describing phenomenology of CP violation in B decays in Section 2.2, we discuss the origin of CP violation and Kobayashi-Maskawa matrix in the framework of Standard Model in Section 2.3. The measurement of the angle, ϕ_1, of unitarity triangle with $B \to$ charmonium$+K_S$ is described in Section 2.4.

2.1 Discovery of CP Violation

2.1.1 P, C, and CP Transformation

In quantum theory, there are conservation laws corresponding to discrete transformations. One of these is reflection in space ("parity operation") **P**. Invariance of laws of nature under **P** means that the mirror image of an experiment yields the same result in its reflected frame of reference as the original experiment in the original frame of reference. This means that "left" and "right" cannot be defined in an absolute sense.

Similarly, the particle-antiparticle conjugation **C** transforms each particle into its antiparticle, by which all additive quantum numbers change their sign. **C** invariance of laws means that experiments in a world consisting mainly of antiparticles will give identical results to the ones in our world provided all names of particles are "anti" relative to ours.

A third transformation of this kind is time reversal **T**, which reverses momenta and angular momenta. This corresponds formally to an inversion of direction of time. According to the CPT theorem of Lüders and Pauli[14] there is a connection between these three transformations such that under rather weak assumptions in a local field theory all processes are invariant under the combined operation **CPT**.

For a long time it was assumed that all the elementary processes are also invariant under the application of each of the three operation **C**, **P**, and **T** separately. However, the work of Lee and Yang[15] questioned this assumption, and the subsequent experiments demonstrated the violation of **P** and **C** invariance in weak decays of nuclei and of pions and muons. At that time **CP** was still considered to be invariant, replacing the separate **P** and **C** invariance of weak interactions.

One consequence of this postulated CP invariance for the neutral K mesons was predicted by Gell-Mann and Pais: there should be a long-lived partner to known $V^0(K_1^0)$ particle of short lifetime(10^{-10} sec). According to this proposal these two particles are mixtures of two strangeness eigenstates, $K^0(S=+1)$ and $\bar{K}^0(S=-1)$ produced in strong interactions. Weak interactions do not conserve strangeness and the physical particles should be eigenstates of CP if the weak interactions are CP invariant. These eigenstates are(with $\bar{K}^0 = \mathbf{CP}K^0$)

$$\begin{aligned} \mathbf{CP}K_1 = \mathbf{CP}[(K^0+\bar{K}^0)/\sqrt{2}] = (K^0+\bar{K}^0)/\sqrt{2} = K_1, \\ \mathbf{CP}K_2 = \mathbf{CP}[(K^0-\bar{K}^0)/\sqrt{2}] = (K^0-\bar{K}^0)/\sqrt{2} = -K_2. \end{aligned} \tag{2.1}$$

Because of $\mathbf{CP}(\pi^+\pi^-) = (\pi^+\pi^-)$ for π mesons in a state with an angular momentum zero , the decay into $\pi^+\pi^-$ is allowed for the K_1, but forbidden for the K_2; hence the longer lifetime of K_2 , which was indeed confirmed when the K_2 was discovered.

In 1964, however, Christenson, Cronin, Fitch and Turlay discovered that the long-lived neutral K meson also decays to $\pi^+\pi^-$ with a branching ratio of $\sim 2\times 10^{-3}$. From then the long-lived state was called K_L because it was no longer identical to the CP eigenstate K_2; similarly, the short-lived state was called K_S. The CP violation that manifested itself by the decay $K_L \to \pi^+\pi^-$ was confirmed by subsequent discoveries of the $K_L \to \pi^0\pi^0$, and of a charge asymmetry in the decays $K_L \to \pi^\pm e^\mp \nu$ and $K_L \to \pi^\pm \mu^\mp \nu$.

2.2 Phenomenology of CP violation in B decays

Decays of B mesons are expected to be the most promising processes to clarify the nature of CP violation. Below we categorize three types of CP violation.

1. Direct CP violation in weak decays, which occurs in both charged and neutral meson decays.

2. Indirect CP violation in the mixing.

3. CP violation in the interference of mixing and decay, which occurs in decays into final states that are common to B^0 and $\bar{B}^0$.

In each case it is useful to identify a particular CP violating quantity that is independent of phase conventions and discuss the types of processes that depend on this quantity. In following sections phenomenology for each type is described.

2.2.1 Direct CP Violation in Weak Decays

Consider two decay processes related to each other by a CP transformation. Let P and $\bar{P}$ be CP-conjugated pseudoscalar meson states, and f and $\bar{f}$ some CP-conjugated final states:

$$\mathbf{CP}|P\rangle = e^{i\phi_P}|\bar{P}\rangle, \qquad \mathbf{CP}|f\rangle = e^{i\phi_f}|\bar{f}\rangle. \tag{2.2}$$

The phase ϕ_P and ϕ_f are arbitrary. The CP-conjugated decay amplitudes, A and $\bar{A}$, can be written as

$$\begin{aligned} A &= \langle f|\mathcal{H}|P\rangle \sum_i A_i e^{i\delta_i} e^{i\phi_i}, \\ \bar{A} &= \langle \bar{f}|\mathcal{H}|\bar{P}\rangle = e^{i(\phi_P-\phi_f)} \sum_i A_i e^{i\delta_i} e^{-i\phi_i}, \end{aligned} \tag{2.3}$$

where $\mathcal{H}$ is the effective Hamiltonian for weak decays, and A_i are real partial amplitudes. Two types of phases may appear in the decay amplitudes: the weak phases ϕ_i are parameters of the Lagrangian that violate CP. They usually appear in the electroweak sector of the theory and enter A and $\bar{A}$ with opposite signs. The strong phases δ_i appear in scattering amplitudes even if the Lagrangian is CP invariant. They usually arise from rescattering effects due to the strong interactions and enter A and $\bar{A}$ with the same sign.

Although the definition of strong and weak phases is to a large degree convention-dependent, one can show that a ratio

$$\left|\frac{\bar{A}}{A}\right| = \left|\frac{\sum_i A_i e^{i\delta_i} e^{i\phi_i}}{\sum_i A_i e^{i\delta_i} e^{-i\phi_i}}\right| \tag{2.4}$$

is independent of phase conventions and therefore physically meaningful. The condition

$$\left|\frac{\bar{A}}{A}\right| \neq 1 \quad \Rightarrow \quad \text{direct CP violation} \tag{2.5}$$

implies CP violation, which results from the interference of decay amplitudes leading to the same final state. Note that this requires at least two partial amplitudes that differ in both their weak and strong phases.

Experimental observation of direct CP violation:

Since mixing is unavoidable in neutral meson decays, it is better to observe direct CP violation in the decays of charged mesons. One defines the CP asymmetry:

$$a_f = \frac{\Gamma(P^+ \to f) - \Gamma(P^- \to \bar{f})}{\Gamma(P^+ \to f) + \Gamma(P^- \to \bar{f})} = \frac{1 - |\bar{A}/A|^2}{1 + |\bar{A}/A|^2}. \tag{2.6}$$

The requirement of at least two partial amplitudes with different phases forces us to consider non-leptonic decays, since leptonic and semileptonic decays are usually dominated by a single diagram. Non-leptonic decays, on the other hand, can receive so-called "tree" and "penguin" contribution[16]. Penguin diagrams contain a W-boson-quark loop and typically involve other weak phases than tree diagrams. In order to get large interference effects, one needs partial amplitudes with similar magnitude[17]. A possibility is to consider decays in which the tree contribution is suppressed, with respect to the penguin contribution, by small KM parameters[1].

This compensates for the loop suppression of penguin diagrams. In the Standard Model, an example of this type is the decay $B^\pm \to K^\pm \rho^0$ shown in Figure 2.1, for which the penguin diagram is proportional to $(\alpha_s/12\pi)\ln(m_t^2/m_b^2)|V_{tb}V_{ts}^*| \simeq 0.02 \times 0.04 \sim 10^{-3}$[18, 19, 20]. Another possibility is to consider tree-forbidden decays, which can only proceed through penguin diagrams. In this case, it is the possibility to have different quarks in the loop (t, c, u) that leads to the interference. Examples are $B^\pm \to K^\pm K$ and $B^\pm \to K^\pm \phi$, as well as the radiative decays $B^\pm \to K^{*\pm}\gamma$ and $B^\pm \to \rho^\pm \gamma$, see Figure 2.2.

There is no unambiguous experimental evidence for direct CP violation yet[1].

[1] KM parameters are described in Section 2.3.

[1] This is the situation as of March 1999. However, it is expected that new papers on K decays will be submitted soon[21].

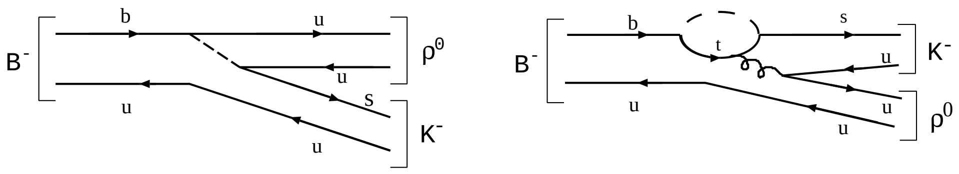

Figure 2.1: *Tree and penguin diagrams for the decay* $B^{\pm} \to K^{\pm}\rho^0$.

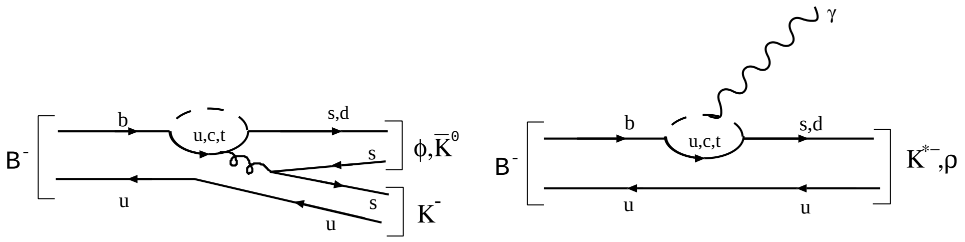

Figure 2.2: *Penguin diagrams for some tree-forbidden* B *decays.*

2.2.2 Indirect CP Violation in the Mixing of Neutral Mesons

The neutral mesons P^0 and $\bar{P}^0$ can mix via common decay channels:

$$P^0 \leftrightarrow X \leftrightarrow \bar{P}^0 \tag{2.7}$$

An arbitrary neutral meson state can thus be written as a superposition of the flavor eigenstates, $a|P^0\rangle + b|\bar{P}^0\rangle$, which obeys the time-dependent Schrödinger equation

$$i\frac{d}{dt}\begin{pmatrix} a \\ b \end{pmatrix} = H\begin{pmatrix} a \\ b \end{pmatrix} = \left(M - \frac{i}{2}\Gamma\right)\begin{pmatrix} a \\ b \end{pmatrix} \tag{2.8}$$

where $\mathbf{M}$ and Γ are Hermitian 2×2 matrices, which are called the mass and decay matrices, respectively. Since the Hamilton operator, $\mathbf{H}$, is not Hermitian, its eigenvectors

$$|P_{1,2}\rangle = p|P^0\rangle \pm q|\bar{P}^0\rangle; \quad |p^2| + |q^2| = 1 \tag{2.9}$$

are not orthogonal, and the eigenvalues

$$\mu_i = M_i - \frac{i}{2}\Gamma_i; \quad i = 1, 2 \tag{2.10}$$

are complex. This reflects that the states P_1 and P_2 are resonances, not elementary particles. M_i are the masses of these resonances, and Γ_i are their decay widths. The states P_i have a diagonal time evolution given by

$$|P_i(t)\rangle = e^{-iM_i t}e^{-\frac{1}{2}\Gamma_i t}|P_i(0)\rangle. \tag{2.11}$$

One can show that ratio

$$\left|\frac{q}{p}\right| = \left|\frac{M_{12}^* - \frac{i}{2}\Gamma_{12}^*}{M_{12} - \frac{i}{2}\Gamma_{12}}\right| \tag{2.12}$$

is independent of phase conventions and therefore physically meaningful. The condition

$$\left|\frac{q}{p}\right| \neq 1 \quad \Rightarrow \quad \text{indirect CP violation} \tag{2.13}$$

implies CP violation, which results from the fact that the mass eigenstates are different from the CP eigenstates.

Let us collect some useful equations related to the mixing of neutral mesons. Define the mass difference $\Delta m = m_2 - m_1$ and the width difference $\Delta\Gamma = \Gamma_1 - \Gamma_2$. Then the following relations hold:

$$\begin{aligned}
(\Delta m)^2 - \frac{1}{4}(\Delta\Gamma)^2 &= 4|M_{12}|^2 - |\Gamma_{12}|^2, \\
\Delta m \cdot \Delta\Gamma &= 4Re(M_{12}\Gamma_{12}^*), \\
\frac{q}{p} &= -\frac{1}{2}\frac{\Delta m - \frac{i}{2}\Delta\Gamma}{M_{12} - \frac{i}{2}\Gamma_{12}} = -2\frac{M_{12}^* - \frac{i}{2}\Gamma_{12}^*}{\Delta m - \frac{i}{2}\Delta\Gamma}.
\end{aligned} \tag{2.14}$$

An alternative common notation is to define $\bar{\epsilon}$ such that

$$p = \frac{1+\bar{\epsilon}}{\sqrt{2(1+|\bar{\epsilon}|^2)}}, \qquad q = \frac{1-\bar{\epsilon}}{\sqrt{2(1+|\bar{\epsilon}|^2)}}, \qquad \frac{q}{p} = \frac{1-\bar{\epsilon}}{1+\bar{\epsilon}}. \tag{2.15}$$

q/p in the B-meson system:

Decay channels common to B^0 and $\bar{B}^0$, which are responsible for the difference $\Delta\Gamma_B$, are known to have branching fractions of order 10^{-3} or less. Hence, although $\Delta\Gamma_B$ has not yet been measured directly, it follows that $|\Delta\Gamma_B|/\Gamma_B < 10^{-2}$. On the other hand, the observed $B^0 - \bar{B}^0$ mixing rate implies[22] $\Delta m_B/\Gamma_B = 0.74 \pm 0.04$, so that model independently

$$|\Delta\Gamma_B| \ll \Delta m_B \tag{2.16}$$

thus, there is a negligible lifetime difference between the CP eigenstates, and one therefore refers to these states as "light" ($=B_L$) and "heavy" ($=B_H$). It follows that $|\Gamma_{12}| \ll |M_{12}|$, and to first order in Γ_{12}/M_{12} we obtain from (2.14)

$$\left(\frac{q}{p}\right)_B \simeq -\frac{M_{12}^*}{|M_{12}|}\left(1 - \frac{1}{2}Im\frac{\Gamma_{12}}{M_{12}}\right). \tag{2.17}$$

Hence

$$|\frac{q}{p}| - 1 \simeq -2\,Re\,\bar{\epsilon}_B = \mathcal{O}(10^{-2}). \tag{2.18}$$

As in the kaon system, CP violation in $B^0 - \bar{B}^0$ mixing is a small effect.

Experimental observation of indirect CP violation in the B-meson system:

Since B_L and B_H have almost identical lifetimes, it is not possible to produce selectively beams of B_L or B_H particles. With $m_{H,L} = m_B \pm \frac{1}{2}\Delta m_B$ and $\Gamma_{H,L} \simeq \Gamma_B$, equation (2.11) gives for the time evolution of an initially pure B^0 state:

$$\begin{aligned}
|B^0(0)\rangle &= \frac{1}{2p}\left(|B_H\rangle + |B_L\rangle\right), \\
|B^0(t)\rangle &= \frac{1}{2p}e^{-im_Bt}e^{-\frac{1}{2}\Gamma_Bt}\left\{e^{-\frac{i}{2}\Delta m_Bt}|B_H\rangle + e^{\frac{i}{2}\Delta m_Bt}|B_L\rangle\right\}, \\
&= e^{-im_Bt}e^{-\frac{1}{2}\Gamma_Bt}\left\{\cos\left(\frac{1}{2}\Delta m_Bt\right)|B^0\rangle + \frac{iq}{p}\sin\left(\frac{1}{2}\Delta m_Bt\right)|\bar{B}^0\rangle\right\}.
\end{aligned} \tag{2.19}$$

Similarly:

$$|\bar{B}^0(t)\rangle = e^{-im_B t} e^{-\frac{1}{2}\Gamma_B t} \left\{ \cos\left(\frac{1}{2}\Delta m_B t\right) |\bar{B}^0\rangle + \frac{ip}{q} \sin\left(\frac{1}{2}\Delta m_B t\right) |B^0\rangle \right\}. \tag{2.20}$$

Defining the semileptonic asymmetry as

$$a_{SL}^B = \frac{\Gamma(\bar{B}^0(t) \to l^+ \bar{\nu} X) - \Gamma(B^0(t) \to l^- \nu X)}{\Gamma(\bar{B}^0(t) \to l^+ \bar{\nu} X) + \Gamma(B^0(t) \to l^- \nu X)}. \tag{2.21}$$

We obtain

$$a_{SL}^B = \frac{1 - |q/p|^4}{1 + |q/p|^4} \simeq 4\, Re\, \bar{\epsilon}_B = \mathcal{O}(10^{-2}). \tag{2.22}$$

To date, there is no experimental evidence for indirect CP violation in the B-meson system.

2.2.3 CP Violation in the Interference of Mixing and Decay

Consider decays of neutral mesons into CP eigenstates:

$$A = \langle f_{CP} | \mathcal{H} | P^0 \rangle, \quad A^* = \langle f_{CP} | \mathcal{H} | \bar{P}^0 \rangle. \tag{2.23}$$

It can be shown that the product

$$\lambda = \frac{q}{p} \cdot \frac{\bar{A}}{A} \tag{2.24}$$

is independent of phase conventions and thus physically meaningful. In other words, the convention dependence of q/p cancels against that of $\bar{A}/A$. The condition

$$\lambda \neq \pm 1 \quad \Rightarrow \quad \text{CP violation} \tag{2.25}$$

implies CP violation. Note that direct CP violation($|\bar{A}/A| \neq 1$) and indirect CP violation ($|q/p| \neq 1$) imply $|\lambda| \neq 1$, but they are not necessary for the weaker condition $\lambda \neq \pm 1$.

Many decays of neutral B mesons are the kind described above. This type of CP violation is called CP violation in the interference of mixing and decay. Consider the time evolution of a state which is identified as B^0 at time 't' = 0 as

$$t = 0: \quad |B^0\rangle = \frac{1}{2p}(|B_L\rangle + |B_H\rangle), \tag{2.26}$$

Since B_L and B_H evolve according to Equation (2.9), the $|B^0\rangle$ oscillates into a mixture of B^0 and $\bar{B}^0$ as Equation (2.19) and (2.20). Let's consider decays into states $|f\rangle$ which are eigenstates of CP, i.e. $CP|f\rangle = \eta|f\rangle$, with eigenvalue $\eta = \pm 1$, and let's assume that a single weak amplitude (or rather a single weak phase) dominates the decay process. Both B^0 and $\bar{B}^0$ decay to the state f, with amplitudes:

$$\begin{aligned} B^0 \quad &: \quad A = |A| e^{i\phi_f} e^{i\delta_f} \\ \bar{B}^0 \quad &: \quad \bar{A} = \eta |A| e^{-i\phi_f} e^{i\delta_f} \end{aligned} \tag{2.27}$$

where ϕ_f and δ_f are the weak and strong phases, respectively. The "clean modes" with $|\lambda| \simeq 1$ are those dominated by a single weak phase ϕ_f, so that

$$\frac{\bar{A}}{A} \simeq e^{-2i\phi_f} \tag{2.28}$$

is close to a pure phase. Using Equation (2.26), the time dependent decay rates of an initial B^0 and $\bar{B}^0$ can be written as

$$\begin{aligned}
\Gamma(t) &= \Gamma(B^0(t) \to f) = e^{-\Gamma_B t}|A|^2 \qquad (2.29)\\
&\quad \times \left\{ \frac{1+|\lambda|^2}{2} + \frac{1-|\lambda|^2}{2}\cos\Delta mt - Im(\lambda)\sin\Delta mt \right\} \\
\bar{\Gamma}(t) &= \Gamma(\bar{B}^0(t) \to f) = e^{-\Gamma_B t}|\frac{p}{q}^2||A|^2 \qquad (2.30)\\
&\quad \times \left\{ \frac{1+|\lambda|^2}{2} - \frac{1-|\lambda|^2}{2}\cos\Delta mt + Im(\lambda)\sin\Delta mt \right\}
\end{aligned}$$

If one defines the CP asymmetry [8, 23]

$$a_{f_{CP}} = \frac{\Gamma(B^0(t) \to f_{CP}) - \Gamma(\bar{B}^0(t) \to f_{CP})}{\Gamma(B^0(t) \to f_{CP}) + \Gamma(\bar{B}^0(t) \to f_{CP})} \qquad (2.31)$$

and takes into account that $|q/p|_B \simeq 1$ so that we can put $\frac{q}{p} = e^{-2i\phi_f}$, it follows that

$$\begin{aligned}
a_{f_{CP}} &\simeq \frac{(1-|\lambda|^2)\cos(\Delta m_B t) - 2Im\lambda\sin(\Delta m_B t)}{1+|\lambda|^2} \\
&\stackrel{|\lambda|=1}{\rightarrow} -Im\lambda\sin(\Delta m_B t). \qquad (2.32)
\end{aligned}$$

This method using such decays is very useful and shows large CP violation in the Standard Model prediction. The quantity Imλ which can be extracted from $a_{f_{CP}}$ is theoretically very interesting since it can be directly related to KM matrix elements in the Standard Model. The detail of this decay on B-mesons is described in Section 2.4.

2.3 CP Violation in the Standard Model

2.3.1 KM Matrix

In terms of the mass eigenstates, a Lagrangian of weak interaction forms

$$\mathcal{L}_{int} = -\frac{g}{\sqrt{2}}(\bar{u_L}, \bar{c_L}, \bar{t_L})\,\gamma^\mu V \begin{pmatrix} d_L \\ s_L \\ b_L \end{pmatrix} W_\mu + h.c.. \qquad (2.33)$$

The KM(Kobayashi-Maskawa) mixing matrix V is a unitary matrix in flavor space. In the general case of n quark generations, V would be an $n \times n$ matrix. For the case of three generations, V is then, explicitly,

$$V = \begin{pmatrix} V_{ud} & V_{us} & V_{ub} \\ V_{cd} & V_{cs} & V_{cb} \\ V_{td} & V_{ts} & V_{tb} \end{pmatrix}, \qquad (2.34)$$

which can be parametrized by three Euler angels and six phases, five of which can be removed by adjusting the relative phases of left-handed quark fields. Hence, three angles θ_{ij} and observable phase δ remain in the quark mixing matrix, as was first pointed out by Kobayashi and Maskawa[7]. The imaginary part of the mixing matrix is necessary to describe CP violation in the Standard Model. In general, CP is violated in flavor-changing decays if there is no degeneracy of any two quark masses, and if the quantity $J_{CP} \neq 0$, where

$$J_{CP} = \left| Im(V_{ij} V_{kl} V_{il}^* V_{kj}^*) \right| ; i \neq k, j \neq l. \tag{2.35}$$

It can be shown that all the CP-violating amplitudes in the Standard Model are proportional to J_{CP}, and that this quantity is invariant under phase redefinitions of the quark fields[24, 25].

For many applications, it is convenient to use an approximate parametrization of the KM matrix, called Wolfenstein parametrization[26], which makes explicit the strong hierarchy observed experimentally.

$$V \cong \begin{pmatrix} 1-(\lambda^2/2) & \lambda & A\lambda^3(\rho - i\eta) \\ -\lambda & 1-(\lambda^2/2) & A\lambda^2 \\ A\lambda^3(1-\rho-i\eta) & -A\lambda^2 & 1 \end{pmatrix}. \tag{2.36}$$

Using this parametrization, we obtain

$$J_{CP} \simeq A^2 \eta \lambda^6, \tag{2.37}$$

which shows that J_{CP} is of order 10^{-4} for $\lambda \simeq 0.22$ and $A \simeq 0.8$.

In principle, the entries in the first two rows of mixing matrix are accessible in so-called direct (tree-level) process, i.e. in weak decays of hadrons containing the corresponding quarks. In practice, $|V_{ud}|$ and $|V_{us}|$ are known to an accuracy of better than 1%, $|V_{cb}|$ is known to 5%, and $|V_{cd}|$ and $|V_{cs}|$ are known to about 10~20%. Hence, the two Wolfenstein parameters λ and A are rather well determined experimentally:

$$\lambda = |V_{us}| = 0.2205 \pm 0.0018, \qquad A = \left| \frac{V_{cb}}{V_{us}^2} \right| = 0.80 \pm 0.04. \tag{2.38}$$

On the other hand, $|V_{ub}|$ has an uncertainty of about 30%, and the same is true for $|V_{td}|$, which is obtained from $B^0 - \bar{B}^0$ mixing. This implies a rather significant uncertainty in the values of the Wolfenstein parameters ρ and η. A more precise determination of these parameters will be a challenge to experiments and theory over the next decade.

2.3.2 The Unitarity Triangle

A simple visualization of the implications of unitarity is provided by the so-called unitarity triangle, which uses the fact that the unitarity equation

$$V_{ij} V_{ik}^* = 0 \quad (j \neq k) \tag{2.39}$$

can be represented as the equation of a closed triangle in the complex plane. Most useful from the phenomenological point of view is the triangle relation

$$V_{ud} V_{ub}^* + V_{cd} V_{cb}^* + V_{td} V_{tb}^* = 0, \tag{2.40}$$

since it contains the most poorly-known entries in the KM matrix. In the standard parametrization, $V_{cd} V_{cb}^*$ is real, and the unitarity triangle has the form shown in Figure 2.3. It is useful to rescale the triangle by dividing all sides by $|V_{cd} V_{cb}^*|$. The rescaled triangle has the coordinates (0,0),(1,0), and ($\bar{\rho}$,$\bar{\eta}$), where

$$\bar{\rho} = \left(1 - \frac{\lambda^2}{2}\right) \rho, \quad \bar{\eta} = \left(1 - \frac{\lambda^2}{2}\right) \eta \tag{2.41}$$

are related to the Wolfenstein parameters ρ and η appearing in (2.36). CP is violated when the area of the triangle does not vanish, i.e. when all the angles are different from zero. The three angles of the triangle are defined as

$$\phi_1 \equiv -arg\left(\frac{V_{td}V_{tb^*}}{V_{cd}V_{cb}^*}\right), \quad \phi_2 \equiv arg\left(\frac{V_{ud}V_{ub^*}}{V_{td}V_{tb}^*}\right), \quad \phi_3 \equiv arg\left(\frac{V_{cd}V_{cb^*}}{V_{ud}V_{ub}^*}\right). \tag{2.42}$$

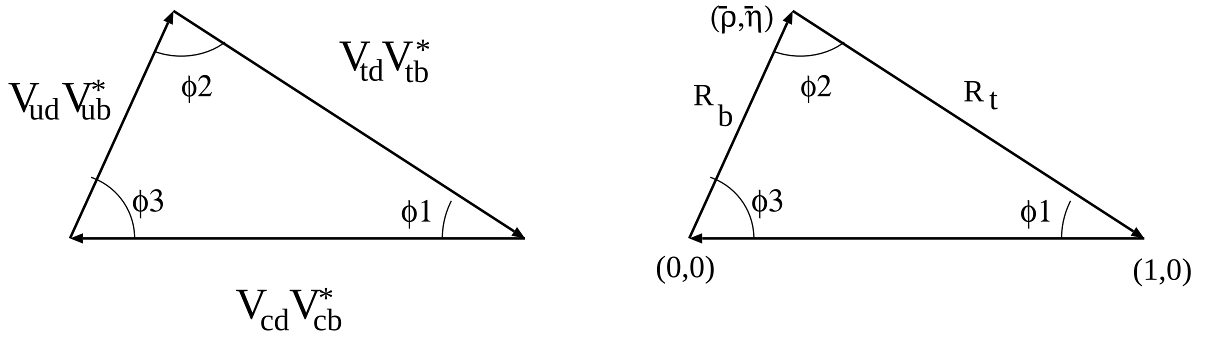

Figure 2.3: *The unitarity triangle of the KM matrix (left) and its rescaled form in the $(\bar\rho - \bar\eta)$ plane (right).*

To determine the shape of the triangle, one can aim for measurements of the two sides R_b and R_t, and three angles ϕ_1, ϕ_2, and ϕ_3 (Figure 2.3). So far, experimental information is available only on the sides of the triangle. The current value of $|V_{ub}|$[27, 28] implies

$$R_b = \sqrt{\bar\rho^2 + \bar\eta^2} = \left(1 - \frac{\lambda^2}{2}\right)\frac{1}{\lambda}\left|\frac{V_{ub}}{V_{cb}}\right| = 0.35 \pm 0.09. \tag{2.43}$$

To determine R_t , one needs information on $|V_{td}|$, which can be extracted from $B^0 - \bar B^0$ mixing. In the Standard Model, the mass difference Δm_B between the two neutral meson states is calculable from the box diagrams shown in figure 2.4. The resulting theoretical expression is

$$\Delta m_B = \frac{G_F^2 m_W^2}{6\pi^2}\eta_B B_B f_B^2 m_B S(m_t/m_W)|V_{td}V_{tb}^*|^2, \tag{2.44}$$

where $\eta_B = 0.55 \pm 0.01$ accounts for the QCD corrections[29], and $S(m_t/m_W)$ is a function of the top quark mass[30]. The product $B_B f_B^2$ parameterizes the hadronic matrix element of a local four-quark operator between B-meson states. There exists a vast literature on calculations of the decay constant f_B and the B_B parameter. Combining the results of some recent QCD sum-rule[31] and lattice calculations[32], we quote the value

$$f_B = 185 \pm 40 MeV. \tag{2.45}$$

Together with the prediction $B_B \simeq 1.08$ obtained from lattice calculations[33], this gives

$$B_B^{1/2} f_B = (200 \pm 40) MeV. \tag{2.46}$$

Solving then (2.44) for $|V_{td}|$, one obtains[34]

$$|V_{td}| = 8.59 \times 10^{-3} \left(\frac{200\ MeV}{B_B^{1/2} f_B}\right) \left(\frac{170\ GeV}{\bar{m}_t(m_t)}\right)^{0.76} \left(\frac{\Delta m_B}{0.471\ ps^{-1}}\right)^{1/2}. \tag{2.47}$$

Taking $\bar{m}_t(m_t) = (170 \pm 15) GeV$ for the running top-quark mass, and using the average experiment value[35]

$$\Delta m_B = (0.471 \pm 0.016) ps^{-1}, \tag{2.48}$$

gives

$$|V_{td}| = (8.59 \pm 1.51) \times 10^{-3}. \tag{2.49}$$

The corresponding range of values for R_t is

$$R_t = \sqrt{(1-\bar{\rho}^2) + \bar{\eta}^2} = \frac{1}{\lambda}\left|\frac{V_{td}}{V_{cb}}\right| = 1.10 \pm 0.17. \tag{2.50}$$

Equations (2.43) and (2.50) yield constraints on the Wolfenstein parameters $\bar{\rho}$ and $\bar{\eta}$, which

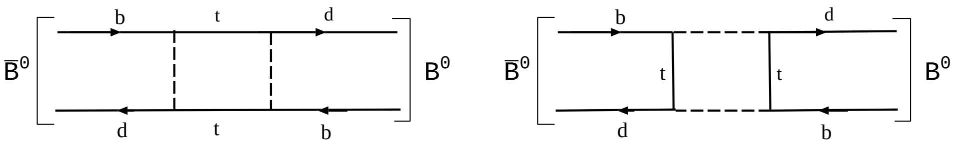

Figure 2.4: *Box diagram for $B^0 - \bar{B}^0$ mixing in the Standard Model.*

have the form of rings centered at $(\bar{\rho}, \bar{\eta}) = (0, 0)$ and (0,1). Another constraint can be obtained from the measurement of indirect CP violation in the kaon system. The experimental result on the parameter ϵ_K measuring CP violation in $K^0 - \bar{K}^0$ mixing implies that the unitarity triangle lies the upper half plane. The constraint arising in the $\bar{\rho} - \bar{\eta}$ plane has the form of a hyperbola, the shape of which depends on a hadronic parameter B_K. The theoretical prediction is [36]

$$\bar{\eta}\left[(1-\bar{\rho})A^2\left(\frac{m_t}{m_W}\right)^{1.52} + (0.69 \pm 0.05)\right] A^2 B_K \simeq 0.50, \tag{2.51}$$

where $A = 0.80 \pm 0.04$ according to (2.38). In the last few years, theoretical calculations of the B_K parameter have converged and give results[36] of

$$B_K = 0.75 \pm 0.15 \tag{2.52}$$

In principle, the measurement of the ratio $\mathrm{Re}(\epsilon'/\epsilon)$ in the kaon system could provide a determination of η independent of ρ. In practice, however, the experimental situation is unclear[37, 38], and the theoretical calculations[39] of this ratio are affected by large uncertainties, so that there currently is no useful bound to be derived.

In Figure 2.5, we show the constraints which the measurements of R_b, R_t, and ϵ_K imply in the $\bar{\rho} - \bar{\eta}$ plane. Given the present theoretical and experimental uncertainties in the analysis of charmless B-decays, $B^0 - \bar{B}^0$ mixing, and CP violation in the kaon system, there is still a rather large region allowed for the Wolfenstein parameters. This has important implications. For instance, the allowed region for the angle ϕ_1 of the unitarity triangle is such that

$$0.34 < \sin 2\phi_1 < 0.75. \tag{2.53}$$

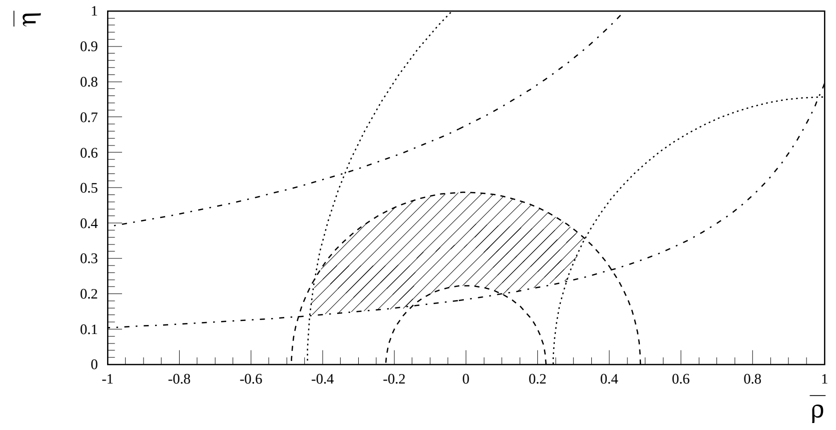

Figure 2.5: *Experimental constraints on the unitarity triangle in the $\bar{\rho} - \bar{\eta}$ plane. The region between the dashed (dotted) circles is allowed by the measurement of R_b (R_t) discussed in text. The dash-dotted curves show the constraint following from the measurement of the ε_k parameter in the kaon system. Each constraint shows the region with the confidence level of 95%.*

Among the three CP angles of unitarity triangle, ϕ_1 is expected to be the most measurable experimentally with CP violation in the interference of mixing and decay described in Section 2.2.3.

2.4 $B \to$ Charmonium + K_S mode

As already mentioned in Section 2.2 and 2.3, the decay of neutral B mesons into CP eigenstates shows a large CP asymmetry and we can extract the elements of KM matrix from this asymmetry. In this section, we describe the extraction of ϕ_1 through CP violation in the interference of mixing and decay in $B \to \text{charmonium} + K_S$.

2.4.1 Charmonium modes

Figure 2.6 shows the charmonium system. Table 2.1 shows observed branching ratios for $B^0(B^\pm) \to \text{charmonium} + K^0(K^*)$.

$B^0(\bar{B^0}) \to J/\psi K_S$

The combination of relatively large branching fractions, readily accessible final states with small backgrounds and negligible theoretical uncertainty have earned the decay $B \to J/\psi K_S$ the name "gold-plated mode". Among all $B \to \text{charmonium} + K_S$ modes, $J/\psi K_S$ is the most effective decay mode experimentally to measure ϕ_1.

$B^0(\bar{B^0}) \to \psi(2S) K_S$

The decay mode $B \to \psi(2S) K_S$ has not been observed yet, but is estimated to have about the same branching ratio as that of $B \to J/\psi K_S$ assuming the isospin symmetry between

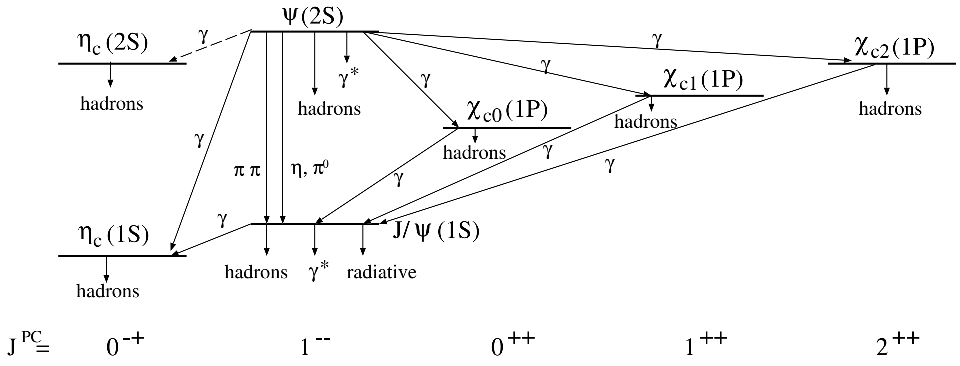

Figure 2.6: *The current state of knowledge of the charmonium system and transitions[46].*

$B^0 \to \psi(2S)K_S$ and $B^+ \to \psi(2S)K^+$.

$B^0(\bar{B^0}) \to \chi_{c1}K_S$

The decay mode $B \to \chi_{c1}K_S$ has not been observed yet. However, this mode may have larger branching ratio than that of $B \to J/\psi K_S$, again assuming the isospin symmetry.

$B^0(\bar{B^0}) \to \eta_c K_S$

The decay mode $B \to \eta_c K_S$ has not been observed yet. However some recent theoretical works show that $B \to \eta_c K_S$ has the branching ratio 1.6~2.3 times larger than that of $B \to J/\psi K_S$[41, 42]. In addition, recently CLEO reported a large branching ratio for a corresponding charged mode[40]. This mode is therefore promising.

2.4.2 CP Asymmetry in $b \to c\bar{c}s$ transition

In the B meson system, up to corrections of order 10^{-2}, we have

$$\left(\frac{q}{p}\right) \simeq -\frac{M_{12}^*}{|M_{12}|} = \frac{(V_{tb}^* V_{td})^2}{|V_{tb}^* V_{td}|^2} = \frac{V_{tb}^* V_{td}}{V_{tb} V_{td}^*} = e^{-2i\phi_1}. \tag{2.54}$$

This combination of KM parameters can be read off directly from the vertices of the box diagram in Figure 2.4, which in the Standard Model are responsible for the non-diagonal element M_{12}^* of the mass matrix. Notice that for the real part of the box diagrams, which determine M_{12}, the contributions of c and u quarks in the loops can be neglected. The decay $B \to$ charmonium$+K_S$ is based on the quark transition $b \to c\bar{c}s$, for which the tree diagram is dominant. All processes, which have quark transition of $b \to c\bar{c}s$, follow the same line except the CP eigenvalue of the final states. As shown in Figure 2.7, the tree amplitude is proportional to $V_{cb}V_{cs}^* \sim \lambda^{-2}$. With CP$(J/\psi K_S)$=-1, one finds

$$\lambda_{J/\psi K_S} = -\left(\frac{q}{p}\right)_B \cdot \left(\frac{q}{p}\right)_K \cdot \frac{\bar{A}}{A} \simeq \frac{V_{tb}^* V_{td}}{V_{tb} V_{td}^*} \cdot \frac{V_{cs} V_{cd}^*}{V_{cs}^* V_{cd}} \cdot \frac{V_{cb} V_{cs}^*}{V_{cb}^* V_{cs}} = -e^{-2i\phi_1}, \tag{2.55}$$

Table 2.1: *Data on branching ratios for $B \to Charmonium + K(K^*)$*

Decay mode	Experimental Branching Ratio	Reference
$J/\psi \bar{K}^0$	$(8.9 \pm 1.2) \times 10^{-4}$	[46]
$J/\psi K^-$	$(9.9 \pm 1.0) \times 10^{-3}$	[46]
$J/\psi \bar{K}^{*0}$	$(1.35 \pm 0.18) \times 10^{-3}$	[46]
$J/\psi K^{*-}$	$(1.47 \pm 0.27) \times 10^{-3}$	[46]
$\psi(2S)\bar{K}^0$	$\leq 8 \times 10^{-4}$	[46]
$\psi(2S)K^-$	$(6.9 \pm 3.1) \times 10^{-4}$	[46]
$\psi(2S)\bar{K}^{*0}$	$(1.49 \pm 0.9) \times 10^{-3}$	[46]
$\psi(2S)K^{*-}$	$\leq 3 \times 10^{-3}$	[46]
$\chi_{c1}\bar{K}^0$	$\leq 2.7 \times 10^{-3}$	[46]
$\chi_{c1}\bar{K}^-$	$(1.0 \pm 0.4) \times 10^{-3}$	[46]
$\chi_{c1}\bar{K}^*$	$\leq 2.1 \times 10^{-3}$	[46]
$\chi_{c1}\bar{K}^{*-}$	$\leq 2.1 \times 10^{-3}$	[46]
$\eta_c\bar{K}^0$	$\leq 6.8 \times 10^{-3}$	[40]
$\eta_c\bar{K}^-$	$1.54^{+1.39}_{-0.87}(stat.) \pm 0.62(syst.) \times 10^{-3}$	[40]
$\eta_c\bar{K}^{*0}$	$\leq 5.95 \times 10^{-3}$	[40]
$\eta_c\bar{K}^{*-}$	$\leq 18.5 \times 10^{-3}$	[40]

where the first term comes from B^0-$\bar{B}^0$ mixing, the second from the ratio $\frac{\bar{A}(f)}{A(f)}$ and the third from K^0-$\bar{K}^0$ mixing. Therefore we obtain

$$Im\lambda_{J/\psi K_S} \simeq \sin 2\phi_1. \tag{2.56}$$

In the present case, the contamination from the penguin contribution is extremely small[8]. Depending on the flavor q of the quark in the loop, the penguin contributions are proportional to $V_{tb}V_{ts}^* \simeq \lambda^2$ (for $q = t$), $V_{cb}V_{cs}^* \simeq \lambda^2$ (for $q = c$), and $V_{ub}V_{us}^* \simeq \lambda^4$ (for $q = u$). Because of the relation $V_{tb}V_{ts}^* = -V_{cb}V_{cs}^* + \mathcal{O}(\lambda^4)$, it follows that up to very small corrections the penguin contributions have the same weak phase as the tree diagram. Hence, their presence affects neither $|\lambda|$ nor Imλ. Detailed estimates show that hadronic uncertainties are only of order 10^{-3}.

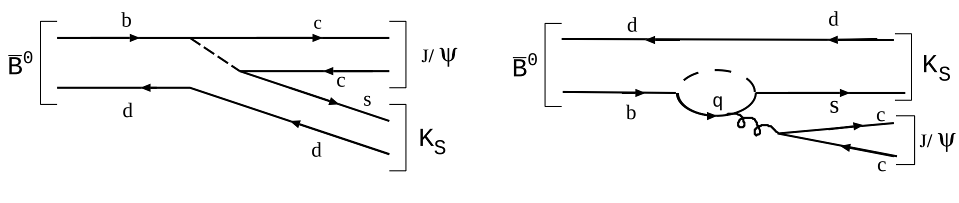

Figure 2.7: *Tree and penguin diagrams for the decay $B \to J/\psi K_S$.*

This measurement will thus give the theoretically cleanest determination of $\sin 2\phi_1$.

Table 2.2: *Examples of decay modes*

Quark subprocess	Examples of decay modes
$b \to c\bar{c}s$	$B^0 \to \eta_c K_S(K_L, K^{*0})$, $J/\psi K_S(K_L, K^{*0})$, $\psi(2S)K_S(K_L, K^{*0})$, $\chi_{c1}K_S(K_L, K^{*0})$
$b \to c\bar{c}d$	$B^0 \to D\bar{D}$,$D^*\bar{D}^*$,$D\bar{D}^*$
$b \to s\bar{s}s$	$B^0 \to \phi K_S(K_L, K^{*0})$

2.4.3 Comparison with other decay modes for $\phi_1$measurement

We show in Table 2.2 the examples of decay modes of B meson that can be used for ϕ_1 measurement. In the case of $B \to J/\psi K^{*0}$, two vector particles can have either even or odd relative angular momentum. Hence the final state is not a pure CP eigenstate. Although two different CP states can be separated by an analysis of the angular distribution of the decays[43], this requires more data to get a comparable accuracy for $\sin 2\phi_1$.

The channel $B \to J/\psi K_L$, and other $B \to \text{charmonium} + K_L$, also have a similar amplitude structure as $B \to \text{charmonium} + K_S$. Because of the difficulty of K_L detection, however, the efficiency and S/N ratio for $B \to J/\psi K_L$ would be worse than that in $B \to J/\psi K_S$ mode.

$B \to \phi K_S$ is theoretically clean as $B \to J/\psi K_S$. This decay proceeds through the quark transition $b \to s\bar{s}s$, i.e. it involves a flavor-changing neutral current, which is forbidden at the tree level in the Standard Model. The leading contribution comes from penguin diagram shown in Figure 2.8. The parameter λ is

$$\lambda_{\phi K_S} = \left(\frac{q}{p}\right)_B \cdot \left(\frac{q}{p}\right)_K \cdot \frac{\bar{A}}{A} \simeq \frac{V_{tb}^* V_{td}}{V_{tb} V_{td}^*} \cdot \frac{V_{cs} V_{cd}^*}{V_{cs}^* V_{cd}} \cdot \frac{V_{tb} V_{ts}^*}{V_{tb}^* V_{ts}} = e^{-2i\phi_1}, \tag{2.57}$$

and therefore

$$Im\lambda_{\phi K_S} \simeq -\sin 2\phi_1. \tag{2.58}$$

However, the branching ratio of $b \to \phi K_S$ is estimated to be an order of magnitude lower than that of $J/\psi K_S$. Therefore this mode doesn't have advantage to measure ϕ_1 experimentally.

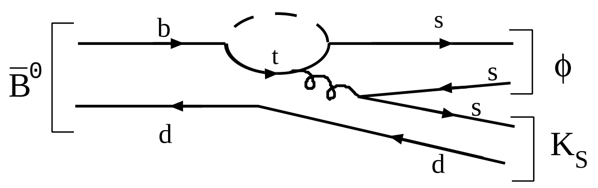

Figure 2.8: *Penguin diagram for the decay $B \to \phi K_S$.*

The decay $B \to D^+D^-$ is dominated by the tree diagram shown in Figure 2.9. The quark subprocess here is $b \to c\bar{c}d$. With CP(D^+D^-)=+1, the tree contribution gives

$$\lambda_{D^+D^-} = \frac{V_{tb}^* V_{td}}{V_{tb} V_{td}^*} \cdot \frac{V_{cd}^* V_{cb}}{V_{cd} V_{cb}^*} = e^{-2i\phi_1}. \tag{2.59}$$

Therefore we obtain

$$\text{Im}\lambda_{D^+D^-} \simeq -\sin 2\phi_1. \tag{2.60}$$

There are hadronic uncertainties due to the pure penguin term, but they are estimated to be small to 5%[45]. This decay mode has as large branching fraction as that of $B \to J/\psi K_S$. Although the reconstruction efficiency is low due to its multiplicity of daughter tracks, the number of useful events is still comparable to that of $B \to J/\psi K_S$. The background rejection plays a key role for this type of decay modes.

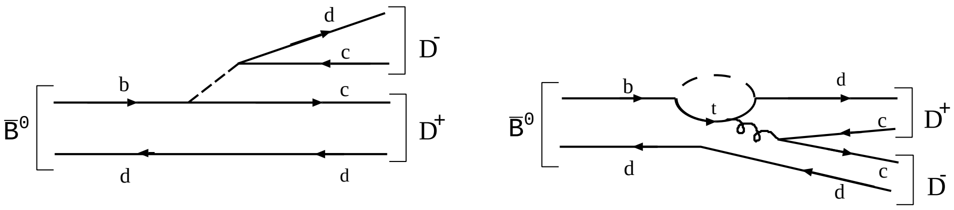

Figure 2.9: *Tree and penguin diagrams for the decay $B \to D^+D^-$.*

2.4.4 Observation of CP Violation in Asymmetric B-factory

In the KEK B-factory experiment, the initial B^0 and $\bar{B}^0$ are produced in a coherent $B^0\bar{B}^0$ state and remain in this state until one of them decays. If one B decays to a CP eigenmode, here $B \to$ charmonium $+ K_S$, and the other decays to a flavor specific mode, the event can be used to reconstruct the time dependence of CP asymmetry. (Figure 2.10)

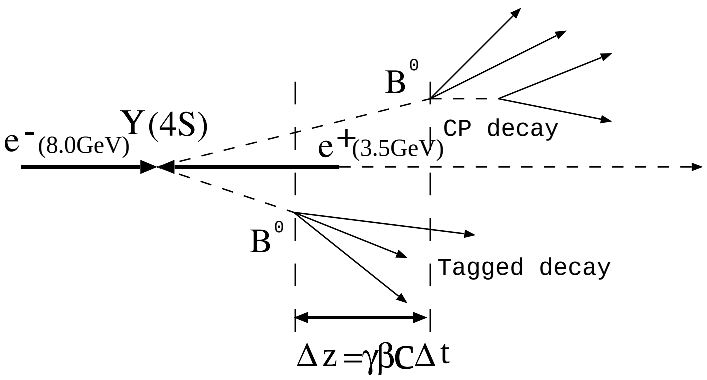

Figure 2.10: *Decay scheme of $B^0\bar{B}^0$ at asymmetric B factory. The proper time are measured from the distance of two B decays.*

CP asymmetry appears in difference of the decay rates between B^0 and $\bar{B}^0$. Figure 2.11 shows the proper time distribution for $B \to J/\psi K_S$ decays for the case of $\sin 2\phi_1 = +0.6$ as a function of the time distribution in units of the B lifetime, τ_B. The proper time shows the distribution as (2.29)$\sim$(2.32). The solid and dotted lines are the decay rates of the $\bar{B}^0$ and the B^0, respectively. The difference between the positive and negative time scale reflects the CP asymmetry. This can be seen either in the solid and dotted curves separately, or in the sum after the time scale of the dotted curve is reversed.

The proper time of B decay is measured with the distance of vertices of two B mesons as[2]

$$\Delta t \simeq \Delta z / c\beta\gamma, \tag{2.61}$$

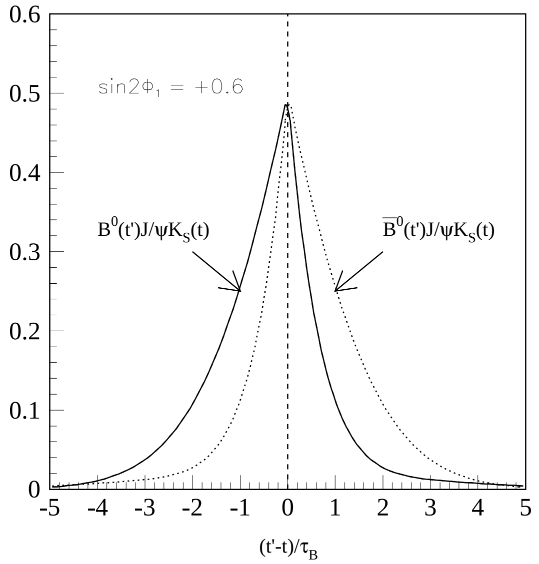

Figure 2.11: *Proper time distribution for* $B^0(\bar{B}^0) \to J/\psi K_S$.

where $\beta\gamma$ is the Lorentz boost factor due to the asymmetric beam energy ($\beta\gamma = 0.42$ at KEKB) and Δz is the distance between the decay vertices of the two B mesons along the beam direction. Figure 2.10 shows the measurement scheme of proper time of B mesons.

Flavor tagging

The flavor of B meson which decays into CP eigenstate is determined by the flavor of the other B meson which decays into flavor specific mode.

The charge of leptons or kaons from generic B decays has the information of the parent B meson. As shown in Figure 2.12, the lepton's charge from the b-quark($\bar{b}$-quark) decays into $c\mathrm{W}^-(\bar{c}\mathrm{W}^+)$ indicates flavor of B meson. As shown in Figure 2.13, the flavor of B meson has also correlation with the charge of the kaon in the final state.

Figure 2.14 shows the momentum distribution of leptons from B meson decays in $\Upsilon(4S)$ rest frame. Although leptons are produced in c decays also, one can efficiently remove such contamination by selecting high momentum lepton, *e.g.* above 1.2 GeV/c.

The flavor of B_{tag} has correlation to the sign of charge sum of charged kaon in final state.

[2] Δt is measured as the difference of two B mesons and is different from t in (2.32). When one B decays to a CP eigenmode and the other decays to a flavor specific mode, the decay rates are expressed as

$$\Gamma(B^0(t_1), f(t_2)) = e^{-\Gamma_B(t_1+t_2)}(1 - \sin 2\phi_1 \Delta m(t_1 - t_2))$$
$$\Gamma(\bar{B}^0(t_1), f(t_2)) = e^{-\Gamma_B(t_1+t_2)}(1 + \sin 2\phi_1 \Delta m(t_1 - t_2)).$$

where f is defined as a certain CP eigenstate. Integrating this equation over $(t_1 + t_2)$ to $(t_1 - t_2)(\equiv \Delta t)$, the proper time distribution would be same form as (2.29).

Figure 2.15 shows the charge sum of charged kaon detected and identified as kaon in an event.

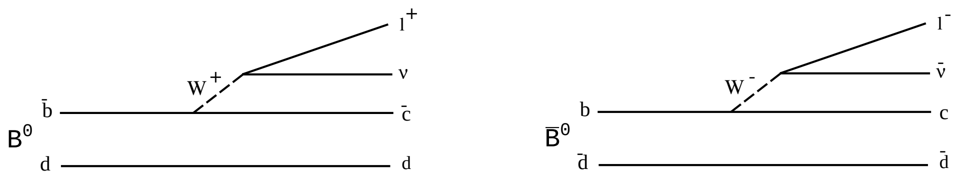

Figure 2.12: *Diagrams for flavor tagging with leptons.*

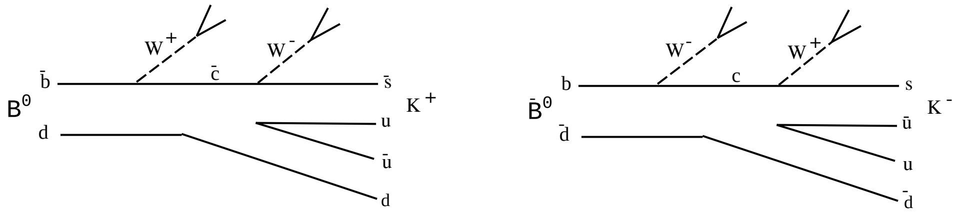

Figure 2.13: *Diagrams for flavor tagging with charged kaons.*

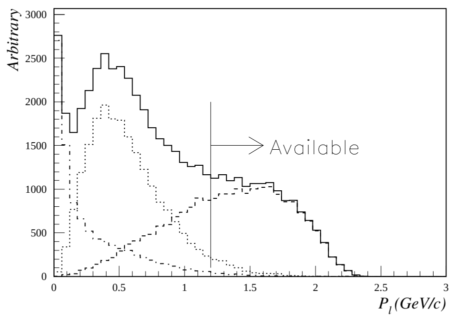

Figure 2.14: *Lepton momentum in generic B decay in the event generator. Dashed line is lepton momentum from b, dotted line is from c and dash-dotted is others.*

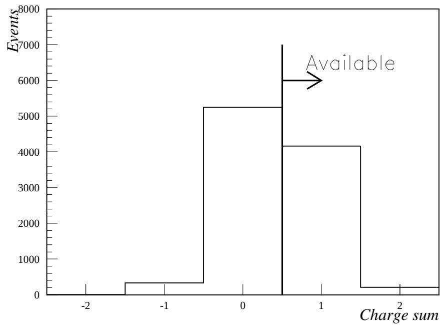

Figure 2.15: *Charge sum of charged kaons. For events where B_{tag} is $\bar{B}^0$, the sign of charge sum is inverted.*

2.4.5 Previous Search

The first direct measurement of $\sin 2\phi_1$ was performed by OPAL collaboration with $B \to J/\psi K_S$ at the energy of M_Z peak. They have measured $\sin 2\phi_1$ with 24 $J/\psi K_S$ events including background. The result was[47]

$$\text{OPAL}: \quad \sin 2\phi_1 = 3.2^{+1.8}_{-2.0}(stat.) \pm 0.5(syst.).$$

The second was measured by CDF collaboration with 198±17 $B \to J/\psi K_S$ events in $p\bar{p}$ collisions at $\sqrt{s} = 1.8$ TeV. The result was [48]

$$\text{CDF}: \qquad \sin 2\phi_1 = 1.8 \pm 1.1(stat.) \pm 0.3(syst.).$$

Both results have a large statistical error, and therefore are not conclusive.

Chapter 3

B-Factory Experiment

In this chapter we describe the B-factory experiment and its apparata, BELLE detector and KEKB accelerator for the measurement of CP violation in neutral B meson decays.

KEKB accelerator is designed to produce a large number of B-mesons. The BELLE detector is optimized to measure the particles from B-meson decays effectively. These are being constructed at High Energy Accelerator Research organization(KEK). The commissioning of the KEKB beams will take place in March 1999. In Section 3.1, a brief introduction of the KEKB accelerator is given. In Section 3.2, the overview of BELLE detector and the description of its principal components are given. The detail of Silicon Vertex Detector(SVD), which has an essential role to measure indirect CP violation, is given in Section 3.3.

3.1 KEKB accelerator

KEKB is an electron-positron collider. The energy of electrons and positrons are 8 GeV and 3.5 GeV, respectively. Hence the center-of-mass energy is 10.58 GeV, which corresponds to $\Upsilon(4S)$ resonance. Electrons have higher energy than positrons in order to avoid ion trapping, which happens only at low energies. The design luminosity is $10^{34} cm^{-2} s^{-1}$ in order to produce 10^8 $\Upsilon(4S)$ a year.

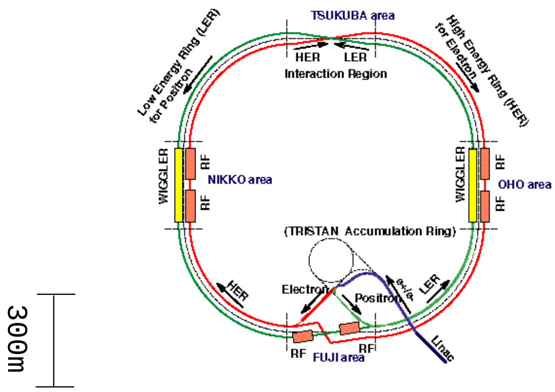

Figure 3.1: *Configuration of the KEKB accelerator system*

Figure 3.1 illustrates the configuration of the two rings of KEKB. The electron ring is called

HER (High Energy Ring) and the positron ring is called LER (Low Energy Ring). These rings are built side by side in the existing TRISTAN tunnel, which has a circumference of about 3 km. KEKB has only one interaction point (IP) in the Tsukuba experimental hall, where the electron and positron beams collide at a finite angle of ± 11mrad. The BELLE detector is installed in this interaction region.

8 GeV electrons (3.5 GeV positrons) can be directly injected from LINAC to the HER (LER) at Fuji and circulate clockwise (anticlockwise). The RF cavities of the HER (LER) are installed at the straight section of Nikko and Oho (Fuji). The two wigglers for LER are also put at Nikko and Oho. They reduce the longitudinal damping time of the LER from 43ms to 23ms, i.e., the same damping time as the HER. To achieve the design luminosity, 5000 bunches are injected to each ring, where the bunch interval is only 2ns (or 60cm). The main parameters of KEKB are summarized in Table 3.1[49].

3.2 BELLE Detector

The configuration of the BELLE detector is shown in Figure 3.2.

Because of the asymmetry of the beam energy, the detector itself also has the asymmetry: *i.e.* it has a larger acceptance in the direction of electrons (which is defined as "the forward region"). The definition of coordinate of detector is shown in Figure 3.3. B-meson decay vertices are measured by a silicon vertex detector (SVD) just outside a cylindrical beryllium beam pipe. Charged particle tracking is provided by a central drift chamber (CDC). Particle identification is provided by dE/dx measurements in the CDC, the aerogel Čerenkov counter (ACC) and the time of flight (TOF) counter arrays outside the CDC. Electromagnetic showers are detected in CsI(Tl) electromagnetic calorimeter (ECL) located inside the superconducting solenoid, which provides magnetic field of 1.5 Tesla. K_L mesons and muon counters (KLM), which consists of resistive plate counters (RPCs), are interspersed in the iron return yoke of the magnet. The expected performance of each detector is summarized in Table 3.2. The detail of each detector component is given in [50]. A brief description of the components follows.

3.2.1 Silicon Vertex Detector(SVD)

The main task of Silicon Vertex Detector (SVD) is to reconstruct the decay vertices of two primary B mesons in order to determine the time between two decays. This determination will allow the measurement of time-dependent CP asymmetry in B^0 decays. Since SVD is one of the most important detector for the simulation performed in this thesis, we will describe the detail of SVD in Section 3.3.

3.2.2 Central Drift Chamber(CDC)

The main role of Central Drift Chamber (CDC) is the detection of charged particles. Specifically, the physics goals of BELLE experiment require a momentum resolution better than $\sigma_{p_t}/p_t \sim 0.5\% \cdot \sqrt{1+p_t^2}$ for all charged particles with $p_t \geq 100MeV/c$ in the polar angle region $17^\circ \leq \theta \leq 150^\circ$. In addition, CDC is expected to provide particle identification information in the form of precise dE/dx measurements for charged particles.

The inner and outer radii are 8 cm and 88 cm, respectively. CDC consists of 50 sense wire layers in total and 3 cathode strip layers. The sense-wire layers are grouped into 11 super layers, where 6 of them are axial and 5 are stereo super layers. Stereo angles range from 42.5 mr to

Table 3.1: *Main parameters of KEKB.*

Ring		LER	HER	
Energy	E	3.5	8.0	GeV
Circumference	C	3016.26		m
Luminosity	$\mathcal{L}$	1×10^{34}		$\mathrm{cm}^{-2}\mathrm{s}^{-1}$
Crossing angle	θ_x	± 11		mrad
Tune shifts	ξ_x/ξ_y	0.039/0.052		
Beta function at IP	β_x^*/β_y^*	0.33/0.01		m
Beam current	I	2.6	1.1	A
Natural bunch length	σ_z	0.4		cm
Energy spread	σ_ε	7.1×10^{-4}	6.7×10^{-4}	
Bunch spacing	s_b	0.59		m
Particle/bunch	N	3.3×10^{10}	1.4×10^{10}	
Emittance	$\varepsilon_x/\varepsilon_y$	$1.8 \times 10^{-8}/3.6 \times 10^{-10}$		m
Synchrotron tune	ν_s	$0.01 \sim 0.02$		
Betatron tune	ν_x/ν_y	45.52/45.08	47.52/43.08	
Momentum compaction factor	α_p	$1 \times 10^{-4} \sim 2 \times 10^{-4}$		
Energy loss/turn	U_o	0.81†/1.5‡	3.5	MeV
RF voltage	V_c	$5 \sim 10$	$10 \sim 20$	MV
RF frequency	f_{RF}	508.887		MHz
Harmonic number	h	5120		
Longitudinal damping time	τ_ε	43†/23‡	23	ms
Total beam power	P_b	2.7†/4.5‡	4.0	MW
Radiation power	P_{SR}	2.1†/4.0‡	3.8	MW
HOM power	P_{HOM}	0.57	0.15	MW
Bending radius	ρ	16.3	104.5	m
Length of bending magnet	ℓ_B	0.915	5.86	m

†: without wigglers, ‡: with wigglers

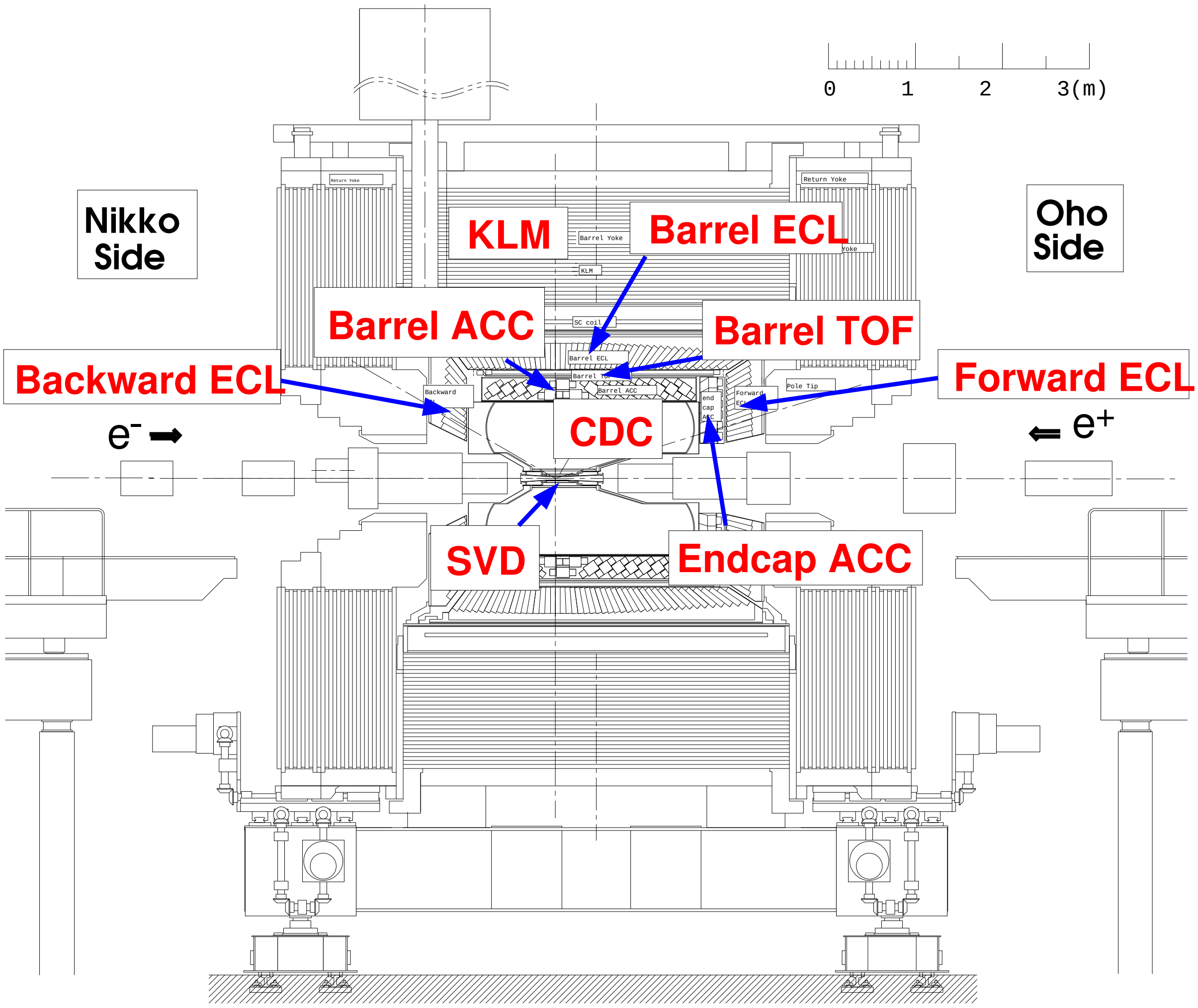

Figure 3.2: *Side view of the BELLE detector.*

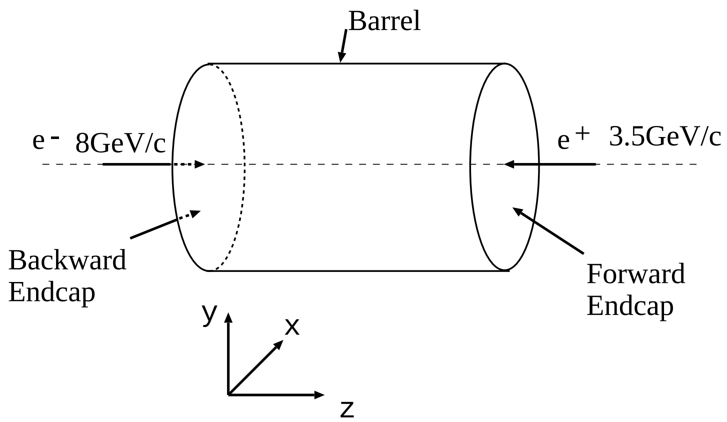

Figure 3.3: *Side view of the BELLE detector.*

72.1 mr. The number of readout channels is 8,400 for anode wires and 1,792 for cathode strips. A 50% helium-50% ethane gas mixture will be used in the chamber to minimize the multiple Coulomb scattering contribution to the momentum resolution.

In the beam test of the full-size CDC prototype, a spatial resolution of 130 μm and a dE/dx resolution of 5.2% for 3.5 GeV/c pions were obtained as shown in Figure 3.4. Figure 3.5(a) shows the pulse height distribution for 0.8 GeV/c charged particles; it is seen that protons and electrons are clearly separated from pions. This figure indicates e/π separation with 4σ or more, which will provide a very powerful handle for electron identification below 1 GeV/c, where E/p method in ECL is not so effective. Measurement of dE/dx as a function of $\beta\gamma$ are shown in Figure 3.5(b).

The details of results of full-size CDC prototype can be found elsewhere[51].

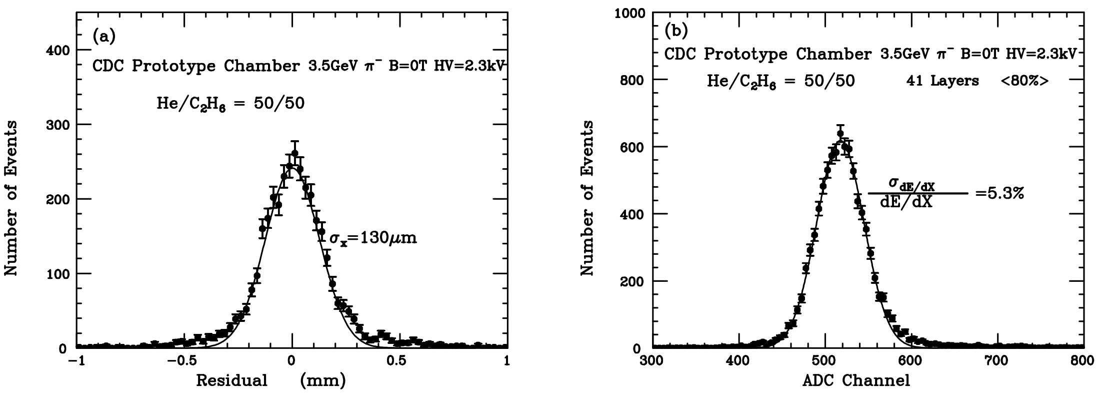

Figure 3.4: *(a) A typical track residual distribution (b) A typical 80% truncated-mean pulse height distribution[52].*

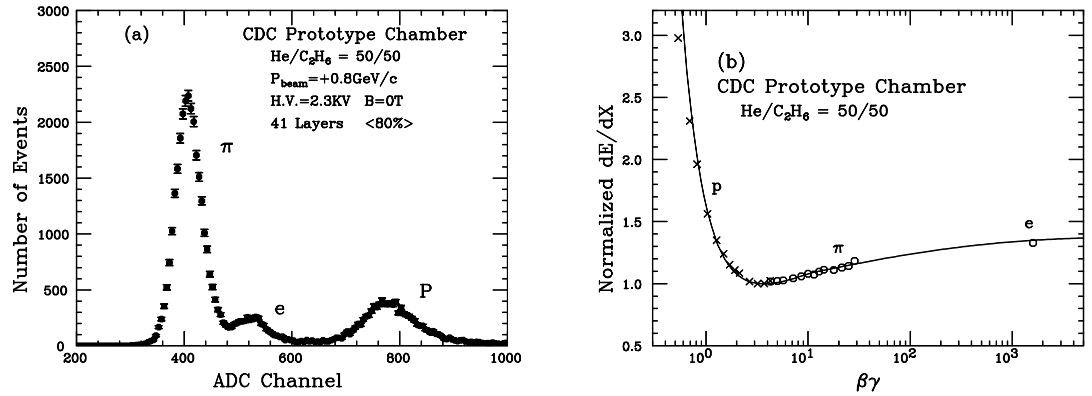

Figure 3.5: *(a) A pulse height distribution for 0.8GeV/c charged particles. (b) A normalized dE/dx distribution as a function of $\beta\gamma$[52].*

3.2.3 Aerogel Čherenkov Counter(ACC)

The BELLE particle identification system comprises an array of time-of-flight counters covering the momentum range of $p \leq$1.2GeV/c, augmented by a Aerogel Čherenkov Counter (ACC) system that extends the coverage upward to the kinematic limit of two-body B-decays such as $B^0 \to \pi^+\pi^-$, to $p = 2.5 \sim 3.5 GeV/c$, depending on polar angle.

Each aerogel counter module consists of silica aerogel radiator module and fine-mesh photo multiplier tubes to detect Čherenkov radiation. The typical aerogel module comprises aerogel tiles contained in a 0.2-mm-thick aluminum box. The inner surface of the box is lined with Goretex sheet as the reflector. The barrel part of ACC consists of 960 aerogel counters; 16-fold segmentation in z and 60-fold segmentation in ϕ. Five different indices of reflection, n = 1.01, 1.013, 1.015, 1.020 and 1.028, are used depending on θ (angle with respect to the beam axis). Each barrel counter is viewed by one or two fine-mesh photo-multipliers (FM-PMT's). The endcap part of ACC has 228 counters in total with n = 1.03 and is structured in five concentric rings with 36-, 36-, 48-, 48-, and 60-fold segmentation from inside to outside. Each endcap counter is viewed by one FM-PMT through an air light guide. The number of readout channels is 1,560 in the barrel and 228 in the endcap.

Figure 3.6 shows the performance of the ACC prototype in a beam test with 1.5 Tesla magnetic field. Pulse-height distributions produced by 3.5GeV/c pions are shown in Figure 3.6(a) together with the results for sub-threshold particles;3.5GeV/c protons with n=1.015 aerogel. Figure 3.6(b) shows the inefficiency and the background contamination as a function of a threshold on the pulse height. We obtained efficiency larger than 98.0% for separating pions from protons. The probability for a proton mis-identified as a pion is less than 2.0%. The background mainly comes from proton-induced knock-on electrons produced on the aluminum box and aerogel material.

A detailed description of ACC and test beam performances can be found elsewhere[53].

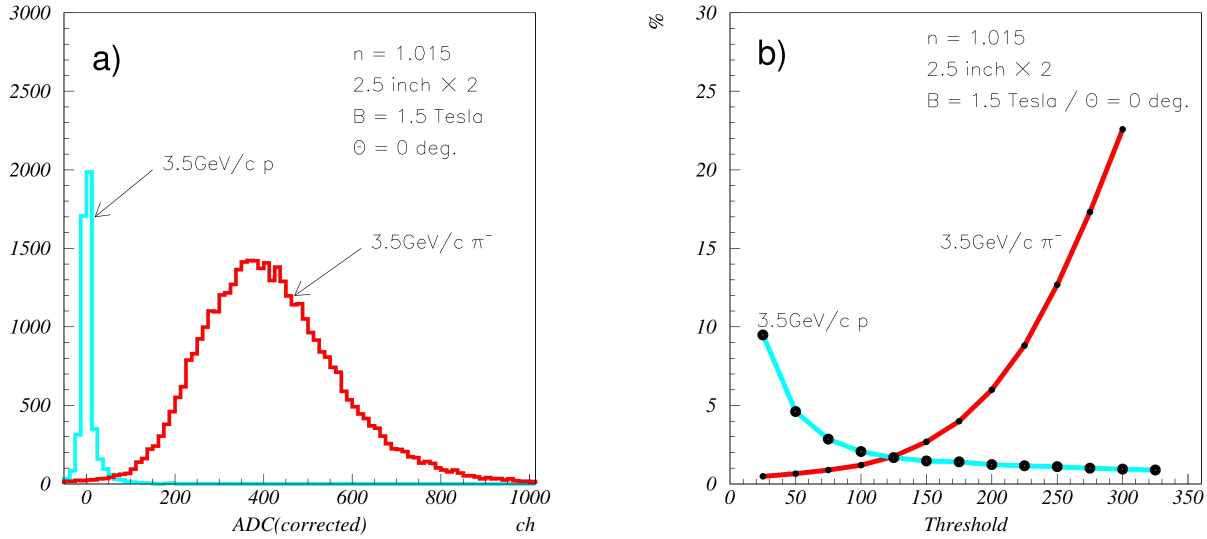

Figure 3.6: *ACC performances: (a) Pulse height distributions obtained with 3.5GeV/c pions and 3.5 GeV/c protons for n=1.015 (b); the inefficiency for pions and the mis-identification probability for protons as a function of the pulse-height threshold values[52].*

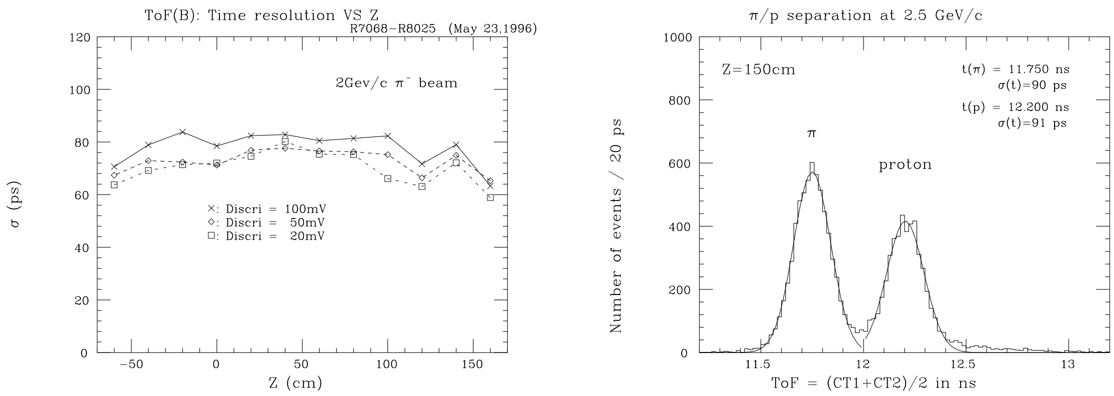

Figure 3.7: *TOF performance:(a) Time resolution of a BELLE TOF module as a function of the hit position and (b) π/p separation as 2.5GeV/c[54].*

3.2.4 Trigger/Time of Flight Counter(TOF)

The Time of Flight counter (TOF) system is required to have a 100ps time resolution in order to provide 3σ π/K separation for momenta below 1.2GeV/c, the region of interest for B-flavor tagging.

One 5-mm-thick Trigger Scintillation Counter (TSC) layer and two 4-cm-thick Time-of-Flight counter (TOF) layer separated by a 2-cm gap are located at r = 120 cm. TOF is segmented into 128 in ϕ sectors and readout by one FM-PMT at each end. TSC's have 64-fold segmentation and are readout from only backward end by a single FM-PMT. The number of readout channels is 256 for TOF and 64 for TSC.

Figure 3.7(a) shows the time resolution of BELLE TOF system as a function of a beam hit position. The results achieved the time resolution that meets the BELLE design goal of 100ps. Figure 3.7(b) demonstrates the separation capability of the BELLE TOF counter. It indicates 5σ separation of π/p at 2.5GeV/c for the beam, which corresponds to 5σ π/K separation at 1.25GeV/c.

3.2.5 Cesium Iodide Calorimeter(ECL)

The main purpose of the electromagnetic calorimeter (ECL) is the detection of photons from B-meson decays with high efficiency and good resolution. Most of the physics goal of BELLE experiment require reconstruction of exclusive B-meson final states. For typical B-meson decays approximately one third of the final state particles are π^0's, thus it is important to have photon detection capabilities that match those for charged particles, especially for low energy photon. π^0 mass resolution is dominated by the photon energy resolution. Sensitivity to and resolution of low energy photons are the critical parameters for the efficient π^0 detection.

Electron identification in BELLE relies primarily on a comparison of the charged particle track momentum and the energy it deposits in the electromagnetic calorimeter. Good energy resolution of the calorimeter results in better hadron rejection.

In order to satisfy these requirements, we chose a design of the electromagnetic calorimeter based on CsI(Tl) crystal. All CsI(Tl) crystals are 30cm (16.1 radiation length) long, and are

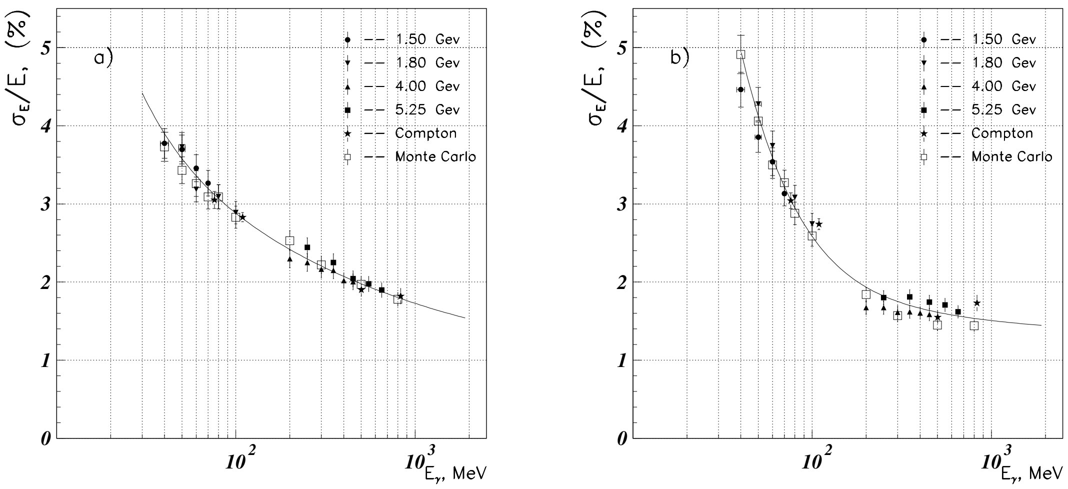

Figure 3.8: *ECL performances: Energy resolution as a function of the incident photon-energy for 3×3(left) and 5×5 matrices. The results obtained from different electron-beam energies are shown by different symbols. The star($\star$) indicates the resolution obtained from the compton-edge. The square is the result from the Monte Carlo simulation[55].*

assembled into a tower structure pointing near the interaction point. The barrel part of ECL has 46-fold segmentation in θ and 144-fold segmentation in ϕ.

The forward(backward) endcap part of ECL has 13-(10-) fold segmentation in θ and the ϕ segmentation varies from 48 to 144 (64 to 144). The barrel part has 6,624 crystals and the forward (backward) endcap part has 1,152(960) crystals. Each crystal is readout by two 10mm$\times$20mm photo-diodes. Total readout channel is 17,472. The inner radius of the barrel part is 125cm. The forward(backward) endcap part starts at z=+196cm(-102cm).

Several tests were performed with a photon beam provided from the backward Compton scattering between electrons and laser photon [55]. The energy resolution is given in Figure 3.8 for 3×3(left) and 5×5(right) CsI matrices in the photon-energy region from 40 up to 800MeV/c^2.

A detailed description of ECL performances can be found elsewhere[56].

3.2.6 Solenoid magnet

The magnetic field causes the charged particles to follow a helical path. Its curvature is related to the momentum of the particles. The coil consists of a single layer of an aluminum-stabilized superconductor coil, a niobium-titanium-copper alloy embedded in a high purity aluminum stabilizer. It is wound around the inner surface of an aluminum support cylinder. Indirect cooling is provided by liquid helium circulating through a single tube welded on the outer surface of the support structure. A super conducting solenoid magnet provides a magnetic field strength of 1.5 Tesla in a cylindrical volume of 3.4 m in diameter and 4.4 m in length. The field value in the CDC volume is expected to vary by 2.0%.

3.2.7 K_L and Muon Detector(KLM)

The K_L and Muon Detector(KLM) is designed to detect neutral kaons and muons with momenta above 600 MeV/c. The detection of K_L is needed to reconstruct $B \to J/\psi K_L$. Muons are used in the CP violation measurements to identify the flavor tagging B meson and to reconstruct $J/\psi \to \mu^+\mu^-$.

Resistive Plate Counter (RPC) is utilized for BELLE KLM system. RPC's are essentially planar spark counters wherein the avalanche induced by an incident charged particle is quenched when the limited amount of charge on the inner surfaces of highly resistive electrodes is exhausted. Having a particle penetrating an RPC, it becomes locally deadend for short time until the inner surfaces can recharge through the resistive material. As resistive material for RPC, BELLE KLM employs glass, which has a bulk resistivity of about $10^{12} - 10^{13}\Omega$-cm.

The KLM detector consists of a barrel part and two endcap parts. Fourteen layers of 4.7 cm thick iron plate and each RPC superlayer contains two RPC planes and provides θ and ϕ information. The barrel part has one additional RPC superlayer in front of the first iron plate. RPC is made of 2-mm thick glass electrodes. The iron plate is an absorber material for KLM and also serves as a return path of the magnetic flux provided by solenoid magnet. K_L is tagged with hadronic interactions in the ECL, the coil or KLM itself. Nominally, the detector covers the polar angle range of $25° \leq \theta \leq 145°$. Signals are readout by $\approx$5 cm wide cathode strips in both θ and ϕ. The number of readout channels is 21,856 in barrel and 16,128 in endcap.

3.2.8 Trigger and Data Acquisition

Figure 3.9 shows a schematic view of the trigger system. The trigger information from individual detector components is formed in parallel and combined at the final stage (global decision logic, GDL). In the full-bucket operation of KEKB, the time between beam crossing is only 2 ns and trigger system works in the pipelined manner in order to avoid large dead-time losses. The GDL provides the trigger signals 2.2μs delayed from the actual event crossing.

The global scheme of the data acquisition system is shown in Figure3.10. The data from each subsystem are combined into a single event by the eventbuilder. The output of the event builder is then transferred to the online computer farm.

The allocated data digitization time should be less than 200 μs in order to achieve the dead time less than 10% at 500 Hz trigger rate. Once the data taking is done, full event records are reconstructed in an event builder system before being transferred to the online computer farm where a more complete on line event reconstruction is done before the data is stored in the tapes by the mass storage system.

3.3 Silicon Vertex Detector (SVD)

At the B-Factory experiment, the precision vertex detection is essential to observe the asymmetry in the proper-time-difference of two B-mesons. We achieve this accuracy with using Silicon Vertex Detector (SVD). While the wire drift chamber has worse resolution than 100 μm from sense wires for only $r-\phi$ direction, the resolution of SVD is much better : the intrinsic resolution is expected to be a few tens of microns. Therefore it is suitable for measurement of the vertex of B-mesons in z-direction. BELLE SVD is situated just inside CDC and reconstructs precise tracks of charged particles with combining CDC measurement.

Table 3.2: *Performance parameters of the BELLE detector.*

Detector	Type	Configuration	Readout	Performance
Beam pipe	Beryllium double-wall	Cylindrical, r=2.3 cm 0.5mm Be/2mm He /0.5mm Be		Helium gas cooled
SVD	Double Sided Si Strip	300 μm-thick, 3 layers r = 3.0 - 5.8 cm Length = 22 - 34 cm	81.9 K	$\sigma_{\Delta z} \sim 105$ μm
CDC	Small Cell Drift Chamber	Anode: 52 layers Cathode: 3 layers r = 8.5 - 90 cm -77$\leq z \leq$ 160 cm	A: 8.4 K C: 1.5 K	$\sigma_{r\phi}$ = 130 μm $\sigma_z = 200 \sim 1,400\mu$m σ_{p_t}/p_t =0.3%$\sqrt{p_t^2+1}$ $\sigma_{dE/dx}$ = 6%
ACC	n : 1.01 $\sim$ 1.03 Silica Aerogel	$\sim$12x12x12 cm^3 blocks 960 barrel / 228 endcap FM-PMT readout	1,788	$\mu_{eff} \geq 6$ K/π 1.2<p<3.5GeV/c
TOF	Scintillator	128 ϕ segmentation r = 120 cm, 3 m-long	128$\times$2	σ_t = 100 ps K/π up to 1.2GeV/c
ECL	CsI	Towered structure $\sim$ 5.5x5.5x30 cm^3 crystals Barrel: r = 125 - 162 cm Endcap: z = -102 and +196 cm	6,624 1,152(f) 960(b)	σ_E/E= 0.67%/$\sqrt{E}\oplus$1.8% σ_{pos}=0.5 cm/$\sqrt{E}$ E in GeV
MAGNET	super conducting	inn.rad. = 170 cm		B = 1.5 T
KLM	Resistive Plate c.	14layers (5cm Fe+4cm gap) two RPCs in each gap θ and ϕ strips	θ:16 K ϕ:16 K	$\Delta\phi$=$\Delta\theta$=30mr for K_L σ_t=1ns 1% hadron fakes

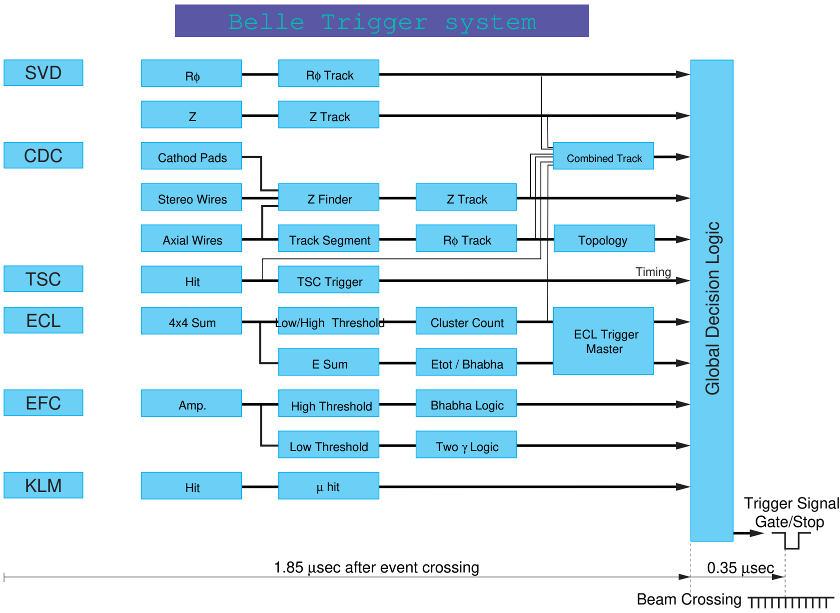

Figure 3.9: *Block diagram of BELLE trigger system. SVD trigger is optional for future SVD system.*

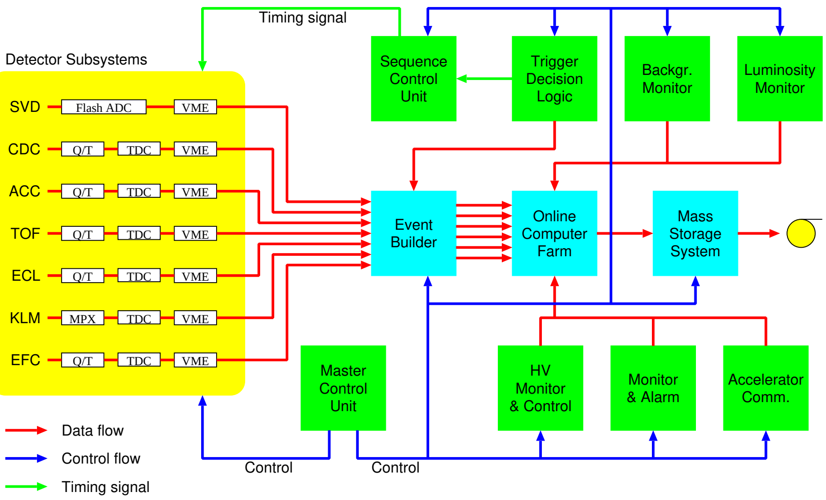

Figure 3.10: *Block diagram of BELLE data acquisition system.*

The precise vertex information will also be useful for eliminating continuum events and reducing combinatorial backgrounds and for measuring the life time of the short lived particles[57].

In this section, required capability, configuration, readout system and expected performance will be given. The more detail of BELLE SVD is described elsewhere[58].

3.3.1 Requirement for Silicon Vertex Detector

The primary goal for the vertex detector is the measurement of an asymmetry in the proper time distribution when one of $B\bar{B}$ pair decays into CP eigenstate. The proper time difference Δt is given by

$$\Delta t \simeq \Delta z / c\beta\gamma, \tag{3.1}$$

where $\beta\gamma$ is the Lorentz boost factor due to the asymmetric beam energy ($\beta\gamma = 0.42$ at KEKB) and Δz is the distance between the decay vertices of the two B mesons along the beam direction. At the KEKB situation, mean decay length of B meson should be about 200μm. The proper time distribution of $B \to J/\psi K_S$ was already shown in Figure 2.11. The difference between the B^0 and $\bar{B}^0$, or positive and negative time scale, reflects the CP asymmetry. The curves in the figure are drawn assuming perfect vertex-position resolution. When the finite time resolution is included, the difference between the positive and negative time scale is diluted. The errors of measured vertex point reduces the sensitivity of the CP violation measurement. Figure 3.11 shows the relative integrated luminosity required for observing CP asymmetry in the $B \to J/\psi K_S$ with 3σ significance for different Δt resolutions. The penalty for resolution of $\Delta t/\tau_B = 0.5$ (as compared to perfect vertex resolution) is 30% increase in luminosity. If $\Delta t/\tau_B$ further degrades from 0.5 to 1.0, another 70% increase in luminosity is required. We expect to achieve $\Delta t/\tau_B \leq 0.5$, corresponding to about 100μm position resolution in the beam direction.

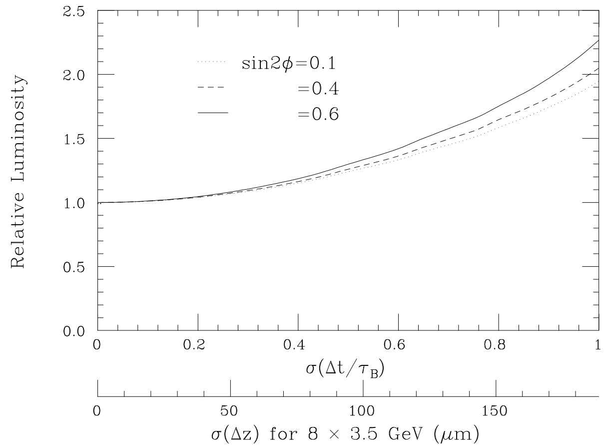

Figure 3.11: *Required integrated luminosity as a function of the Δz resolution for three different values of* $\sin 2\phi_1$.

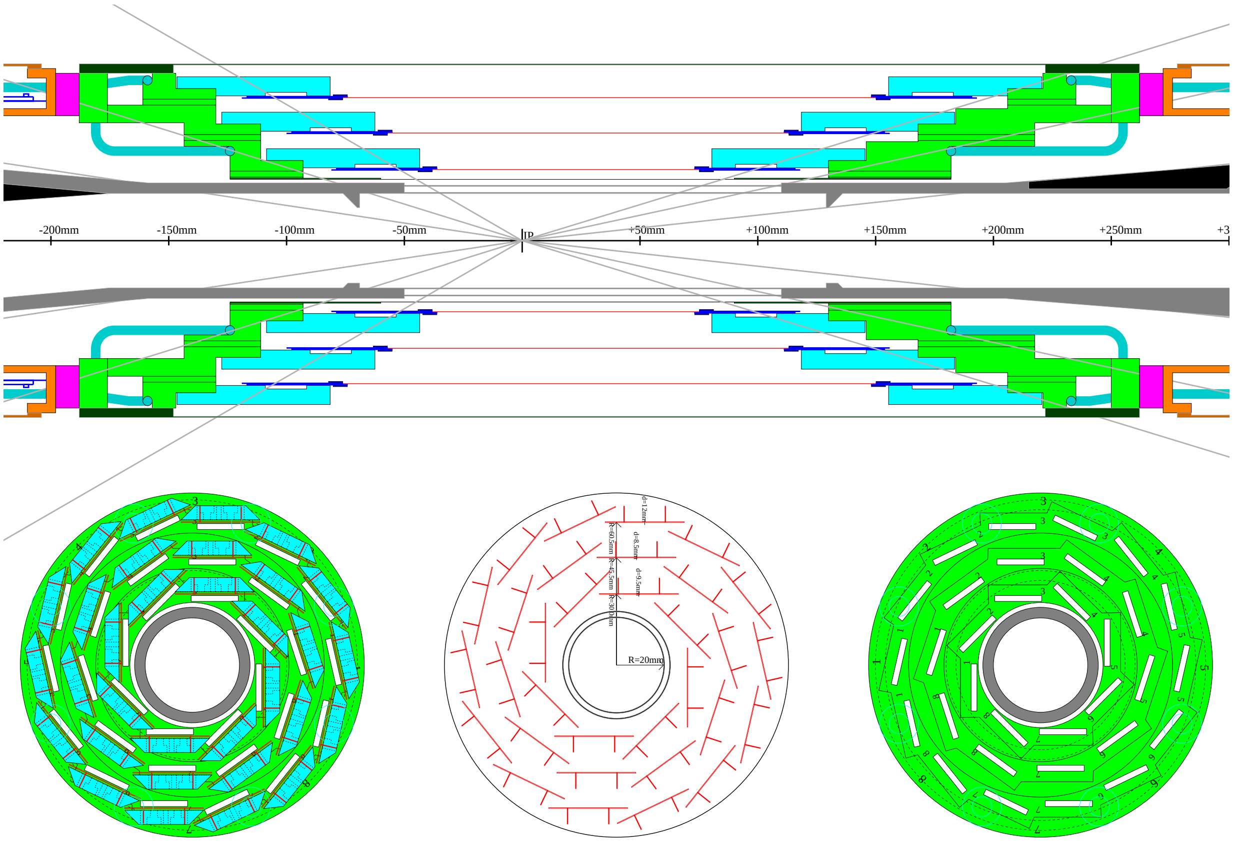

Figure 3.12: *The configuration of BELLE silicon vertex detector.*

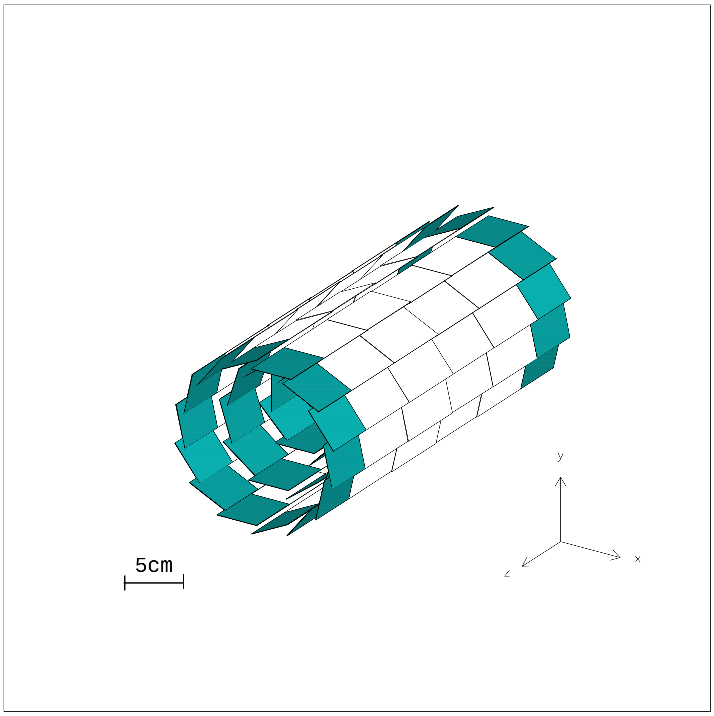

Figure 3.13: *The configuration of SVD ladders. The hatched layers are hybrid board, which have the LSI chip for readout.*

3.3.2 Detector Configuration

The configuration of BELLE SVD is shown in Figure 3.12 and 3.13. SVD has three cylindrical layers consisting of units of the silicon sensors. The position of each layer is 3.0 cm, 4.55 cm and 6.05 cm in r direction, respectively. The three layers have 8, 10 and 14 sensor ladders in ϕ. In order to make precise alignment with particle tracks and cover the non-active region at the edge of each sensor, all silicon sensors have some overlap with one another. The sensor ladders have 2, 3 and 4 unit sensors to cover the acceptance of 21 to 140 degree in polar angle in layer 1, 2 and 3, respectively.

At the BELLE experiment, the transverse momentum distribution of charged particles from B decays peaks around 200 MeV/c, which makes multiple Coulomb scattering of great importance. For reduction of the materials, all readout electronics are located outside the acceptance region.

Each sensor ladder is divided into two electrically-separated long and short half-ladders. Each long half-ladder contains two Double-sided Silicon Strip Detectors (DSSDs) and two hybrid cards. Each short half-ladder contains a DSSD and two hybrid cards. As shown in Figure 3.14, each inner sensor ladder consists of two short half-ladders. Middle sensor ladders consist of a short and a long half-ladder. Outer sensor ladders have two long half-ladders.

3.3.3 Design of Unit Silicon Sensor

As a unit sensor, we selected DSSDs, where all sensors have the same design. We used the DSSD fabricated by HAMAMATSU Photonics (HPK) originally designed for DELPHI micro

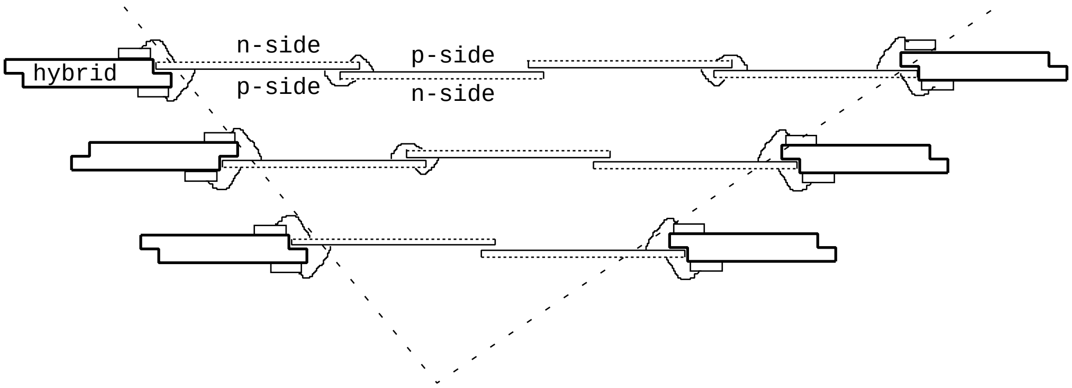

Figure 3.14: *The Schematic view of ladder assemble.*

vertex detector[59]. This DSSD is called S6936[60]. Figure 3.15 shows the schematic structure of DSSD. It has a size of 57.5×33.5mm. The one side (= n-side) of DSSDs has n^+-strips oriented perpendicular to the beam direction to measure the z coordinate and the other side (= p-side) with longitudinal p^+-strips, allows ϕ coordinate measurement. The bias voltage of 80V is supplied to the n-side and p-side is grounded. The n^+-strips are interleaved by p^+ implants (called p-stops) to separate the consecutive strips electrically. The thickness is $300 \pm 15\mu$m. Figure 3.16 shows the readout scheme of DSSD. On both sides, the number of readout channels is a half of the number of strips. On the p-side, every second strip is connected to a readout channel. The remaining half strips are floating, which are biased but not connected to preamplifiers, capacitively dividing the charge between adjacent channels, which are connected to the readout system. On the n-side, the consecutive two strips are connected to one readout channel. In order to change direction of readout channel of n-strips to the direction of p-strips, Double Metal Layer (DML) structure is adopted on the n-side.

Table 3.3 shows revised BELLE specification for S6936. The average resistance of poly-silicon bias resistor is raised from original specification[1]to 35MΩ with an allowed-minimum of 25MΩ. Schematic view of strips on both sides is shown in Figure 3.17.

Strips on the n-side for z measurement has larger noise than that on the p-side for ϕ measurement. In order to minimize the noise of the long half-ladder, different sides of the two DSSDs are connected *i.e.* p-strips on one detector are wire-bonded to n-strips on the other detector(p-n flipped) as shown in Figure 3.14.

BELLE SVD will have 102 DSSDs in total with a total of 81,920 readout channels.

3.3.4 Readout System

The readout system of SVD consists of three parts. The charge signal from each silicon sensor is amplified by a pre-amplifier in a LSI chip on the hybrid card. From this frontend electronics, the current signal is sent to the repeater system 2m apart from SVD. The repeater system converts the current signal to the voltage signal, amplifies and sends it to the backend part in the electronics hut 30m apart from BELLE detector. A schematic view of the readout system is shown in Figure 3.18.

[1]The original specification of S6936 guaranteed 10MΩ for p-side and 20MΩ for n-side as minimum values.

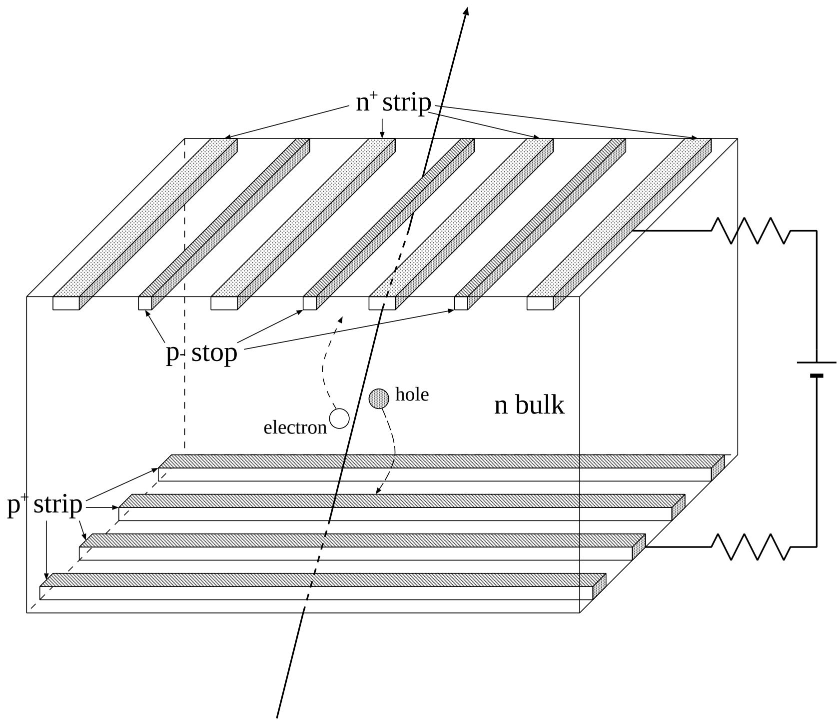

Figure 3.15: *The schematic view of double sided silicon strip detector.*

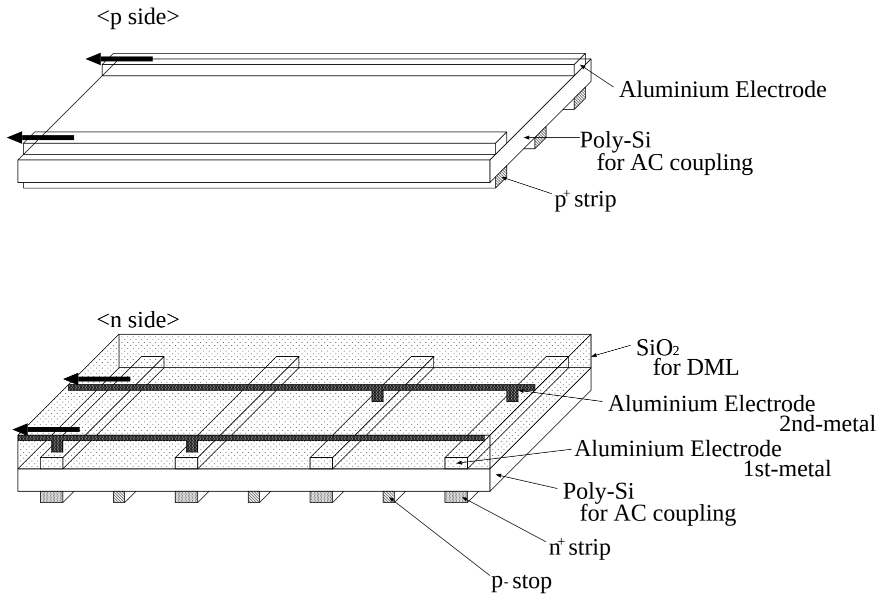

Figure 3.16: *The readout scheme on each side of DSSD. On the n-side, Double Metal Layer (DML) structure change the direction of readout electrode to same direction as p-side.*

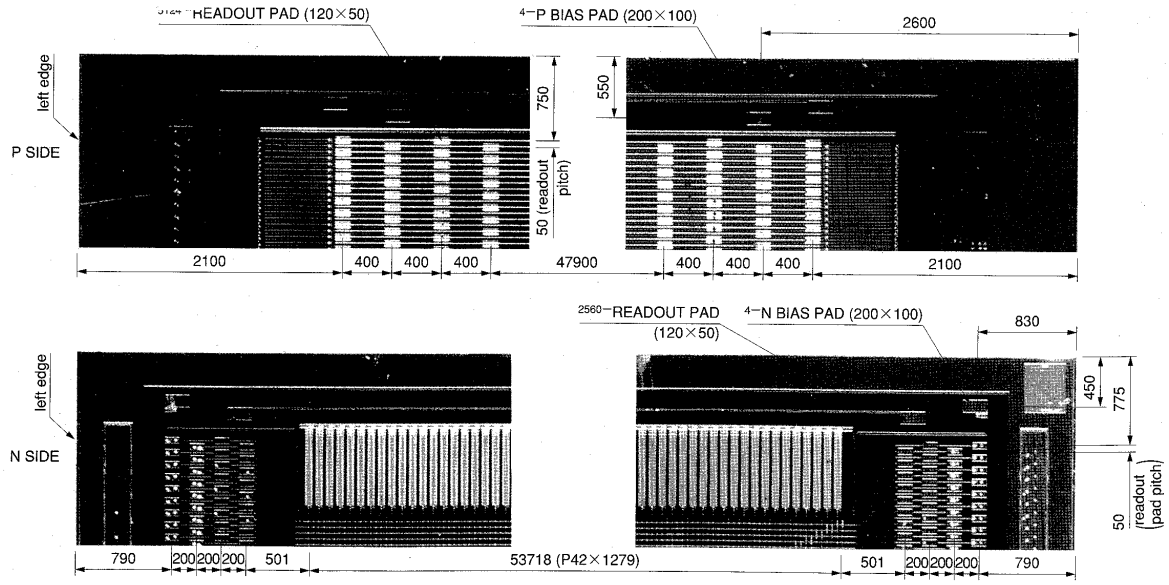

Figure 3.17: *The S6936 silicon sensor. Top: p-side. Bottom: n-side.*

Table 3.3: *Specifications for S6936[60].*

Parameter	p-side	n-side
Chip size	57.5mm×33.5mm	
Active Area	54.5mm×32.025mm	53.76mm×32.04mm
Thickness	$300 \pm 15\mu$m	
Readout(Bias) method	AC(Poly-Si)	AC(Poly-Si)
Strip pitch	25μm	42μm
Number of strips	1281	1280
Number of readout strips	641	640
Strip width	8μm	8μm
Readout electrode width	8μm	14μm
DML insulator material, thickness	N/A	SiO_2, 5μm
DML trace pitch, width	N/A	48μm,8μm
Full depletion voltage (Vfd)	80V Max	
Breakdown voltage	100V Min	
Leakage current at Vfd	2μA Max	
Bias Resistance	25MΩ Min	25MΩ Min
Coupling capacitance at 10kHz	55pF	40pF
Breakdown voltage of coupling capacitor	50V Min	50V Min
Load capacitance at 1MHz	8pF	20pF
Number of NG channel	19 Max	19 Max
Passivation	SiO_2	SiO_2

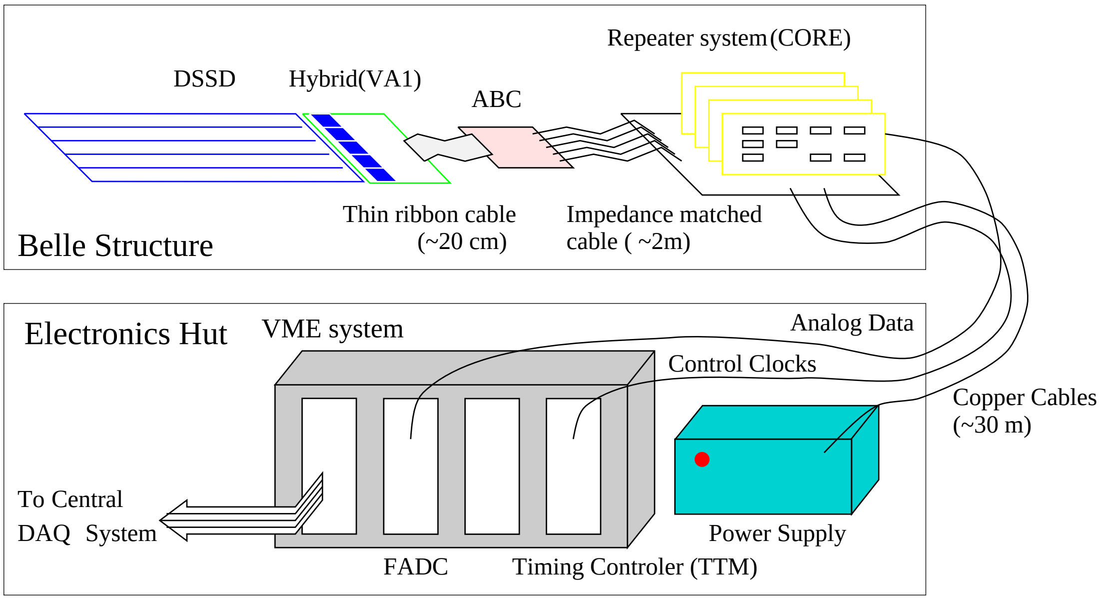

Figure 3.18: *The readout scheme of BELLE SVD.*

Frontend electronics

As a frontend electronics circuit, we have chosen VA1 chip[61], which was developed at CERN. The VA1 is a 128-channel CMOS integrated circuit that is specially designed for the read-out of silicon strip detectors and other signal devices. It has excellent noise characteristics (ENC=$165e^{-} + 6.1e^{-}$/pF at 2.5μs shaping time), and consumes only 1.2mW/channel. Signals from the strips of DSSDs are amplified by charge sensitive preamplifiers, followed by shapers. The output of the shaper is fed into a track and hold circuitry, which consists of a capacitor and a CMOS switch. The voltage on the capacitors is connected to output amplifiers. All 128 channels in the chip are readout by single output amplifier with a shift register. The signal from all channels can be read by a single ADC in this way. Five VA1 chips are put on a hybrid card and all channels are connected to the strips of a silicon sensor with thin wires.

Repeater System

The repeater system has three roles. It receives analog signals from VA1 through hybrid cards and transmits them to the backend part. All control and timing signals are optimized and transferred through the repeater system. Powers for frontend electronics and detector bias are also distributed by the repeater system.

Backend in Electronics Hut

Backend electronics consists of flash ADCs (FADC) and trigger timing modules (TTM). TTMs distribute clocks and other digital control signals required for the VA1 readout sequence. The signals from the repeater system are digitized by FADCs. We take signals from all VA1 chips at a rate of 5 MHz. In addition, FADC must also perform a zero suppression so as to reduce the dataflow in data acquisition system in order to achieve the rate required by BELLE Data acquisition. FADC system contains digital signal processor (DSP) and first-in/first-out (FIFO) memory. To reduce the data size, DSP calculates and subtracts the offset from signal for each channel. The signal lower than given threshold is rejected.

3.3.5 Summary

The construction of SVD was already completed in November 1998. Figure 3.19 shows the cosmic ray event taken with BELLE CDC and SVD. The SVD system was installed to BELLE structure in December 1998. SVD and other sub-detectors of BELLE will start to take physics data in the beginning of JFY 1999.

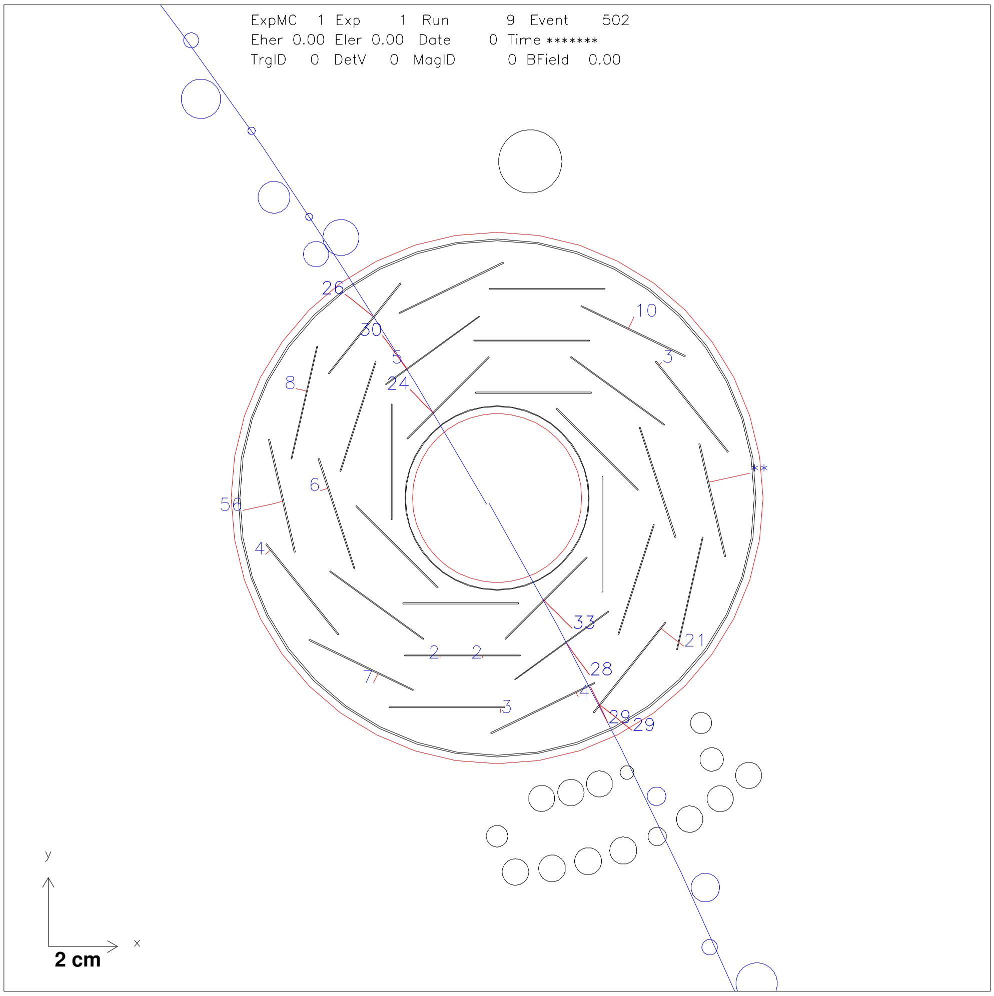

Figure 3.19: *The cosmic ray event with BELLE CDC and SVD. This event was taken inside BELLE structure in January 1999.*

Chapter 4

Testbeam Experiment for Silicon Strip Detectors

In this chapter, we will describe the results of beam tests for silicon strip detectors carried out as R & D for BELLE SVD.

In Section 4.1, the motivation of the beam test is described. The sample detectors and testbeam setup are described in Section 4.2. The data processing is explained in Section 4.3. The results of beam tests are given in Section 4.4. We also describe the performance test of a real-size Double sided Silicon Strip Detector (DSSD) for BELLE SVD in Section 4.5. Finally, we summarize this chapter in Section 4.6.

4.1 Motivation of Beam Test

BELLE SVD is required to have the vertex resolution of about 100μm for the z distance of two B vertices as mentioned in Section 3.3. We use DSSD as unit silicon sensor. When a particle penetrates DSSD, p-strips measure ϕ position and n^+-strips measure z-position(see Section 3.3.3).

The vertex resolution of SVD depends on the intrinsic spatial resolution, especially that of n-strips, of a unit silicon sensor. The spatial resolution of Silicon Strip Detector (SSD) is better with a narrower strip pitch for a small incident angle. According to our simulation study[62], however, there is a possibility that better resolution is obtained with wider strip pitch for a particle with large incident angles.

In addition, the adoption of the wide pitch detector reduces the number of strips and detector capacitance, which results in the better S/N ratio and less number of fake hits from electric noise[1].

Since the configuration of BELLE SVD has cylindrical structure, the maximum incident angle reaches 69° for n^+-strips for z measurement[2]. However, no experimental measurement on the spatial resolution existed for inclined tracks with such a large incident angle.

The main purpose of this testbeam experiment was to measure the spatial resolution of SSDs with various strip pitches at various incident angles. This was an indispensable information to determine the strip pitch of BELLE SVD for z-coordinate measurement.

[1] We require detector to have the S/N ratio of more than 15.

[2] For p-strips ($r-\phi$), the maximum incident angle is about 45°. The spatial resolution in this condition was already measured[63].

Table 4.1: *The parameters of the sample detectors.*

Sample	A	B	C
Strip pitch:p[μm]	50	125	250
Number of strips	200	80	40
Strip width:Wn[μm]	10	20	40
Electrode width:Wr[μm]	10	20	20
P-stop width:Wp[μm]	30	95	200
Thickness[μm]	300		
Active area	$10.0\times10.0mm^2$		
Bias resistance	20MΩ		

In addition to the purpose described above, an important goal of the testbeam experiment was to check the correctness of our Monte Carlo simulation program. This was carried out by comparing the intrinsic spatial resolution with the one predicted by Monte Carlo simulation.

Finally, is was also required to evaluate the performance of a large-area DSSD selected as the BELLE SVD unit sensor to check validity of our choice.

4.2 Detector and Testbeam Setup

4.2.1 Detectors

In order to study a spatial resolution of detector at large incident angles and with wide strip pitches for n^+ strip, we used three sample detectors, denoted as type-A, B and C detectors, fabricated by HAMAMATSU PHOTONICS K.K.[60].

The structure of these detectors is shown in Figure 4.1. The parameters of these detectors are shown in Table 4.1. The area of type-A$\sim$C detectors is $10.0 \times 10.0\text{mm}^2$. These detectors are single sided with n^- bulk and have n^+-strips on the ohmic side, whose strip pitches are 50, 125 and 250μm, respectively. P-stops are adopted between strips to separate the consecutive strips electrically. The bias voltage was $-70V$ on the p-side, while the n-side was grounded.

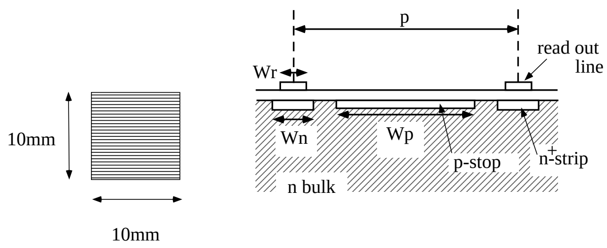

Figure 4.1: *The schematic view and parameters of type-A detector. These detectors are single sided and have only n^+-strips on n-side.*

The charge signal from these detectors is readout with a multiplexor charge amplifier VLSI chip. These detectors have VA2 chips[61] which have similar performance as that of VA1, which is selected for BELLE SVD. The readout rate was 2.5MHz for each strip.

These sample detectors were tested in advance with β source and Infra-red laser. The results of the tests are described elsewhere[64].

4.2.2 Testbeam setup

The beamtest was performed at the $\pi 2$ beam line at KEK(National Laboratory for High Energy Physics) 12GeV Proton Synchrotron in May and November 1995. During the data taking period, we used a π^- beam with momentum of 2.0GeV/c for all sample detectors. Figure 4.2 illustrates our testbeam setup.

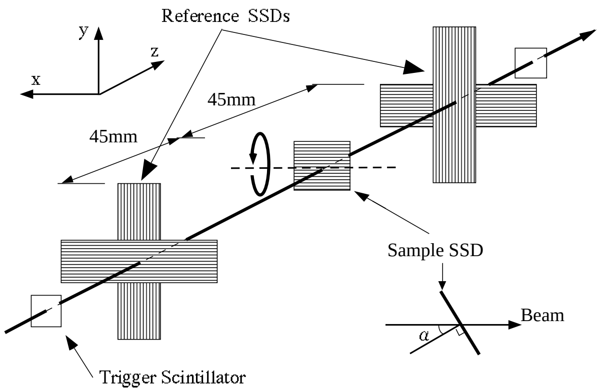

Figure 4.2: *The testbeam setup.*

Four reference SSDs are located upstream and downstream to reconstruct a particle track precisely. These reference SSDs are single-sided and have an area of $12.8\times64.0\text{mm}^2$ each. The p^+-strip pitch is 25μm and we read out every other strip, *i.e.* the readout pitch is 50μm. The detail of these reference SSDs is described elsewhere[63]. The sample detectors were mounted between upstream and downstream reference SSDs and can be rotated about the axis which is parallel to the n-strips. Data have been taken at eleven different incident angles ranging from $0°$ to $70°$ for the type-A and at ten different incident angles ranging from $0°$ to $75°$ for the type-B and C.

4.3 Raw Data Processing

For each event and each channel, the pulse-height and the noise are calculated with subtracting the offset and the common mode noise from ADC counts off-line[63].

We calculate the hit position on the sample detector with the following steps;

(1) Data sparsification

(2) Cluster finding

(3) δ-ray cut

(4) Position calculation

The details of these algorithms are described below.

Calculating hit position on reference detector is done in the same way as sample detectors but without steps (1) and (3).

Only if we find clusters on the whole set of four reference detectors (*i.e.* 4-fold coincidence), a track is reconstructed by interpolating hit positions of the upstream and downstream detectors. Since we measure such a fine spatial resolution, a few tens of μm, precise alignment of this setup is very important. We have aligned the position of the sample SSD using data of the beam tracks. The method of alignment is described in Appendix A in detail.

4.3.1 Data sparsification

In the readout system of BELLE-SVD, the sparse data scan will be adopted. In this analysis, therefore, we only used the information of the strips which had larger charge than 3.7 times the noise level and its both sides. The signals on the rest of strips were zero-suppressed.

4.3.2 Cluster finding algorithm

The charge induced by a penetrating particle is collected by several consecutive strips, which form a cluster. In order to find the cluster, we first look for consecutive strips with the given width, whose sum of charges is higher than the given threshold. The threshold was defined as $5 \times \sqrt{\sum_i {\sigma_i}^2}$, where σ_i is the *r.m.s.* noise of each strip. The cluster width, N_w, was defined as

$$N_w = 2 + Int(1.1 \times \frac{D}{p} \times \tan\alpha), \tag{4.1}$$

where D is the thickness of the silicon wafer (300μm), p a pitch of the readout strip, α the incident angle, and $Int(x)$ the nearest integer to x. If there is more than one cluster, we choose a cluster which has the largest charge.

4.3.3 δ-ray cut

When a δ-ray electron is generated, larger charge is deposited on the neighbor strips than other strips in the cluster. This effect is large for particles with a large incident angle. In order to reject the effect of δ-rays, we applied the following algorithm as a δ-ray cut for incident angles larger than 40°. When Q_i is greater than $< Q > +\sigma_i$, Q_i is changed to $< Q >= \sum Q_i/N_w$.

4.3.4 Position finding algorithm

For computing the impact position of the particle passing through the detector, we used three different methods, *i.e.* (1) the analog centroid method(AC-method), (2) the analog head-tail method(AHT-method) and (3) the non-linear method on η(ETA-method)[65].

Analog centroid method

In the AC-method, the hit position, X_{AC}, is given by

$$X_{AC} = \frac{\sum\limits_{i \in cluster} x^i Q^i}{\sum\limits_{i \in cluster} Q^i}, \tag{4.2}$$

where x^i is each strip position defined at the center and Q^i the charge collected on each strip. In the AC-method, we used the information of the strips with charge larger than σ_i.

Analog head-tail method

For a large incident angle, the charge generated by a particle spreads among many strips. We assumed that the charge collected by strips was proportional to the path length of a particle in a SSD. In this case, the charges collected by strips except both edges of the cluster do not contain position information. Therefore including this information (which is the case in the AC method) simply degrades the spatial resolution. In the AHT-method, we used the information from strips on both edges only to solve this problem. We defined the head(tail) strip as a strip which had the smallest(largest) strip number and which had charge larger than three times the noise level in a cluster. The hit position, X_{AHT}, is then given by

$$X_{AHT} = \frac{x_h + x_t}{2} + \frac{Q_t - Q_h}{2Q_{AV}} \times p, \tag{4.3}$$

where $x_h(x_t)$ is the position of the head(tail) strip and defined at the center of the strip. The charge collected on the head(tail) strip is $Q_h(Q_t)$. The average pulse height on the cluster is Q_{AV}.

ETA method

For a small incident angle, the charge generated by a particle is collected by almost a single strip. Figure 4.3(a) shows a simulation of the charge division between consecutive two strips. We define η as

$$\eta = \frac{Q_{right}}{Q_{left} + Q_{right}}, \tag{4.4}$$

where $Q_{left}(Q_{right})$ is the charge collected on the left(right) side strip of the hitpoint.

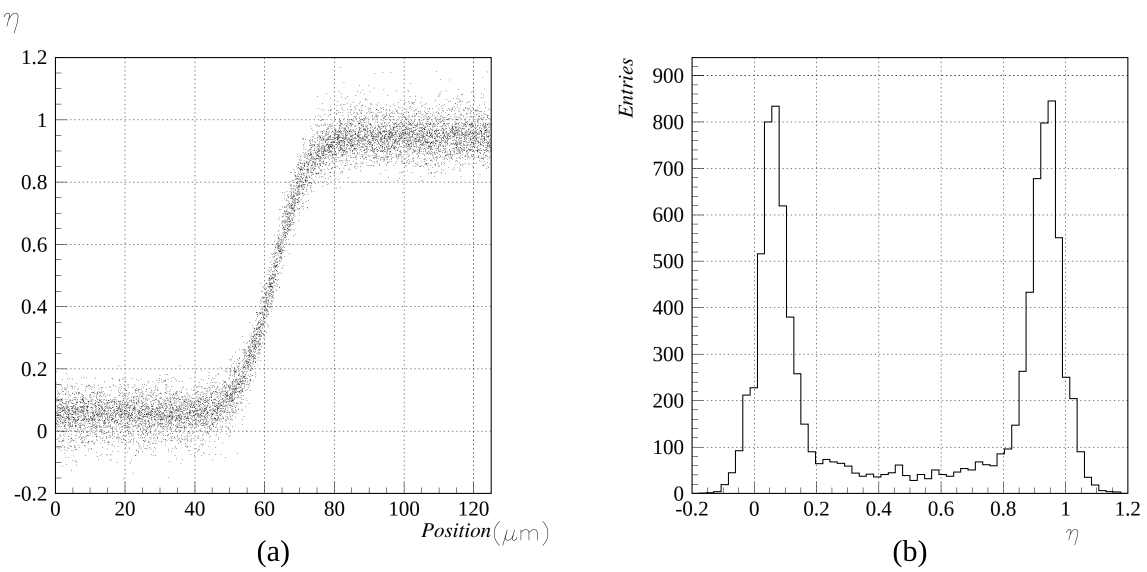

Figure 4.3: *Simulation of (a) Charge division and (b) η distribution for the type-B(125μm).*

In the ETA-method, the hit position, X_η, is given by

$$X_\eta = pf(\eta) + x_{left}, \tag{4.5}$$

where p is the readout pitch, $f(\eta)$ is an arbitrary growing function of η, with $f(0) = 0$ and $f(1) = 1$. We defined $f(\eta)$ as

$$f(\eta_0) = \frac{\int_0^{\eta_0} \frac{dN}{d\eta} d\eta}{\int_0^1 \frac{dN}{d\eta} d\eta}, \tag{4.6}$$

where $dN/d\eta$ is the differential η distribution. The function is obtained with fitting Figure 4.3(b) with the complex Gaussian.

4.4 Results

4.4.1 Signal distribution, S/N ratio and Uniformity

Figure 4.4 shows a pulse-height distribution of the type-A (50μm) detector with zero incident angle($\alpha = 0°$). The S/N ratio we obtained was 18.4 ± 0.5 for the type-A, 20.2 ± 0.5 for the type-B and 16.8 ± 0.5 for the type-C, respectively.

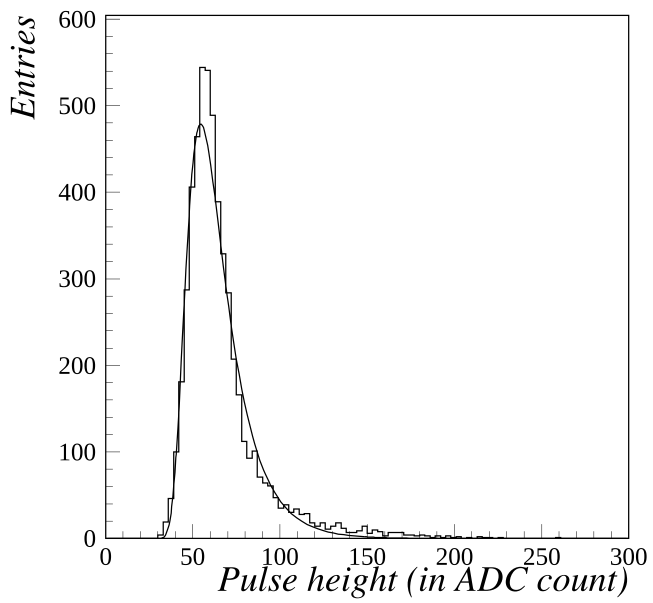

Figure 4.4: *Signal distribution with the type-A(50 μm) detector.*

To establish the design of SSD with the wide strip pitch, it was necessary to check that there was no sizable loss of detection efficiency since there could be a region of weak electric field in the middle of n^+-strips where efficiency of charge collection might be lower. We check the uniformity of charge collection efficiency for the type-C (250μm) detector, which has the widest strip pitch. Figure 4.5 is a scatter plot of the pulse-height vs. the position of incidence obtained with the reference SSDs. In the figure the both ends (i.e. Position = 0, 250μm) correspond to the center of strips. It is seen that there is no sizable loss of charges between two strips.

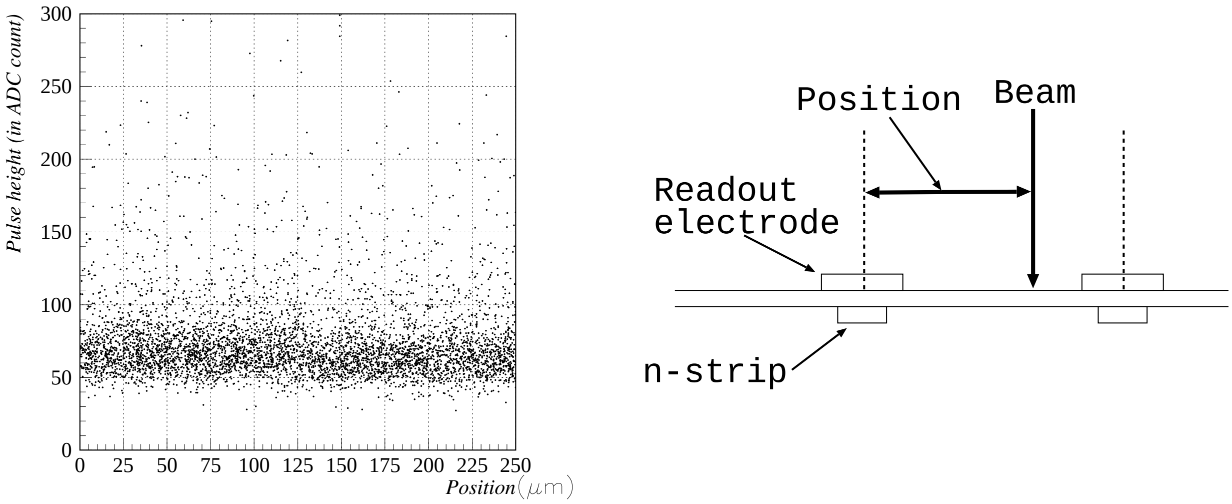

Figure 4.5: *The pulse-height distribution as a function of the position of incident particles with the type-C(250 μm) detector.*

4.4.2 Residual distribution

Figure 4.6 shows the residual distributions of the type-C (250μm) with the AC method. The difference between the point reconstructed by the reference telescope and the sample SSD is defined as residual. The charge generated by a penetrating particle is diffused. The size of the area is about 20μm[57]. When this diffused region is much narrower than strip pitch, the charge is collected by only one strip. In this case the penetrating position has no correlation with that reconstructed with AC method. The residual distribution forms a rectangle with width of the strip pitch. (Figure 4.6(a))

We defined sigma(σ_{fit}) by fitting each distribution with the Gaussian distribution[3]. Table 4.2-4.4 summarize the σ_{fit} obtained for all sample detectors. This σ_{fit} contains the contributions from multiple Coulomb scattering and the finite resolution of the reference SSDs. These contributions need to be subtracted from σ_{fit} to obtain the intrinsic resolution of the sample SSD. Multiple scattering effect is calculated with taking the geometry of the setup and the momentum of the π^- beam into account[66]. On the sample SSD, this effect is estimated to be 3.9$\pm$0.4μm for x-direction and 5.4$\pm$0.6μm for y-direction for particles with an incident angle of 0°. The resolution of each reference SSD has been measured by replacing the sample SSD

[3]The residual distribution does not form a Gaussian shape at zero incident angle. However, when we ignored the tail of distribution larger than strip pitch, the root mean square of residual was identical value of the width of fitted Gaussian function.

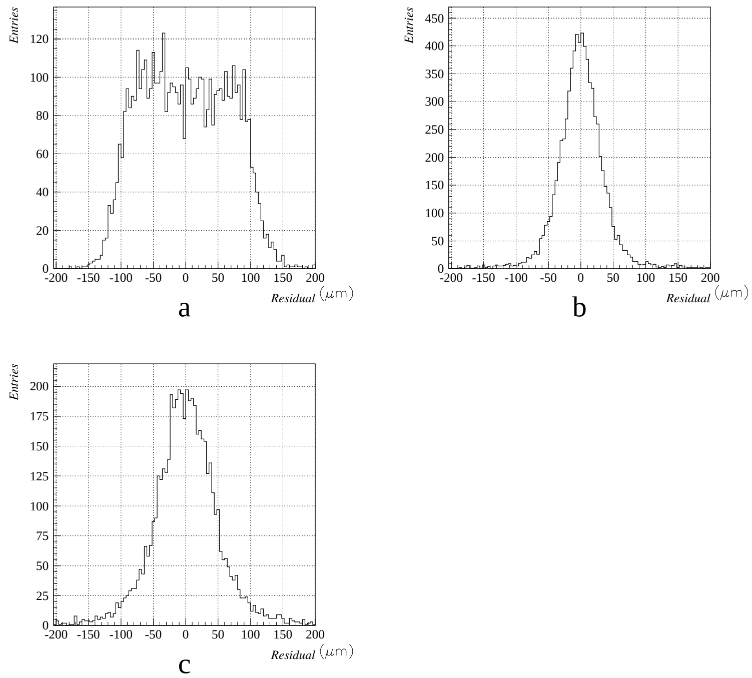

Figure 4.6: *Residual distribution with the type-C(250μm). (a) α=0°, (b) α=40° and (c) α=60°.*

with a reference SSD and we obtained 8.5$\pm$0.2μm. On the sample SSD, this corresponds to an uncertainty of 6.0$\pm$0.1μm.

4.4.3 Spatial resolution

The spatial resolution of the sample SSDs as a function of the incident angle is shown in Figure 4.7-4.9 and Table 4.2-4.4. We also show the simulation result for comparison. In our simulation, the signal and the noise are generated to reproduce the same S/N ratio as that in the measurement. The detail of simulation program is described elsewhere[62, 67]. The measured data and the simulation data are both analyzed with the same method. In the figure the open squares indicate data points with the AC method, the solid circles with the AHT method and the solid triangles with the ETA method, respectively. The solid lines are the simulation with the AC method. With the AC method, measurements agree well with the simulations.

The AHT method was applied for type-B and C with large incident angles. It is seen that there is no sizable improvement once the sparsification is adopted. The peak of the signal read out from a single strip is expressed as $S/N \times \frac{p}{D \times \sin\alpha}$, which becomes smaller with the larger incident angle (α) and the smaller strip pitch (p). When p is 50μm (type-A) and α is 75°, the expectation is 3.5 (with S/N of 20) which is below the threshold of the sparsification. Therefore we did not apply the AHT method for the type-A.

With the ETA method, the resolution is sensitive to the S/N ratio. We do not see a sizable improvement compared with the AC method in this test where the S/N ratios are around 20.

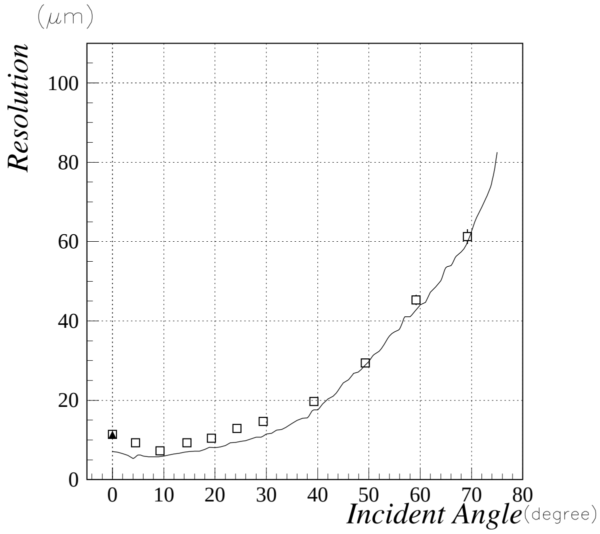

Figure 4.7: *Spatial resolution with type-A(50μm). The open squares indicate data points with the AC method, the solid circles with the AHT method and the solid triangles with the ETA method, respectively. The solid lines are the simulation with the AC method.*

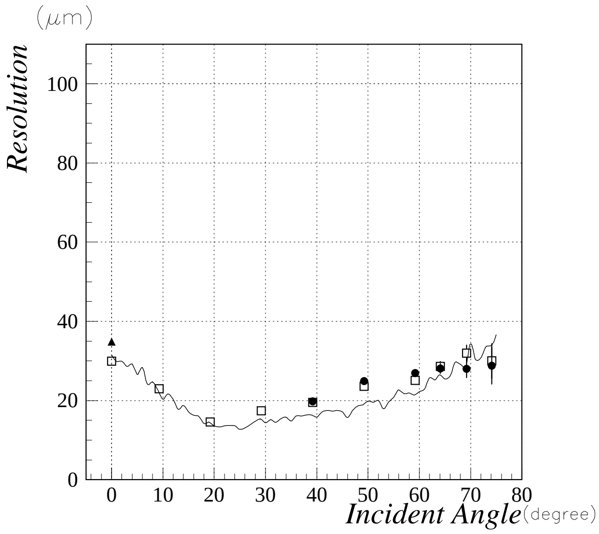

Figure 4.8: *Spatial resolution with type-B(125μm).*

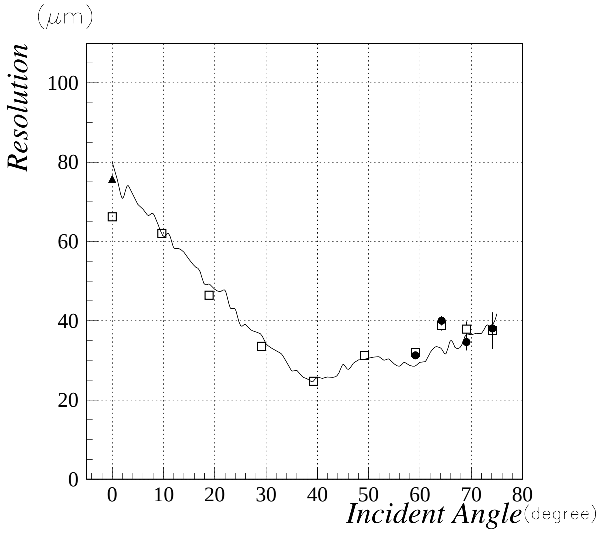

Figure 4.9: *Spatial resolution with type-C(250μm).*

Table 4.2: *Summary of the spatial resolution on the type-A with the AC method.*

Angle [deg.]	σ_{fit} [μm]	Spatial resolution [μm]	Angle [deg.]	σ_{fit} [μm]	Spatial resolution [μm]
0.0	16.3 ± 0.2	11.4 ± 0.3	29.4	20.4 ± 0.3	14.7 ± 0.4
4.5	15.0 ± 0.2	9.3 ± 0.4	39.3	25.8 ± 0.4	19.7 ± 0.5
9.3	13.9 ± 0.2	7.3 ± 0.5	49.3	36.2 ± 0.8	29.4 ± 1.1
14.5	15.3 ± 0.2	9.3 ± 0.4	59.1	54.3 ± 1.0	45.3 ± 1.2
19.3	16.4 ± 0.2	10.4 ± 0.4	69.2	79.6 ± 1.3	61.3 ± 1.9
24.3	18.5 ± 0.2	12.9 ± 0.4			

Table 4.3: *Summary of the spatial resolution on the type-B with the AC method.*

Angle [deg.]	σ_{fit} [μm]	Spatial resolution [μm]	Angle [deg.]	σ_{fit} [μm]	Spatial resolution [μm]
0.0	32.1 ± 0.2	29.9 ± 0.3	49.2	31.7 ± 0.4	23.6 ± 0.6
9.3	25.9 ± 0.2	23.0 ± 0.3	59.2	39.0 ± 0.5	25.1 ± 1.0
19.2	19.3 ± 0.2	14.6 ± 0.4	64.1	47.3 ± 0.6	28.6 ± 1.3
29.2	22.4 ± 0.3	17.4 ± 0.4	69.2	60.1 ± 0.8	32.0 ± 2.1
39.2	25.6 ± 0.3	19.5 ± 0.5	74.1	80.8 ± 1.0	30.0 ± 4.4

Table 4.4: *Summary of the spatial resolution on the type-C with the AC method.*

Angle [deg.]	σ_{fit} [μm]	Spatial resolution [μm]	Angle [deg.]	σ_{fit} [μm]	Spatial resolution [μm]
0.0	67.2 ± 0.7	66.2 ± 0.7	49.2	37.7 ± 0.5	31.3 ± 0.7
9.7	63.2 ± 0.6	62.1 ± 0.6	59.1	43.8 ± 0.6	32.0 ± 1.0
18.9	48.1 ± 0.4	46.4 ± 0.5	64.2	54.2 ± 0.7	38.8 ± 1.1
29.1	36.4 ± 0.3	33.6 ± 0.4	69.1	63.3 ± 0.8	37.9 ± 1.9
39.2	29.8 ± 0.3	24.7 ± 0.4	74.1	83.4 ± 1.7	37.5 ± 4.6

4.5 Performance of BELLE SVD

4.5.1 Selection of unit sensor

We determined the design of the unit silicon sensor with the test results of the small sample detectors. If we use one kind of silicon sensor for simplicity, a detector with the strip pitch around 100μm gives good resolution in all regions. Thus we selected S6936 SSD which has the pitch of 84μm for n^+-strip and is commercially available. The detail of parameters of S6936 SSD was already shown in the previous chapter(Table 3.3).

4.5.2 Test of the Detector Prototype of BELLE SVD

Detector prototype

We also tested the detector prototype which is the same as the detector module of final design of BELLE SVD[4]. The schematic view of the detector prototype is shown in Figure 4.10. The detector prototype consists of two S6936 SSDs. Two SSDs are connected with wire bonding. As mentioned in the previous chapter, the detector module of BELLE SVD is made with one or two sensors connected. In order to test both cases, a part of the detector prototype has the region where two SSDs are wire-bonded. We call this region "the double chained region". Other part where strips of two SSDs are not connected is named "the single region". The bias voltage was $80V$ on the n-side, while the p-side was grounded. The charge signal from the detector prototype was read out with a Viking chip[68].

The measurement was performed with the same setup as that for the small sample detectors. During the data taking period, we used a π^- beam with momentum of 3.5GeV/c. Data have been taken at the seven different incident angles ranging from $0°$ to $30°$.

Results

We obtained the S/N ratio of 17.7 ± 0.1 for n-side of the single region and 12.8 ± 0.1 for the n-side of the double chained region, respectively[5].

The spatial resolution of the n-side as a function of an incident angle ranging from $0°$ to $30°$, is shown in Figure 4.11 for the single region and 4.12 for the double chained region. These results are summarized in Table 4.5. Since the incident angle is smaller than $30°$, we calculated the hit position only with the AC method. In the figure the open squares indicate data points and the solid line the simulation. We can see a good agreement between the measurement and our simulation.

In our simulation, we neglected the gain variation of a preamplifier for each strip and a part of the capacitive charge coupling with double metal layer structure[69]. This effect is expected to be large with a small incident angle. The difference between simulation and measurement mainly comes from this effect.

[4]The difference is that two silicon sensors are connected without p-n flipped.

[5]The detector prototype consisted of two S6936 with both n-sides connected, which gave the worst S/N ratio. The result was, however, consistent with theoretical expectation. Since the real detector module uses p-n flipped connection, S/N ratio of the double region was much better and met our specification.

Table 4.5: Summary of the spatial resolution on the n-side of the detector prototype of BELLE SVD.

Single region			Double chained region		
Angle [deg.]	σ_{fit} [μm]	Spatial resolution [μm]	Angle [deg.]	σ_{fit} [μm]	Spatial resolution [μm]
0.0	21.7 ± 0.4	20.5 ± 0.5	0.0	21.3 ± 0.3	20.1 ± 0.4
5.0	18.6 ± 0.3	17.2 ± 0.4	5.0	20.2 ± 0.4	18.9 ± 0.5
10.0	16.1 ± 0.3	14.4 ± 0.4	10.0	14.9 ± 0.3	13.0 ± 0.4
15.4	10.6 ± 0.4	7.5 ± 0.4	15.5	13.5 ± 0.3	11.2 ± 0.4
20.2	14.1 ± 0.3	11.8 ± 0.4	17.2	14.5 ± 0.3	12.3 ± 0.4
25.2	15.7 ± 0.3	13.5 ± 0.4	23.2	17.3 ± 0.4	15.3 ± 0.5
29.3	15.0 ± 0.4	12.4 ± 0.5	28.8	17.8 ± 0.4	15.7 ± 0.5

4.6 Summary

We have measured the spatial resolution of the wide pitch SSDs and a prototype of BELLE SVD with large incident angles.

As expected by our simulation, the spatial resolution with wide strip pitch detectors didn't become worse very much and was better than that with narrow strip pitch detectors at the large incident angle. Our design of the silicon sensor of BELLE SVD (z-strip pitch of 84 μm) is proper choice to obtain good spatial resolution for particles with any possible incident angles required at BELLE SVD.

The spatial resolution shows good consistency with that expected by simulation with all prototype detectors. Our simulator well reproduces the behavior of intrinsic resolution of SSD. The simulator of BELLE detector described in the following chapters includes the SSD simulator used for comparison in this chapter. The results justify the correctness of SSD part of simulator which is the most crucial part in our physics simulation.

The overall performance for vertex reconstruction of BELLE SVD system is demonstrated in Chapter 6 with physics simulation.

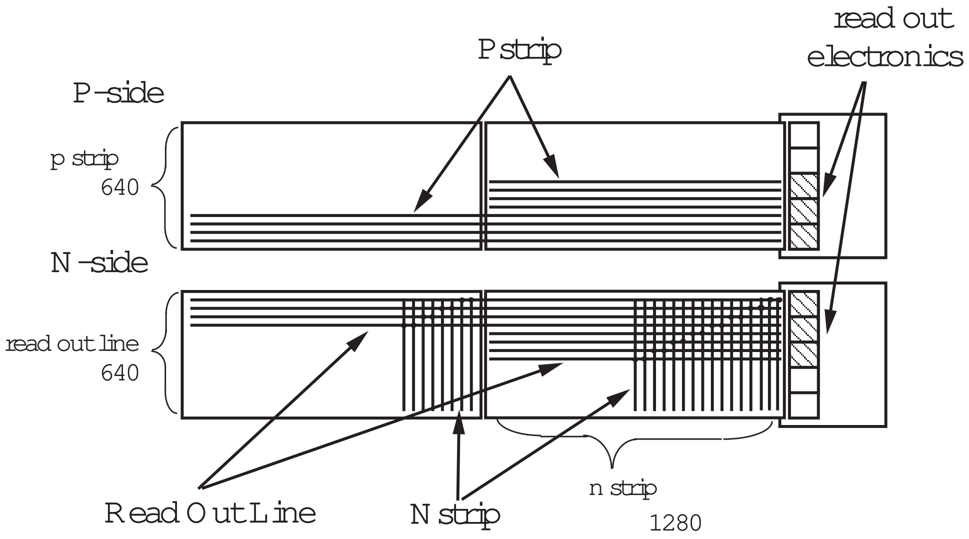

Figure 4.10: *The schematic view of the detector prototype of BELLE SVD.*

Figure 4.11: Resolution measured as a function of incident angle on the n-side of the single region of the detector prototype of BELLE SVD. The open squares with error bars are measured data. The solid line is our simulation.

Figure 4.12: *Resolution measured on the n-side of the double chained region of the detector prototype as a function of incident angle.*

Chapter 5

Monte Carlo Simulator for BELLE detector

This chapter presents an overview of the software tools used in the Monte Carlo simulation in this thesis. After BELLE experiment starts, this simulator will be used for various purposes, *e.g.* to estimate the detector response, efficiency and acceptance comparing with the experimental data.

In Section 5.1 a general framework of software and data flow for experimental and Monte Carlo(MC) data is described. Section 5.2 explains the event generation for Monte Carlo simulation. In section 5.3, the detailed description of detector simulation is given.

5.1 General Framework of Software

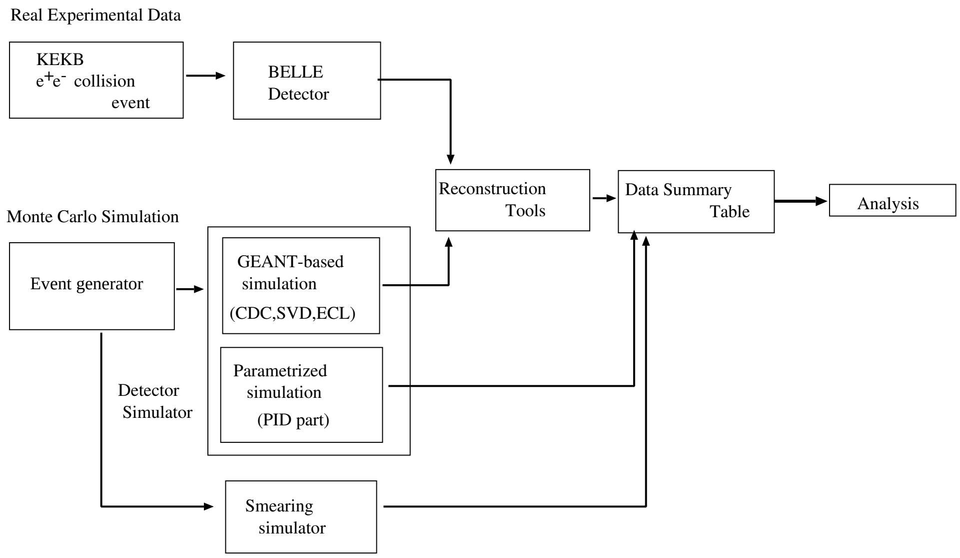

Figure 5.1: *General Framework of Software.*

The general framework of software and data flow for analysis is shown in Figure 5.1. All data transport, shown with arrows in Figure 5.1, are treated with the bank system called Panther[70], developed for BELLE. The MC events are produced by an event generator. The detector simulation is based on GEANT[71] to simulate charged particles in CDC and SVD, and photons in ECL. The signal from detector simulation has the same format as the experimental signal from the real detector.

The MC and experimental signals (digitized quantities such as time and charge) are translated to the physics quantities such as momentum and energy with reconstruction software. Other parts of the detector simulation, ACC, TOF and KLM, don't make the detector signal, i.e. these are not based on GEANT. These detector parts are used for particle identification and we used the parametrized simulator. Particle identification with CDC and ECL was also treated with the parametrized simulator. For the parametrization we used the results obtained in the test-beam experiments. In this thesis, unless otherwise noticed, MC means the event generated by GEANT and parametrized simulation for particle identification.

We also have a "smearing" simulator, which simulates all detector response by smearing the particle momentum vectors. Since it is about 500 times as fast as GEANT-based simulator, it was used to process the large amount of background events. The detail of the smearing simulator is described elsewhere[72].

All physics quantities, reconstructed and smeared for the particles were stored in Data Summary Table(DST). Analyses were performed using DST.

5.2 Event Generator

We used QQ[73] event generator developed by CLEO. It is designed to simulate the e^+e^- collision at the energy of Υ(4S). Event generation by QQ consists of two parts. In the first part reaction products which we call primary particles are generated at the interaction point. In the second particles decay according to the decay table and then daughter particles are generated. All interactions were calculated in the center of mass frame and were boosted to the lab frame according to the difference of e^+ and e^- beam energy.

5.2.1 Primary generation

The cross section for various physics processes are shown in Table 5.1 at the energy of $\Upsilon(4S)$ mass. Although Bhabha and 2γ processes have larger cross sections than $\Upsilon(4S)$ production, they are rejected in the selection effectively because of low track multiplicity or low total energy and transverse momentum. Therefore in this analysis we only considered $\Upsilon(4S)$ production and continuum events. The decay of $\Upsilon(4S)$ was taken care of in this part; it was assumed to decay either into $B^0\bar{B}^0$ or B^+B^- with the equal branching ratio[32].

The continuum, $e^+e^- \to q\bar{q}$, could be a serious backgrounds for $B^0\bar{B}^0$ signal. The continuum events were generated using JETSET[74, 75] inside QQ. For the hadronization process, LUND string model[76] was used for light quarks, u, d and s, and Peterson fragmentation model[77] was used for heavy quarks, c and b.

The spread of beam energy and the interaction point (IP) are also treated in this part. IP was distributed according to the size of beam bunch and the accuracy of beam orbit at the interaction region of BELLE detector. These parameters were determined with the design value of KEKB accelerator and the final-focus quardrupole magnet[49]. Assuming Gaussian shape, the widths of distribution were 110μm, 3μm, 6mm in x, y and z directions, respectively. The real beam bunch may have a wider tail which can not be parametrized with the ideal Gaussian function. Such non-Gaussian tail becomes an origin of beam background which is explained

Table 5.1: *Total cross section of e^+e^-collision at $\sqrt{s} = 10.58(GeV)$ for various processes.*

Physics Process	Cross Section(nb)
$\Upsilon(4S) \to BB$	1.15
Hadronic production from continuum	2.8
$\mu^+\mu^-+\tau^+\tau^-$	1.6
Bhabha	44
$\gamma\gamma$	2.4
2γ	~ 15

in Section 5.2.3. The energy of e^+e^- beam is also distributed. Center value of the energy of electron and positron were set to be 7.996 and 3.5GeV. Assuming a Gaussian shape, the beam energy smearing of electron and positron was modeled with widths of 5.4 and 2.5MeV.

5.2.2 Decays of particles

Generated particles decay to a specific mode with its branching ratios and lifetimes specified in the decay table taking its momentum into account. Long lived particles ($K^\pm$, $\pi^\pm$ and $\mu^\pm$) don't decay in the event generator. In order to consider the interaction with the detector material, decays of these particles are treated in the tracing part of detector simulation.

The branching ratios of B mesons to various exclusive mode were taken mainly from CLEO's data. Branching ratios of some of rare B^0 decays are assumed to be the same as that of corresponding $B^\pm$ decays based on isospin symmetry. In order to specify final states of a part of hadronic decays for which no experimental result is available, we used the decays to quark components and determined daughters and momentum distribution using fragmentation model in JETSET assuming the quark flavors of u, d, s and c.

We used the value of $\sin 2\phi_1 = 0.60$ to calculate CP asymmetry and mixing parameter $\Delta m/\Gamma_B = 0.71$ to reproduce $B^0\bar{B}^0$ mixing.

5.2.3 Beam background

Beam particles interact with residual gas molecules. Their paths deviate from those without interaction. Such particles are called spent electrons. The electrons(or positrons) which deviate from the original path may interact with the beam pipe or the detector. The background from such an origin is called "beam background" and can be a serious problem at the high luminosity collider machine such as KEKB.

To generate spent electrons we used DECAY TURTLE program[78]. First, it simulates the beam-profile with the parameters of KEKB. The interaction with a residual gas molecule was simulated with Coulomb scattering and Bremsstrahlung process. The off-orbit particles are transported with magnetic field along the beam line.

Generated spent-electrons are then mixed with each normal event. While the particles from beam collision are generated at a time, the beam background particles are not synchronous to collision timing. The beam background particles were generated with the time window of 15μsec before beam collision time in order to take this effect into account.

5.3 Detector Simulation

The generated particles are put into the detector simulator based on GEANT. In this section, particle tracing and detector response of SVD, CDC and ECL are described.

5.3.1 Particle tracing

The simulator takes into account detailed configuration of all the sub-detectors. Particle interaction in the detector material, decay in flight and the bending of the trajectory in the magnetic field are considered. The magnetic field is oriented to the electron beam direction (z-direction) and has the strength of 1.5 Tesla.

The short lived particles, which should decay inside the beam pipe, were forced to decay in the event generator. Although the decay of neutral particles, K_S and Λ, were also determined by the event generator, the decays of charged particles, kaon, pion and muon, were treated here according to the life time and branching ratios in order to take the interaction with material into account. For charged particles, energy loss is calculated in the materials by using Berger-Seltzer formula[79]. Although δ-rays were not generated, the effect of fluctuation by δ-ray generation was calculated according to Landau-Vavilov-Gauss function[80]. The effect of multiple scattering, bremsstrahlung, positron annihilation was calculated using standard formula. In addition, Monte Carlo simulation included the photon conversion at the material, compton scattering and photoelectric effect. To simulate the interaction of hadrons with the nuclei of the matter traversed, we used FLUKA[81], which is a GEANT library package.

The secondary particles generated by the above interactions were treated in a similar way. All particles propagate until they go out of the detector fiducial volume or their energy becomes lower than a threshold. The energy thresholds are 100keV for a photon and an electron, 1MeV for a muon and a charged hadron, 10MeV for a neutral hadron.

5.3.2 Central Drift Chamber(CDC) response simulation

Central Drift Chamber(CDC) was divided into many small cells, each of which has one sense wire at the center. When charged particles pass a cell, the deposited energy was calculated from its momentum with Bethe-Bloch formula. The charge was generated from the deposited energy and was then collected by sense wires. The drift time from the particle path to the sense wire was then smeared with position resolution. The deposited energy and the drift time with their smearing are then converted to digital data. If multi hits were recorded in the same cell, the earliest hit-timing and sum of charge were kept. After all these processes, we obtained hit wire numbers, TDC and ADC counts.

5.3.3 Silicon Vertex Detector(SVD) response simulation

The response of SVD is based on the testbeam result described in Chapter 4. When a charged particle penetrates Silicon Vertex Detector(SVD), it creates electron-hole pairs along its path in the depletion area of the semiconductor. The fluctuation due to δ-ray is taken into account. The charge carriers are then moved, diffused and collected to the nearest strip and smeared with electric noise. The charge was distributed among neighboring strips taking into account the charge coupling between the strips. Then the charge was converted with an amplifier to voltage signal with an appropriate time constant and was translated to ADC count and stored. After these processes, we obtained the hit strip numbers and ADC count for each strip.

5.3.4 ECL response simulation

As mentioned in the particle tracing part, GEANT simulates the electromagnetic shower of a charged particle in the detector material. Each particle entering CsI(*Tl*) crystal of Electromagnetic Calorimeter (ECL) deposits energy which depends on its velocity and the charge. ECL routines collect the energy deposited in each CsI(*Tl*) crystal.

The measured energy is smeared with two kinds of noise. One is incoherent, which is independent in each crystal. The other is coherent noise, which is correlated and the energy in all crystals are shifted simultaneously. The magnitudes of these noise are optimized with data taken from the prototype test and design performance of readout electronics. Considering the light yield to be proportional to the the sum of deposit energy, we correct measured energy with calibration constant[1] and translate it to ADC count.

5.3.5 Simulation of detector response for particle identification

The simulator of each Particle Identification (PID) device provides a probability for a certain particle hypothesis when a particle enters within its acceptance. In the following, the calculation methods of the probability are described.

Central Drift Chamber(CDC)

CDC is able to test particle hypothesis by checking the difference between the expected and measured energy loss. The expected dE/dx for each particle hypothesis is calculated from particle's measured momentum. The measured dE/dx is given from the generated but smeared velocity according to the dE/dx resolution.

The probability of a track being a particular particle type i (=e, μ, π, K, p) is calculated as:

$$prob_i = \frac{1}{\sqrt{2\pi}\sigma_x^i} \exp\left\{ -\frac{1}{2}\left(\frac{x_{mea} - x_{exp}^i}{\sigma_x^i}\right)^2 \right\},$$

where x_{mea} is measured(simulated) dE/dx, x_{exp} expected one for the particle type i and σ_x^i resolution of measured dE/dx. For example, the π/K separation capability with dE/dx of CDC is shown in Figure 5.2.

Time of Flight Counter(TOF)

The main role of TOF is to distinguish $K^\pm$ from $\pi^\pm$ at lower momentum than 1.2GeV/c. Taking the TOF's acceptance ($33^\circ < \theta < 124^\circ$ in polar angle) and efficiency(=90%) into account, the simulator calculates the time-of-flight smeared with the time resolution of TOF counters(=100pS). The expected time-of-flight is calculated with the β of particle which is calculated with momentum and the mass of the particle in assumption. The probability of a track being a particular particle type is calculated in the same way as CDC. The π/K separation capability with TOF system is shown in Figure 5.2.

[1] At the real experimental situation, the calibration constant will be determined using π^0 mass reconstructed from 2γ.

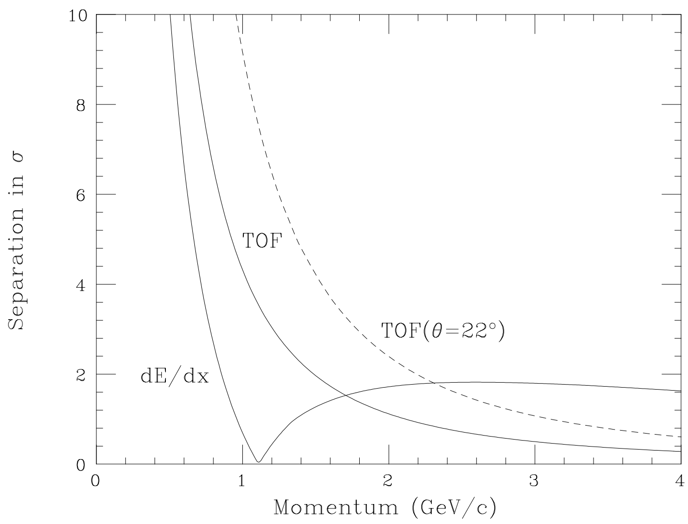

Figure 5.2: *The π/K separation capabilities expected for the dE/dx and TOF systems, expressed in units of rms separation. These are for $\theta = 90°$ tracks unless otherwise specified.*

Aerogel Čherenkov Counter(ACC)

The ACC's acceptance is $17° < \theta < 34°$ for forward endcap region and $34° < \theta < 127°$ for barrel region. The detection efficiency is defined as Figure 5.3. These values are based on data from test-beam experiments [53]. The probability of a track being a particular particle type is calculated as:

$$prob^i = \epsilon^i_{exp} \quad \text{(detected)},$$
$$prob^i = (1 - \epsilon^i_{exp}) \quad \text{(no detected)}.$$

Here, ϵ^i_{exp} is an expected detection efficiency for ith particle hypothesis.

Cesium Iodide Calorimeter(ECL)

The performance of ECL is taken from test data and GEANT simulation [82]. The electron identification efficiency is defined as

$$\begin{aligned} eff &= 0.0(E_e < 0.5GeV), \\ &= 0.90(0.5 < E_e < 1.0GeV), \\ &= 0.95(E_e \geq 1.0GeV), \end{aligned}$$

for the region $13° < \theta < 153°$. The probability of misidentifying a hadron as an electron(eff_{mis}) is assumed to be 4.5(1.0)% at 0.5GeV/c and 0.2(0.3) at 3.0GeV/c for a positive(negative) particle. For the given energy of particle, eff_{mis} is interpolated from these values and calculated.

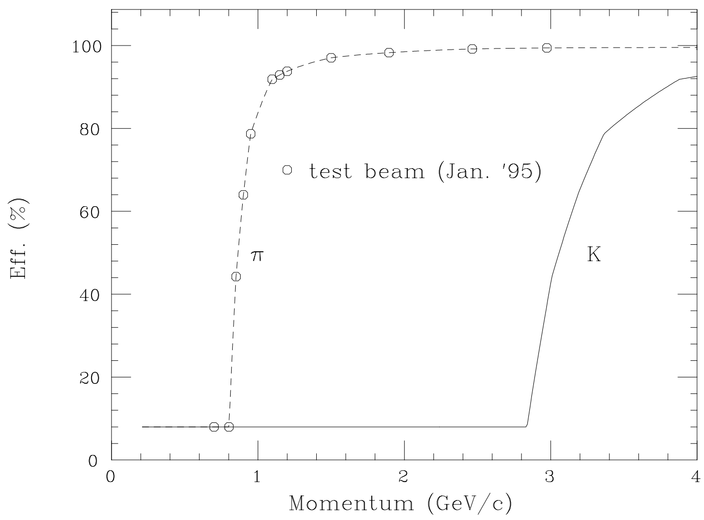

Figure 5.3: *The efficiency of the ACC as a function of momentum. The open circles are measurements under a magnetic field of 1.3T.*

The probability of a track being a particular particle is calculated in the same way as the ACC case with eff for electron and eff_{mis} for hadrons.

K_L and Muon Detector(KLM)

KLM is used to identify high momentum muons. KLM's efficiency is assumed to be

$$\begin{aligned} eff &= 0.0(E_\mu < 1.2GeV), \\ &= 0.9(E_\mu \geq 1.2GeV), \end{aligned}$$

for the region $30° < \theta < 140°$. The hadron misidentification probability is defined to be 1% which was derived with GEANT-based simulation[83]. The probability of a track being a particular particle is calculated in the same way as the ACC case with eff for muon.

5.3.6 Trigger simulation

Trigger efficiencies for various decay modes were checked with simulation. The results show that we obtain $\sim 100\%$ efficiency for the decay modes of B mesons we are interested in[84]. Therefore in this analysis, we have assumed that trigger efficiency is 100% and the trigger simulation is not included. Since we don't need to know the absolute trigger efficiency to measure the CP asymmetry, we simply assume the effective integrated luminosity throughout the analysis.

Chapter 6

Simulation for Vertex Resolution

In this chapter, we explain a simulation performed to estimate the vertex resolution of BELLE SVD for B meson decays.

We studied the vertex resolution for $B \to J/\psi K_S$, which is one of the best modes to observe CP asymmetry in BELLE. In the study, we generated $\Upsilon(4S) \to B^0 \bar{B}^0$ in which one B decays into $J/\psi K_S$ (called B_{CP} hereafter) and the other decays generically (called B_{tag} hereafter), with Monte Carlo simulation. We set J/ψ decays into two leptons ($\mu^+\mu^-$ or e^+e^-) and K_S decays into $\pi^+\pi^-$.

In Section 6.1, the track reconstruction of charged particles is described. In Section 6.2, we explain the method to reconstruct the decay vertices of the two neutral B mesons from the decay of $\Upsilon(4S)$ and estimate the resolution of vertex position. We summarize this chapter in Section 6.3.

6.1 Track Reconstruction

6.1.1 Track reconstruction in CDC

The trajectory of a charged particle is helical in the magnetic field. Reconstructed tracks are expressed with five helix parameters(dr, ϕ, ρ, dz, θ). The definition of these parameters are shown in Figure 6.1. The 3-dimensional track reconstruction in CDC is performed in the following order[1].

1. Using hits of the axial wires (see Section 3.2.2), each track in r-ϕ plane is reconstructed assuming it is a circle. In order to find track candidates, "the conformal and histogram method" was used[85].

2. Using hits of the stereo wires, a track is reconstructed assuming a straight line in z-$S_{r\phi}$ plane, where $S_{r\phi}$ is the length of arc along the track in r-ϕ plane.

3. The track was fitted using hits of the axial and the stereo wires with a helix trajectory in 3 dimension.

All helix parameters are determined with this fitting .

Figure 6.2 shows the tracking efficiency as a function of a momentum for (a) single π^+ events and (b) $B \to J/\psi K_S$ events, where J/ψ was set to decay into l^+l^-, K_S into $\pi^+\pi^-$ and other B

[1]The details of the track finding are described in Appendix B.

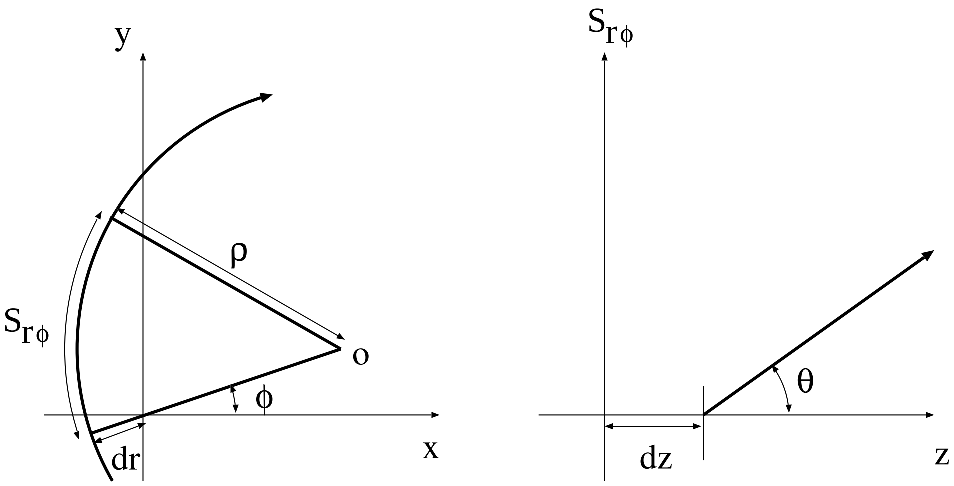

Figure 6.1: *Helix parameters. The charged tracks are expressed with five helix parameters, dr, ϕ, ρ, dz and θ. In the figure $S_{r\phi}$ is the arc length.*

generically. The figures do not include an acceptance effect. For single π^+ events, we obtained the efficiency of 95% or more for the momentum higher than 200MeV/c. For $B \to J/\psi K_S$, the efficiency was degraded by the presence of other particles. However, it is high enough for momentum above 300 MeV/c.

6.1.2 Track fitting with CDC and SVD hits

SVD has much better resolution in z direction than that of CDC. Using SVD hits and extrapolation of tracks reconstructed in CDC, tracks are refitted to reconstruct vertices with high accuracy.

In track reconstruction in CDC described above, the effects of the multiple scattering (MS) and energy loss (LOSS) in the detector were ignored. Taking these effects into account, we refit each track with all hits in both CDC and SVD.

The refitting was performed with a Kalman filter method[86, 87, 88]. Because of the effects of MS and LOSS in the detector, the trajectory of particle is not an ideal helix. In the Kalman filter method, helix parameters are not global and are defined at each hit point of CDC and SVD. Hits are traced from the outermost wire in CDC to beam axis along a track trajectory. Taking MS and LOSS[2] into account, we correct the helix with the expected trajectory and each measured hit point. Hits with poor quality were also rejected in this refitting in CDC.

In the fitting in SVD, since this refitting was performed in 3-dimension, we required that hit strips were found on both sides on each silicon sensor.

When there are associated hits on at least 2 layers, the track is defined as "a track with matched SVD hits". Then helix parameters are re-calculated at the interaction point.

Figure 6.3 shows the SVD matching efficiency. We obtained the matching efficiency of 98% with the momentum higher than 500MeV/c.

[2]We assume the particle has a pion mass.

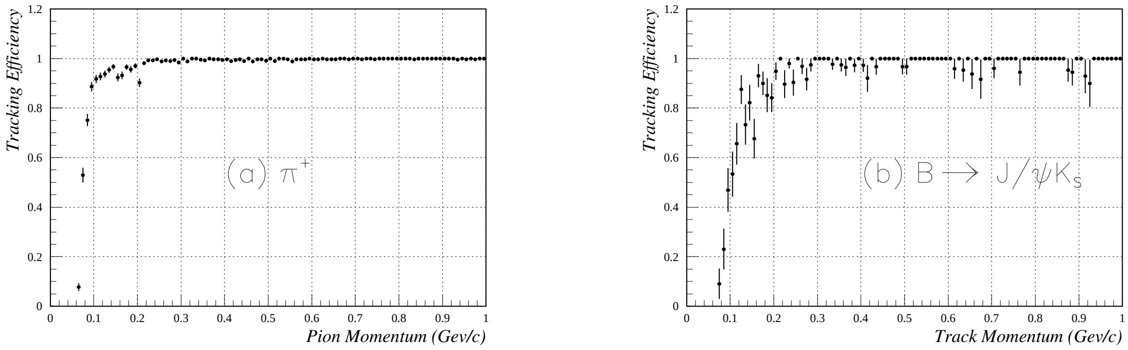

Figure 6.2: *Tracking efficiency as a function of the momentum for (a) single π^+ event and (b) $B \to J/\psi K_S$ event.*

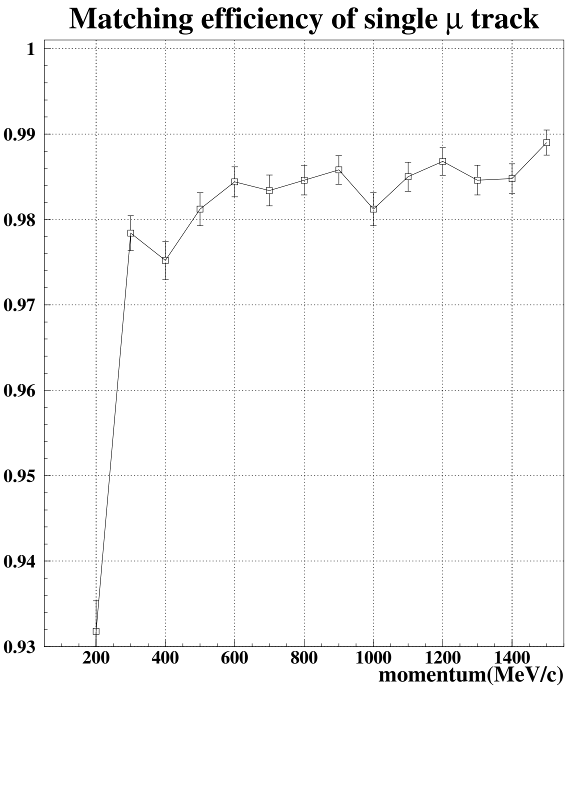

Figure 6.3: *SVD matching efficiency for single muon events. Muons were generated in SVD acceptance.*

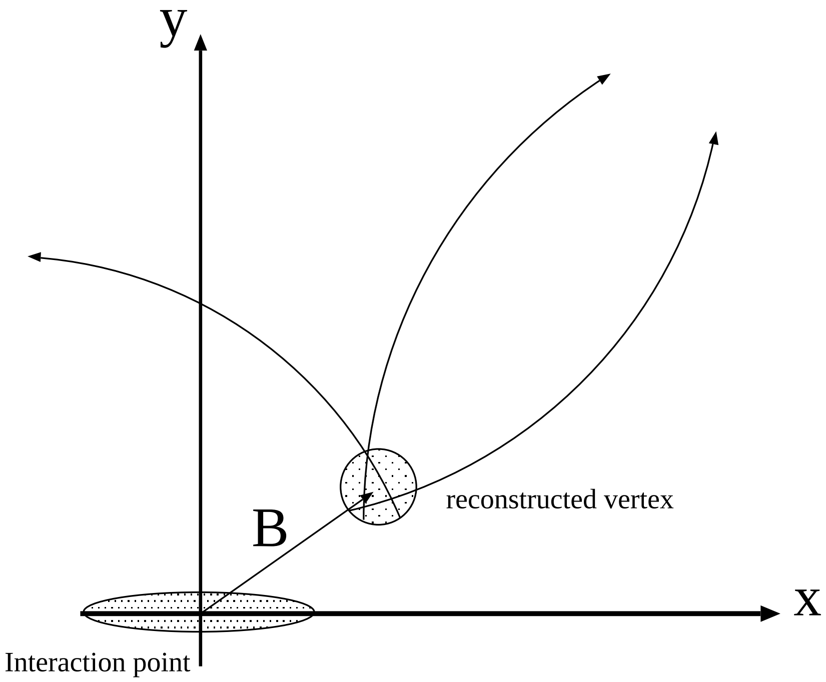

Figure 6.4: *Vertex reconstruction.*

6.2 Estimation of Vertex Resolution

6.2.1 Overview of vertex reconstruction

Vertex reconstruction is a process of finding the best estimate of the three dimensional point of intersection of tracks(See Figure 6.4). Assuming that the magnetic field is uniform and the effect of detector material is small, the trajectory of a charged particle can be approximated by a helix. Most of vertex reconstruction algorithms work by minimizing the sum of the squares of the distance of closest approach of a set of tracks to a candidate point. The χ^2 of vertex is calculated as[85]

$$\chi^2 = \sum_{i=1}^{n} (h_i - h(v, p_i))^T C_i^{-1} (h_i - h(v, p_i)) \tag{6.1}$$

where n is the number of tracks, i runs over all the tracks, C_i is a covariance matrix of helix parameters, which gives the errors of parameters and their correlation to each other, h_i is the matrix of five helix parameters of i-th track, $h(v, p_i)$ is the matrix of five helix parameters which passes the vertex, v, and have the momentum, p_i. The reduced $\chi^2(=\chi^2/n.d.f.)$ indicates goodness of vertex reconstruction, where n.d.f. is the number of degrees of freedom defined as $2 \times N_{track} - 3$, where N_{track} is the number of the tracks used to reconstruct a vertex.

6.2.2 Vertex reconstruction of B_{CP}

We used the decay vertex of J/ψ as the decay vertex of B_{CP} (called V_{CP} hereafter). The vertex of J/ψ was reconstructed with using two daughter leptons.

In order to maximize the reconstruction efficiency of the V_{CP}, we took the following procedure:

- If both tracks have matched SVD hits, V_{CP} was reconstructed with two leptons in 3-dimension.
- If only one track has a matched SVD hits, we reconstructed the vertex position with one lepton track and the beam axis.

If both tracks do not have matched SVD hits, we did not use the event. By adding the second criterion, the efficiency become better by 7.8%. The size of the beam constraint is determined with the size of beam bunch and the decay length of B meson. The beam size is 100μm in x and 3μm in y at the interaction point. The decay length of B meson in $x-y$ plane is about 30μm[3]. We have assumed the size of beam constraint to be 100μm in x and 30μm in y.

In order to reject vertices erroneously reconstructed in random combination, we required a candidate to have smaller reduced χ^2_{vtx} of fitting than a threshold (=10.0), The distribution of the reduced χ^2_{vtx} and the residual distribution in z-direction between the reconstructed V_{CP} and the generated V_{CP} are shown in Figure 6.5 for $B \to J/\psi K_S$ MC. In the residual distribution, there is a tail due to electrons which have lost large energy by radiation. When we have fitted the residual distribution with double Gaussian function, σ's were 44.3 μm and 211.4 μm for narrower and wider components, respectively. The fraction of narrower component was 89%. We get the vertex reconstruction efficiency of 94.1% for $B \to J/\psi K_S$. The vertex resolution obtained is summarized in Table 6.1.

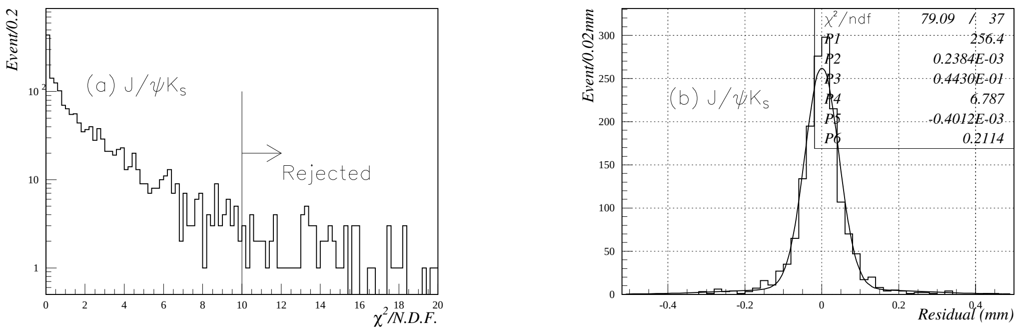

Figure 6.5: *Reconstruction of vertex of B meson in CP side for $B \to J/\psi K_S$ MC. (a) The distribution of reduced χ^2 of V_{CP} reconstruction. (b) The residual distribution of V_{CP} in z direction.*

6.2.3 Vertex reconstruction of B_{tag}

The reconstruction of the decay vertex of B_{tag} (called V_{tag} hereafter) is more complicated than that of V_{CP}. We didn't restrict decay modes and didn't reconstruct B explicitly. We first excluded tracks belonging to B_{CP}. We also rejected tracks with dr[4]larger than 1mm. Since $\Upsilon(4S)$ is produced at rest in r-ϕ plane, we expect the V_{tag} in r-ϕ plane from V_{CP} assuming two

[3](decay length in z)$\times p_t/p_z$=200μm$\times$0.34(GeV/c)/2.25(GeV/c).
[4]dr is an impact parameter in r-ϕ plane. The definition of dr refer to Figure 6.1.

B^0's have the opposite momentum and have same decay length from mean life time of B meson. Then a V_{tag} is reconstructed using all remaining tracks and a constraint axis, which is parallel to beam axis and whose position in r-ϕ, $\vec{r}_{const}$, was determined with the following equation:

$$\vec{r}_{const} = \vec{r}_{V_{CP}} - 2\frac{\vec{p_t}}{m_B}c\tau_B, \tag{6.2}$$

where $\vec{r}_{V_{CP}}$ is a position of V_{CP} in r-ϕ and p_t the transverse momentum of B_{CP}. If the reduced χ^2_{vtx} of fitting was larger than the threshold(=10.0), we rejected the track which had the largest χ^2_{track}. Here χ^2_{track} is χ^2 of each track for the reconstructed vertex. We repeated this procedure until we get a vertex which had the reduced χ^2_{vtx} smaller than the threshold. In case there was no track remained, it means that the vertex finding was failed.

In Figure 6.7, we show the residual distributions of V_{tag} in z-direction and Δz, which is the difference between the two B^0 decay vertices. Both distributions have tails to the positive direction due to the effect of secondary tracks from charm decays. The average number of tracks remained was 3.5 (See Figure 6.8). The average number of iteration of fit was 1.1 (See Figure 6.9). The reconstruction efficiency of V_{tag} was 99% for $B \to J/\psi K_S$.

The residual distributions of V_{tag} and Δz vertices were fitted with double Gaussian function. The vertex resolution obtained is summarized in Table 6.1. The σ of the narrower component is less than 100 μm. The narrower component is dominant and has a fraction of 0.82.

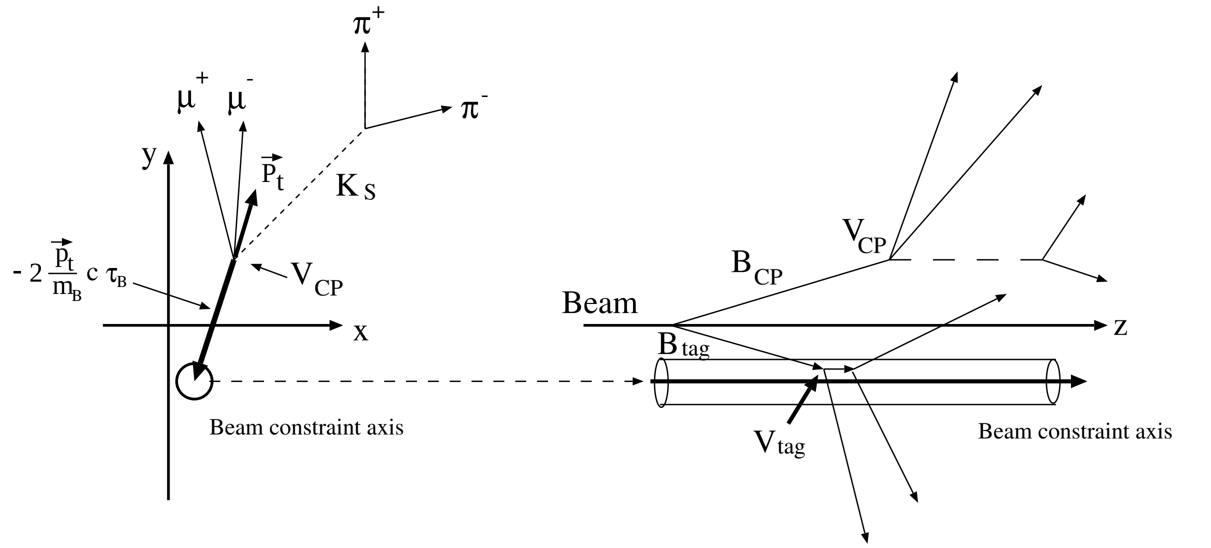

Figure 6.6: *The reconstruction of Tag-vertex. "Beam constraint axis" was calculated with V_{CP} and momentum of B candidate.*

6.2.4 Evaluation of vertex resolution

The sensitivity of measurement of $\sin 2\phi_1$ is calculated analytically as[89]

$$\delta(\sin 2\phi_1) \simeq \frac{1}{d\sqrt{N}}, \tag{6.3}$$

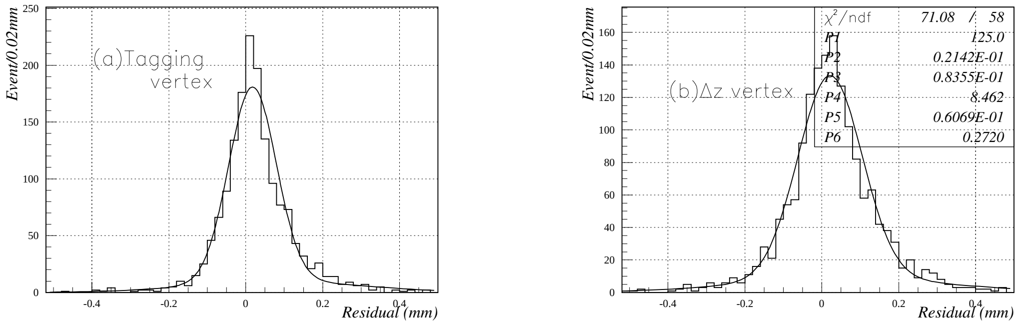

Figure 6.7: *The residual distribution of V_{tag} in z-direction and Δz for $B \to J/\psi K_S$ MC. The residual distribution of Δz is fitted with double Gaussian function.*

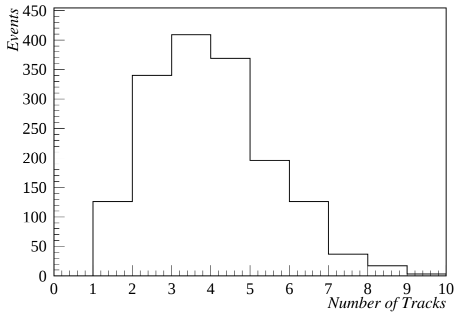

Figure 6.8: *The distribution of the number of the track associate to tagging vertex in $B \to J/\psi K_S$ MC.*

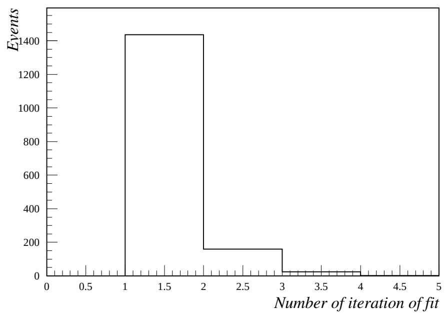

Figure 6.9: *The distribution of the number of the iteration of tagging vertex fit in $B \to J/\psi K_S$ MC.*

Table 6.1: *Results of vertex fitting for $B \to J/\psi K_S$ MC. The fraction of narrow component is f_n. The mean and width are m_n (m_w) and σ_n (σ_w) for narrow (wide) component, respectively. The units for mean and width are μm.*

Mode	Parameters[μm]				
	f_n	m_n	σ_n	m_w	σ_w
V_{CP}	0.89	0.24	44.3	-0.40	211.4
V_{tag}	0.83	17.4	61.8	85.8	222.6
Δz	0.82	21.4	83.6	60.7	272.0

where N is the number of observed events and d is the dilution factor due to the effect from the finite resolution of vertex reconstruction[5]. As mentioned in Section 2.2.3, the proper time distribution of B decays is

$$f(\tau) = \frac{1}{2}e^{-|\tau|}(1 \pm \sin 2\phi_1 \sin x_d \tau), \tag{6.4}$$
$$\tau = \Delta t/\tau_B, \quad c\gamma\beta\Delta t = z_{tag} - z_{CP} = \Delta z.$$

where $\tau \equiv \Delta t/\tau_B$ is the normalized time difference of the two B meson decays, z_{tag} (z_{CP}) is z position of decay vertex of B_{tag} (B_{CP}), τ_B is B^0 meson lifetime and x_d is $B^0\bar{B}^0$ mixing parameter ($= \Delta m/\Gamma_B$). The plus (minus) sign in front of $\sin 2\phi_1$ corresponds to the events tagged by $\bar{B}^0(B^0)$ decay. With real experimental situation, an asymmetry is smeared and (6.4) is modified to

$$F(\tau) = \int_{-\infty}^{\infty} d\tau' g(\tau, \tau') f(\tau'), \tag{6.5}$$

where g is the response function of vertex reconstruction. The dilution factor d is calculated as[90][6]

$$d^2 = \int_{-\infty}^{\infty} \frac{1}{F}\left(\frac{\partial F}{\partial(\sin 2\phi_1)}\right)^2 d\tau. \tag{6.6}$$

As described in Section 3.3, we required the vertex resolution to be about 100μm. When we assume the response function as a Gaussian function with $\sigma = 100\mu m$, we obtain d of 0.587[7].

[5] This is valid only when the background can be ignored, such as the case for $B \to J/\psi K_S$.

[6] When we extract the value of $\sin 2\phi_1$ from the distribution of proper time of B decays, we use maximum likelihood method! Jsee Section 8.2). In this method, we serach $\sin 2\phi_1$ which give the miximum value of logarithm of likelihood function, $\ln \mathcal{L}$. The error for $\sin 2\phi_1$ is given as

$$\sigma^2(S) = E\left(-\frac{\partial^2 \ln \mathcal{L}}{\partial S^2}\right)^{-1}$$

where S =$\sin 2\phi_1$. With N events of measured sample and $\mathcal{L}$ given as F in (6.5), we obtain

$$= \left\{\int_{-\infty}^{\infty} \sum_{i=1}^{N} \left(\frac{\partial^2 \ln F}{\partial S^2}\right) F d\tau\right\}^{-1} = \left\{N \int_{-\infty}^{\infty} \left(\frac{\partial^2 \ln F}{\partial S^2}\right) F d\tau\right\}^{-1}$$
$$\sigma^2(S) = \left\{N \int_{-\infty}^{\infty} \frac{1}{F}\left(\frac{\partial F}{\partial S}\right)^2 d\tau\right\}^{-1}.$$

[7] The dilution factor depends on the value of $\sin 2\phi_1$. We assume $\sin 2\phi_1$ to be 0.60.

Using a double Gaussian function obtained above, d was estimated to be 0.546. Since the sensitivity is proportional to $1/\sqrt{N}$, the number of events needed to measure $\sin 2\phi_1$ with the same accuracy increases by 16% from the case with a single Gaussian with $\sigma = 100\mu$m.

6.3 Summary

In order to evaluate the vertex resolution of B decays with BELLE SVD, we performed simulation study for $B \to J/\psi K_S$. Using double Gaussian resolution function, we obtained the vertex resolution of Δz of 83.6μm for a narrower component with a fraction of 0.82, which is much smaller than the decay length of B meson in z($\sim$200μm). Taking the effect of the wider component into account, the dilution factor in $\sin 2\phi_1$ measurement turns out to be compatible with the case of a single Gaussian response function with σ=100μm.

Thus we conclude that BELLE SVD has the vertex resolution which is good enough to measure CP asymmetry.

Chapter 7

Physics Simulation

In this chapter, we will present the event generation, reconstruction and selection in our physics simulation for the decay mode $B^0 \to$ charmonium + K_S described in Section 2.4. We treat the events generated by Monte Carlo simulation as real data and make the event sample to study CP violation.

First, we will explain the outline of physics simulation in Section 7.1. The event generation of Monte Carlo data (MC-data) are described in Section 7.2. The event selection criteria are described for $B \to J/\psi K_S$ in Section 7.3 and for other modes, $B \to \psi(2S)K_S$, $B \to \chi_{c1}K_S$ and $B \to \eta_c K_S$, in Section 7.4. The number of background is estimated in Section 7.5. In Section 7.6, we summarize the result of this chapter.

7.1 Outline of Physics Simulation

We perform physics simulation in the following steps;

1. Event generation
2. Reconstruction of candidate B mesons.
    1 K_S candidate reconstruction.
    2 Charmonium candidate reconstruction.
    3 B meson candidate reconstruction with charmonium and K_S candidate.
3. Flavor tagging.
4. Vertex reconstruction of the B meson at CP and tagging side.

In the following sections, we describe each step.

7.2 MC-data Generation

In this study, we treat the events generated by Monte Calro simulation as real experimental data. We call that "MC-data" and distinguish them from usual Monte Calro simulation. MC-data include both signal and background events at the integrated luminosity of 100fb^{-1}. This integrated luminosity will be obtained in one year with the design luminosity of KEKB. We didn't use generator information but only reconstructed values.

MC-data event sample was generated with the GEANT-based simulator(hereafter GSIM) and the smearing simulator (hereafter FSIM). Backgrounds from continuum and B^+B^- don't have CP asymmetry (called uncorrelated backgrounds). Since the effect to the measurement of $\sin 2\phi_1$ due to the difference between FSIM and GSIM was small, uncorrelated background were generated with FSIM*

On the other hand, decay products from $B^0\bar{B}^0$ can have CP asymmetry and thus can not be ignored. All signal events and $B^0\bar{B}^0$ background events of MC-data for $B \to J/\psi K_S$, $B \to \psi(2S)K_S$ and $B \to \chi_{c1}K_S$ were therefore generated with GSIM. In order to reduce the number of events, only specific event types were generated. The decay modes and branching ratios used in the event generation are summarized in Table 7.1. Since $B \to \psi(2S)K_S$ and $B \to \chi_{c1}K_S$ have not been established yet, we took the same branching ratios as charged B mesons decays assuming isospin symmetry[46]. In these restricted decay modes, we have set that K_S decays to $\pi^+\pi^-$, K^* to $K_S\pi^0$ or $K^\pm\pi^\mp$, J/ψ to $\mu^+\mu^-$ or e^+e^-, χ_{c1} and χ_{c2} to $\gamma J/\psi$. $\psi(2S)$ was set to decay to $\mu^+\mu^-$, e^+e^-, $J/\psi\pi^+\pi^-$, $\gamma\chi_{c1}$, $\gamma\chi_{c2}$ or $\eta J/\psi$. $B^0\bar{B}^0$ background events for $B \to \eta_c K_S$ were generated with FSIM since they are almost uncorrelated†.

Table 7.1: *Decay modes and its Branching ratios of B^0 for MC-data generation.*

Decay mode	Branching ratio	Decay mode	Branching ratio
$J/\psi K_S$	4.5×10^{-4}	$\psi(2S)K_S$	3.5×10^{-4}
$J/\psi K_S\pi^+\pi^-$	3.5×10^{-4}	$\psi(2S)K^*$	1.4×10^{-3}
$J/\psi K_S\pi^0\pi^0$	3.5×10^{-4}	$\chi_{c1}K_S$	5.0×10^{-4}
$J/\psi K_S\pi^0$	3.5×10^{-4}	$\chi_{c2}K_S$	3.5×10^{-4}
$J/\psi K^*$	1.35×10^{-3}	$\eta_c K_S$	9.9×10^{-4}

7.3 Event Selection for $B \to J/\psi K_S$

In this section, we describe the event selection for $B \to J/\psi K_S$.

7.3.1 Reconstruction of K_S candidate.

K_S decays into two neutral or charged pions with branching fractions shown in Table 7.2. We used only charged mode to reduce the combinatorial background. Since K_S has long decay length‡ compared to B^0's, we can obtain clean signals by rejecting candidates which have short decay length. The distance between the decay vertex of the K_S and the decay vertex of B_{CP} was required to be larger than 2.0mm. We lose few signal events with this cut.

We defined the decay vertex of K_S§ as the crossing point of two tracks where the $z-$distance between two helixes was smaller (c1 in Figure 7.1). The z position of decay vertex of K_S is defined as the middle point of two helixes at the cross point in $r - \phi$ plane.

*Only GSIM takes the effect of CP asymmetry into account.

†The number of remaining backgrounds and their species are also estimated with independent Monte Carlo events using generator information. The analysis and result are described in Appendix D.4.

‡~20cm in r-ϕ plane at BELLE.

§Reconstruction of the vertex of B_{CP} is described in Section 7.3.5.

Table 7.2: K_S *branching ratios.*

Decay mode	BR	Used
$K_S \to \pi^+\pi^-$	$(68.61 \pm 0.28)\%$	$\circ$
$\pi^0\pi^0$	$(31.39 \pm 0.28)\%$	$-$

Invariant mass was calculated assigning the nominal pion mass ($M_\pi = 139.6MeV/c^2$) to both tracks.

$$M^2_{\pi^+\pi^-} = \left(\sqrt{M_\pi^2 + |\vec{P}_{\pi^+}|^2} + \sqrt{M_\pi^2 + |\vec{P}_{\pi^-}|^2}\right)^2 - |\vec{P}_{\pi^+} + \vec{P}_{\pi^-}|^2,$$

where $\vec{P}_{\pi_{1,2}}$ was calculated at the decay vertex of K_S. We require that the invariant mass be

$$|M_{K_S} - M_{\pi^+\pi^-}| < 0.015GeV/c^2,$$

where M_{K_S} is the nominal K_S mass ($M_{K_S} = 497.7MeV/c^2$). Invariant mass distribution of K_S for $B \to J/\psi K_S$ is shown in Figure 7.2.

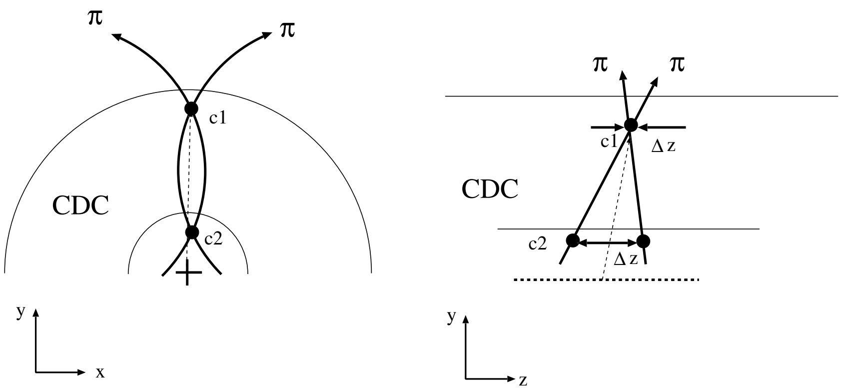

Figure 7.1: *Reconstruction of* K_S *vertex.*

7.3.2 Reconstruction of J/ψ candidate

We reconstructed J/ψ through its decays into $\mu^+\mu^-$and e^+e^-(branching ratios shown in Table 7.3). Although the most straight forward way is to use 2 charged tracks with opposite charges both tagged as μ or e, we required "at least" one lepton in order to have higher reconstruction efficiency. We identify μ with KLM and e with the combined information from CDC, ACC, TOF and ECL. Invariant mass was calculated assuming the nominal lepton mass for both tracks;

$$M^2_{l^+l^-} = \left(\sqrt{M_l^2 + |\vec{P}_{l^+}|^2} + \sqrt{M_l^2 + |\vec{P}_{l^-}|^2}\right)^2 - |\vec{P}_{l^+} + \vec{P}_{l^-}|^2,$$

where M_l is the nominal mass of identified lepton (μ or e)[¶]. Figure 7.3 shows invariant mass distribution. For the electron mode, there is a large tail due to the final-state radiation and

[¶]Mass of muons and electrons are $105.7MeV/c^2$ and $0.511\ MeV/c^2$, respectively.

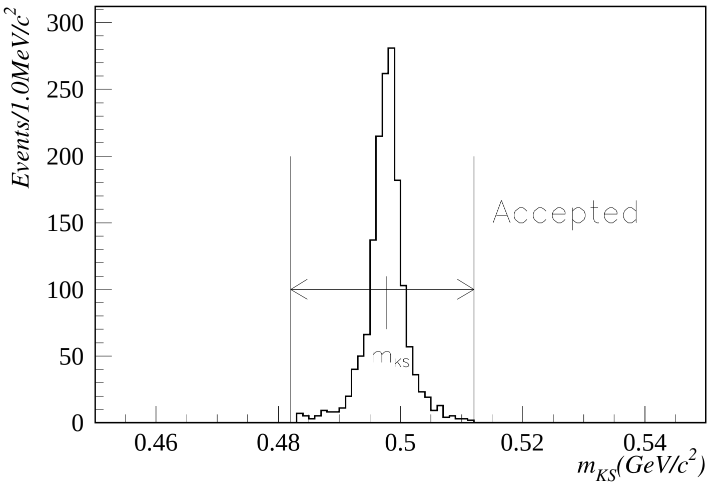

Figure 7.2: *Invariant mass distribution of K_S for selected $B \to J/\psi K_S$ candidates in MC-data.*

Table 7.3: *J/ψ branching ratios to decay modes of interest.*

Decay mode	BR	Used
$J/\psi \to e^+e^-$	$(6.02 \pm 0.19)\%$	∘
$\mu^+\mu^-$	$(6.01 \pm 0.19)\%$	∘
$2(\pi^+\pi^-)\pi^0$	$(3.37 \pm 0.26)\%$	–
$3(\pi^+\pi^-)\pi^0$	$(2.9 \pm 0.6)\%$	–
$\pi^+\pi^-\pi^0$	$(1.50 \pm 0.20)\%$	–
$2(\pi^+\pi^-)$	$(4.0 \pm 1.0) \times 10^{-3}$	–
$3(\pi^+\pi^-)$	$(4.0 \pm 2.0) \times 10^{-3}$	–

large bremsstrahlung effect. We selected candidates with the following criteria;

$$-0.025 < M_{\mu^+\mu^-} - M_{J/\psi} < +0.025 GeV,$$
$$-0.075 < M_{e^+e^-} - M_{J/\psi} < +0.025 GeV,$$

where $M_{J/\psi}$ is the nominal J/ψ mass ($M_{J/\psi} = 3096.9 MeV/c^2$). In order to keep high reconstruction efficiency, acceptance for electrons was wider than that for the muon mode. Resolutions of J/ψ mass are 8.0 MeV for $\mu^+\mu^-$ and 9.2 MeV for e^+e^- modes.

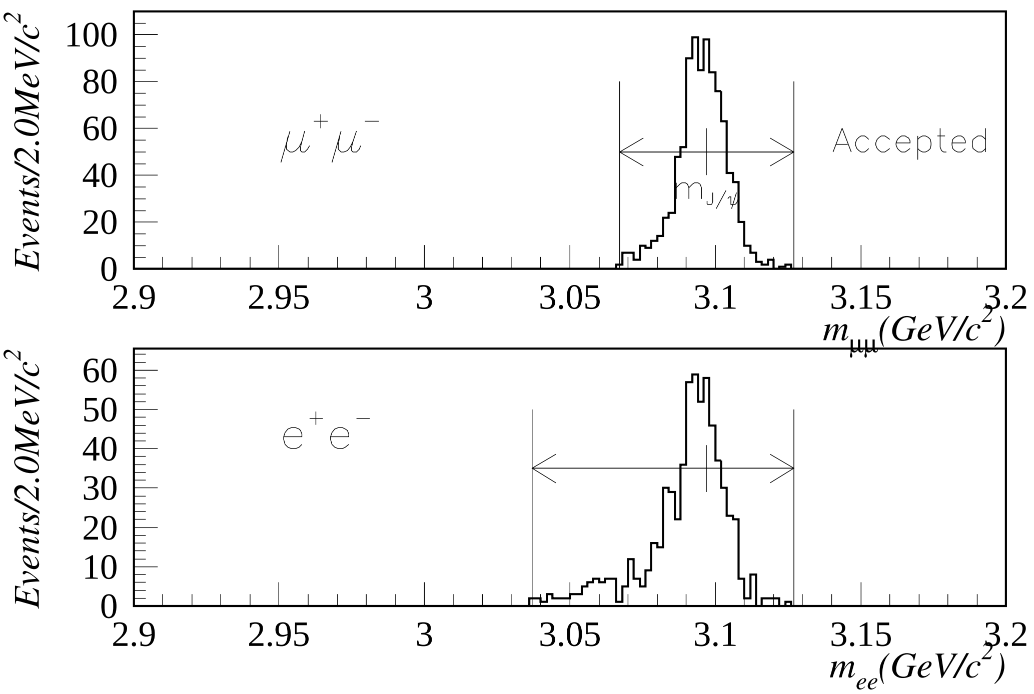

Figure 7.3: *J/ψ mass distribution for selected $B \to J/\psi K_S$ candidates in MC-data.*

7.3.3 Reconstruction of B^0 candidate.

The invariant mass of B^0 candidates were reconstructed assuming that K_S and J/ψ candidates have their nominal mass value.

$$M^2_{J/\psi K_S} = \left(\sqrt{M^2_{J/\psi} + |\vec{P}_{J/\psi}|^2} + \sqrt{M^2_{K_S} + |\vec{P}_{K_S|^2}}\right)^2 - |\vec{P}_{J/\psi} + \vec{P}_{K_S}|^2.$$

The invariant mass and momentum at the $\Upsilon(4S)$ rest frame, $p^*_{B^0}$, for $B \to J/\psi K_S$ are shown in Figure 7.4. The candidates were selected with the following criteria:

$$|M_{B^0} - M_{J/\psi K_S}| < 0.025 GeV/c^2,$$

$$0.19 < P^*_{B^0} < 0.47 GeV/c,$$

where M_{B^0} is nominal B^0 mass($M_{B^0} = 5.279 GeV/c^2$). The resolutions of B mass are $6.1 MeV/c^2$ for $\mu^+\mu^-$ and $6.4 MeV/c^2$ for e^+e^-.

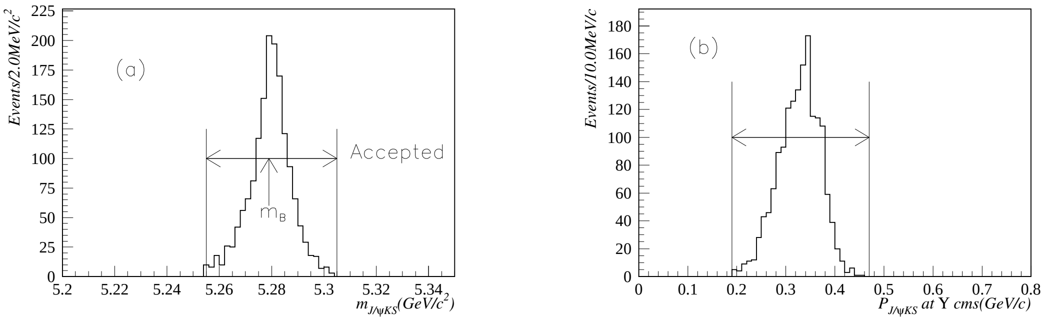

Figure 7.4: *(a) Invariant mass distributions and (b) Momentum at $\Upsilon(4S)$ rest frame of the reconstructed B for $B \to J/\psi K_S$ in MC-data.*

7.3.4 Flavor tagging

As described in Section 2.4.4, the flavor of B_{tag} has the correlation with daughter leptons and kaons;

$$B^0 \to l^+ \text{ or } K^+, \qquad \bar{B}^0 \to l^- \text{ or } K^-. \tag{7.1}$$

First of all, we reject the tracks which belong to B_{CP}. The remaining tracks are assumed to be from B_{tag}. Then we try to find the lepton from B_{tag} with momentum at $\Upsilon(4S)$ rest frame larger than 1.2GeV/c. The flavor of B_{tag} is determined with the lepton charge following the relation (7.1). If the high momentum lepton is not found, we look for a kaon. Charged kaon is identified with combined information from CDC, ACC, TOF and ECL. If the charge sum is positive (negative), B_{tag} is identified as B^0 ($\bar{B}^0$)[‖]. If the charge sum is zero, this event can not be tagged and discarded. .

The tagging probability of 39.7% is obtained for $B \to J/\psi K_S$. The estimation of wrong tagging fraction will be explained in Section 8.1.2.

7.3.5 Vertex Reconstruction

The reconstruction of the decay vertices of two B's is performed in the same way as described in Section 6.2. In order to reject vertices accidentally reconstructed in random combination for V_{CP} as we also performed in Section 6.2.2, we required a candidate to have smaller reduced χ^2 of fitting than a threshold (=10.0). The distribution of the reduced χ^2 is shown in Figure 7.5[**].

[‖]In order to reject tracks from decay in flight and misreconstructed one, tracks are required to have impact parameters of dr ≤5mm and dz ≤15mm. The definitions of dr and dz refer to Figure 6.1

[**]The distribution of Figure 7.5 includes background events since we treated event generated with simulation as real data in this section. On the other hand, Figure 6.5(a) does not include any background events.

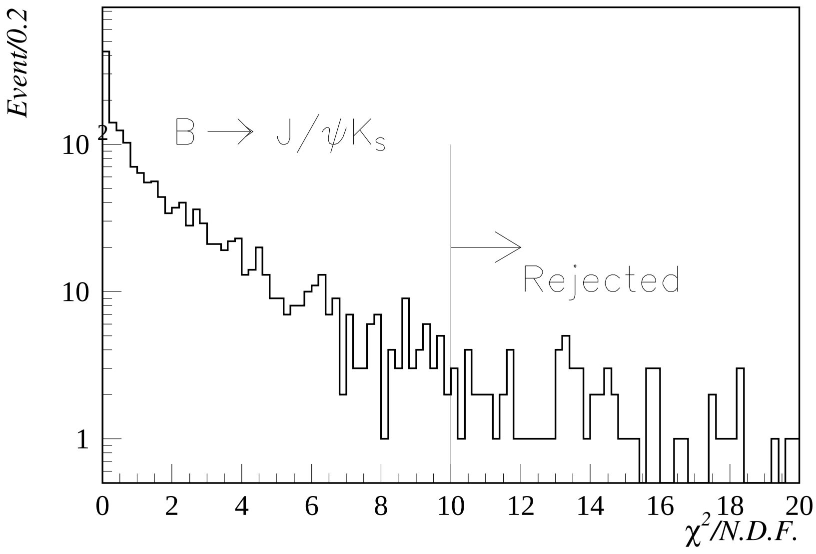

Figure 7.5: *The distribution of the reduced χ^2 of V_{CP} reconstruction for $B \to J/\psi K_S$ in MC-data. The distribution includes background events from $B^0\bar{B}^0$, B^+B^- and continuum.*

We obtained the reconstruction efficiency of 94.1% for CP side and 99.1% for tagging side. The estimation of vertex resolution will be explained in Section 8.1.3.

After all the selection, 677 candidate events remained.

7.4 Event Selection for Other Modes

The event selection for other modes, $B \to \psi(2S)K_S$, $B \to \chi_{c1}K_S$ and $B \to \eta_c K_S$, follows the same line as $B \to J/\psi K_S$. However, some additional cuts are adopted to suppress background events, especially from continuum.

In the following, selection for each decay mode is briefly explained. A full description is given in Appendix C.

7.4.1 Event selection for $B \to \psi(2S)K_S$

The decay modes of ψ(2S) are shown in Table 7.4. The $\psi(2S)$ reconstruction of the decays to two leptons, $\psi(2S) \to \mu^+\mu^-$ and $\psi(2S) \to e^+e^-$, follows the same procedure outlined for J/ψ. Though these decay modes have lower branching ratio($\sim$ 1.7%) than that of J/ψ, the mass width of $\psi(2S)$ is small enough (277 ± 31keV) to reject combinatorial background with mass selection. Thus this mode is as clean as J/ψ mode.

We also used $\psi(2S)$ decaying into $J/\psi\pi^+\pi^-$(30.2%), where J/ψ is reconstructed with two leptons.

In order to reject the background from continuum, we added the cut with event topology[††].

Table 7.4: $\psi(2S)$ *branching ratios to decay modes of interest.*

Decay mode	BR	Used
$\psi(2S) \to e^+e^-$	$(8.5 \pm 0.7) \times 10^{-3}$	∘
$\mu^+\mu^-$	$(7.7 \pm 1.7) \times 10^{-3}$	∘
$J/\psi\pi^+\pi^-$	$(30.2 \pm 1.9)\%$	∘
$J/\psi\pi^0\pi^0$	$(17.9 \pm 1.8)\%$	–
$\gamma\chi_{c0}$	$(9.3 \pm 0.9)\%$	–
$\gamma\chi_{c1}$	$(8.7 \pm 0.8)\%$	–
$\gamma\chi_{c2}$	$(7.8 \pm 0.8)\%$	–

Table 7.5: χ_{c1} *branching ratios to decay modes of interest.*

Decay mode	BR	Used
$\chi_{c1} \to J/\psi\gamma$	$(27.3 \pm 1.6)\%$	∘
$3(\pi^+\pi^-)$	$(2.2 \pm 0.8)\%$	–
$2(\pi^+\pi^-)$	$(1.6 \pm 0.5)\%$	–
$\pi^+\pi^-K^+K^-$	$(9 \pm 4) \times 10^{-3}$	–
$\rho^0\pi^+\pi^-$	$(3.9 \pm 3.5) \times 10^{-3}$	–
$K^+\bar{K}^*(892)^0\pi^-$ + c.c.	$(3.2 \pm 2.1) \times 10^{-3}$	–
$\pi^+\pi^-p\bar{p}$	$(1.4 \pm 0.9) \times 10^{-3}$	–

Applying all the selection criteria, we obtained 181 candidate events.

7.4.2 Event selection for $B \to \chi_{c1}K_S$

Table 7.5 shows the branching ratios of χ_{c1}. χ_{c1} were reconstructed through its decays to $\gamma J/\psi$, $J/\psi \to \mu^+\mu^-$ or e^+e^-. In our analysis, we use photons only for this mode to reconstruct B meson. When photons are included in B reconstruction, the efficiency is generally worse due to the detection efficiency of photon($\sim$ 70%).

The largest background for the χ_{c1} signal is due to random combination of γ from $\pi^0 \to \gamma\gamma$ associated with correctly reconstructed J/ψ from B meson decays. Therefore if a γ candidate forms an invariant mass within +10,-20MeV/c^2 of the known π^0 mass when combined with any other γ (energy above $150MeV/c^2$) in the event, it is rejected. The same event topology cut as that for $B \to \psi(2S)K_S$ was also added.

Applying all the selection criteria, we obtained 124 candidate events.

7.4.3 Event selection for $B \to \eta_c K_S$

The reconstruction of $B^0 \to \eta_c K_S$ is challenging from the experimental point of view. Because of the large width($13.2^{+3.8}_{-3.2}$MeV) of η_c[46, 91], a substantial number of combinatorial background events remain after mass and momentum cuts alone. Also the large track multiplicity causes lower reconstruction efficiency.

At the BELLE experiment, however, we have a good K/π separation capability up to 3.5 GeV/c and good vertex resolution with the silicon vertex detector. These features are quite powerful in order to reduce the background fraction substantially. Since we anyway need to know the decay vertex position of both B-mesons to observe indirect CP violation, we practically have negligible loss in the reconstruction efficiency by introducing cuts on a vertex quality.

Table 7.5 shows the branching ratios of η_c. In this study, we reconstruct the following three modes in which η_c decays into four charged hadrons:

$\eta_c \to K^+K^-\pi^+\pi^-$	(Branching Ratio	=2.0%)
$\eta_c \to 2(\pi^+\pi^-)$	(	=1.2%)
$\eta_c \to 2(K^+K^-)$	(	=2.1%)

††While the continuum event has jetlike structure, $B^0\bar{B}^0$ event has spherical structure.

η_c**(1S) DECAY MODES**	Fraction(Γ_i/Γ)		Confidence level
Decays involving hadronic resonances			
$\eta'(958)\pi\pi$	(4.1 ± 1.7)	$\%$	
$\rho\rho$	(2.6 ± 0.9)	$\%$	
$K^*(892)^0 K^- \pi^+ + c.c.$	(2.0 ± 0.7)	$\%$	
$K^*(892)\bar{K}^*(892)$	(8.5 ± 3.1)	$\times 10^{-3}$	
$\phi\phi$	(7.1 ± 2.8)	$\times 10^{-3}$	
$a_0(980)\pi$	< 2	$\%$	90%
$a_2(1320)\pi$	< 2	$\%$	90%
$K^*(892)\bar{K}$+c.c.	< 1.28	$\%$	90%
$f_2(1270)\eta$	< 1.1	$\%$	90%
$\omega\omega$	< 3.1	$\times 10^{-3}$	90%
Decays into stable hadrons			
$K\bar{K}\pi$	(5.5 ± 1.7)	$\%$	
$\eta\pi\pi$	(4.9 ± 1.8)	$\%$	
$\star$ $K^+K^-\pi^+\pi^-$[92]	$(2.0^{+0.7}_{-0.6})$	$\%$	
$\star$ $2(K^+K^-)$[93]	(2.1 ± 1.2)	$\%$	
$\star$ $2(\pi^+\pi^-)$[94]	(1.2 ± 0.4)	$\%$	
$p\bar{p}$	(1.2 ± 0.4)	$\times 10^{-3}$	
$K\bar{K}\eta$	< 3.1	$\%$	90%
$\pi^+\pi^- p\bar{p}$	< 1.2	$\%$	90%
$\Lambda\bar{\Lambda}$	< 2	$\times 10^{-3}$	90%
Radiative Decays			
$\gamma\gamma$	(3.0 ± 1.2)	$\times 10^{-4}$	

Table 7.6: Decay table of η_c[46].

We don't take care of intermediate resonance states in decay modes above and assume that all modes decay according to the phase space. The branching ratios of these three decay modes in Table 7.6 were measured with no constraint of intermediate states[92, 93, 94]. We didn't use the decay modes including K_S; e.g. $\eta_c \to K^+\bar{K}^0\pi^-, K^-K^0\pi^+$. These modes have different event topology compared with above three modes and the vertex reconstruction of B meson becomes more complicated.

Since η_c has large width, the B^0 candidates are reconstructed with the combination of K_S and η_c using mass and vertex constrained fit. In addition to cuts on event topology, we applied a cut on the momentum of η_c daughters. Requiring all the selection criteria, 273 candidate events remained.

7.5 Background Estimation

The number of background was estimated by fitting the mass distribution of B mesons. We used the region of $5.15 \leq m_B \leq 5.35 GeV/c^2$ in order to include the candidates outside signal region.

Figure 7.6 shows the distributions of reconstructed B mass and fitted results. We used a linear function plus double Gaussian function for $B \to J/\psi K_S$. The number of background in the signal region was estimated to be 8.8 ± 4.5 events.

For other modes, a linear function plus single Gaussian was used since the S/N ratio is not good as that of $J/\psi K_S$. The number of background in the signal region was estimated to be 21.6 ± 7.2 for $B \to \psi(2S)K_S$, 17.5 ± 7.2 for $B \to \chi_{c1}K_S$ and 75.9 ± 12.5 for $B \to \eta_c K_S$, respectively.

In order to check the validity of the background estimation method, we generated independent Monte Carlo events and counted the number of background events quoting the generator information. The full description of such studies is given in Appendix D and the results are consistent with the numbers obtained in this section.

7.6 Summary

Table 7.7 shows the selection criteria and the number of survived events at each step. While $J/\psi K_S$ has the largest contribution, we also see that other modes in total has the similar number of events.

We also list the numbers of estimated background events and their ratios to the numbers of observed events, which should include all the types of backgrounds, *i.e.* $B^0\bar{B}^0$, B^+B^- and continuum. From the table we see that the background fractions are reasonably low for all modes.

Table 7.7: *Results of event selection for all modes.*

Mode	$B \to J/\psi K_S$	$B \to \psi(2S)K_S$	$B \to \chi_{c1}K_S$	$B \to \eta_c K_S$
B^0 recon	1865	553	396	6306
Event topology cut	-	522	391	2892
Flavor tagging	740	230	145	1013
CP-vertex	696	207	133	821
Tagging-vertex	690	197	131	815
Mass constraint fit	-	-	-	328
K_S vertex cut	677	181	124	303
η_c daughter momentum	-	-	-	273
final candidate	677	181	124	273
estimated background	8.8 ± 4.5	21.6 ± 7.2	17.5 ± 7.2	75.9 ± 12.5
background/events($\equiv r_{bg}$)	0.01	0.12	0.14	0.28

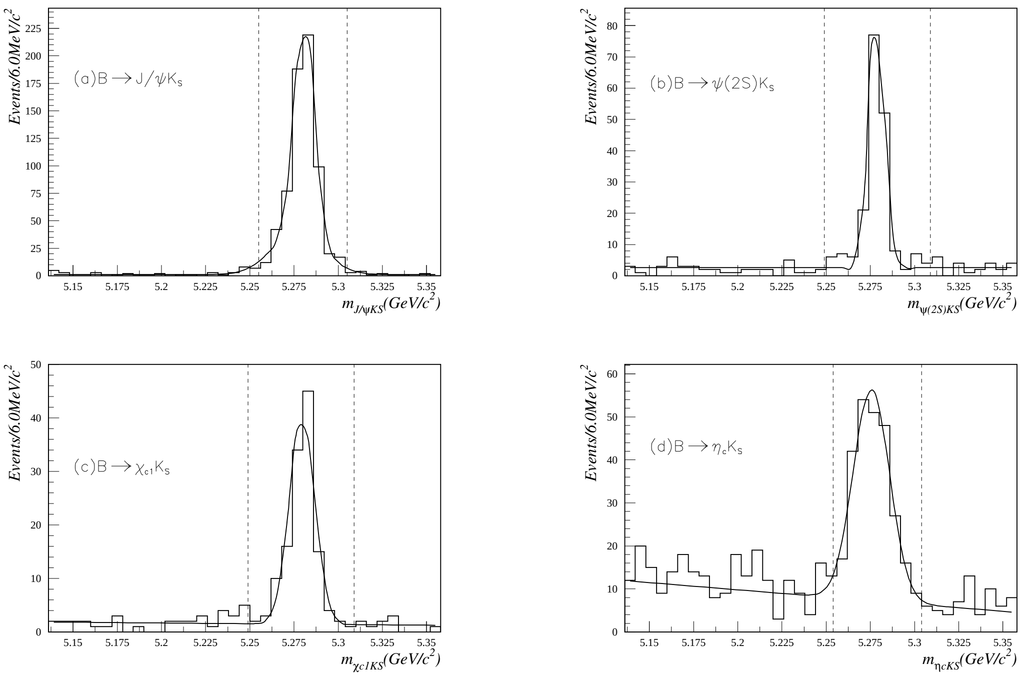

Figure 7.6: *The mass distribution of B mesons for (a)* $B \to J/\psi K_S$*, (b)* $B \to \psi(2S)K_S$*, (c)* $B \to \chi_{c1}K_S$ *and (d)* $B \to \eta_c K_S$ *in MC-data. Solid lines are fitted results to estimate the number of background. Dashed lines show the signal region.*

Chapter 8

Measurement of $\sin 2\phi_1$

In this chapter, we extract the parameter $\sin 2\phi_1$ from the MC-data sample selected in the previous chapter. We will estimate the sensitivity and its statistical and systematic errors at the integrated luminosity of 100 fb^{-1}, which will be obtained with one year of running if the design luminosity of KEKB is achieved.

In Section 8.1, we will explain the proper time distribution taking detector effect into account. Then, we give the fit results in Section 8.2. Systematic errors are discussed in section 8.3. Section 8.4 summarizes this chapter.

8.1 Proper time distribution

The parameter of CP asymmetry, $\sin 2\phi_1$, is obtained from the proper time distributions. The proper time distribution is shown in Figure 8.1 for $B \to J/\psi K_S$ events selected in the previous chapter.

Since the proper time, τ, is measured as the distance of decay vertices of two B mesons, the finite resolution of vertex reconstruction degrades observed CP asymmetry. The asymmetry is also diluted by wrong B-flavor tagging mainly due to imperfection of the detector response[1]. Under the condition of finite τ resolution and imperfect flavor tagging, the proper time distribution (6.4) becomes

$$F(\tau) = (1 - r_{bg}) \int_{-\infty}^{\infty} g(\tau, \tau') \left\{ \frac{1}{2} e^{-|\tau'|} (1 \pm (1 - 2\omega) \sin 2\phi_1 \sin x_d \tau') \right\} d\tau' + r_{bg} f_{bg}(\tau) \quad (8.1)$$

where r_{bg} is the ratio of the number of backgrounds, which is the sum of $B^0\bar{B}^0$, B^+B^- and the continuum events, to that of observed events, g the response function from finite proper time resolution and ω is the wrong tagging fraction in flavor tagging of B meson, and f_{bg} the proper time distribution of background events.

In the fitting of proper time distribution, therefore, we need to define the following parameters and functions:

- the background function, f_{bg},
- the tagging correction factor, $(1 - 2\omega)(\equiv A_{tag})$,
- the response function, g.

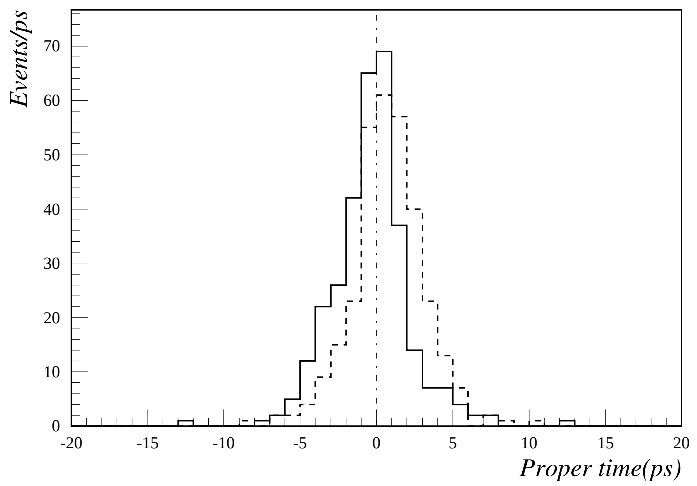

Figure 8.1: *The proper time distribution of events selected in $B \to J/\psi K_S$ MC-data. The solid line is for events tagged by B^0. The dashed line is for events tagged by $\bar{B}^0$.*

8.1.1 Background function

The background function, f_{bg}, is defined as:

$$f_{bg}(\tau) = \frac{1}{2} e^{-|\tau \cdot \tau_B / \tau_{bg}|} (1 \pm CP_{bg} \sin x_d \tau), \tag{8.2}$$

where, the plus (minus) sign in front of CP_{bg} corresponds to B_{CP} tagged by B^0 ($\bar{B}^0$), τ_{bg} and CP_{bg} were decay time and CP asymmetry value of background. Since the decay time of background, τ_{bg}, includes proper time resolution, f_{bg} was not smeared with response function.

The decay time and CP asymmetry of background were measured with the events collected in the "mass sideband" region for $B \to \eta_c K_S$. For other modes, we collected events in the "mass and momentum sideband" region since the number of events inside the mass sideband was too small to measure decay time and CP asymmetry of background. The definition of the sideband region is shown in Figure 8.2. The mass and momentum of reconstructed B at $\Upsilon(4S)$ rest frame for $B \to J/\psi K_S$ MC-data is also shown. Since there is no way to know what the background source is, any type of background, $B^0\bar{B}^0$, B^+B^- and continuum, was treated simultaneously. Then we measured the decay time and CP asymmetry by fitting the Δz distribution with the following function :

$$f(\tau) = \frac{1}{2} e^{-\frac{|\Delta z|}{\tau_{bg} c\beta\gamma}} (1 + CP_{bg} \sin x_d \frac{\Delta z}{c\beta\gamma}), \tag{8.3}$$

[1]Proper time distribution (6.4) in reality must be modified to

$$\begin{aligned} f(\tau) &= (1-\omega) \cdot \frac{1}{2} e^{-|\tau|} (1 \pm \sin 2\phi_1 \sin x_d \tau) + \omega \cdot \frac{1}{2} e^{-|\tau|} (1 \mp \sin 2\phi_1 \sin x_d \tau) \\ &= \frac{1}{2} e^{-|\tau|} (1 \pm (1-2\omega) \sin 2\phi_1 \sin x_d \tau). \end{aligned}$$

where ω is the wrong tagging fraction.

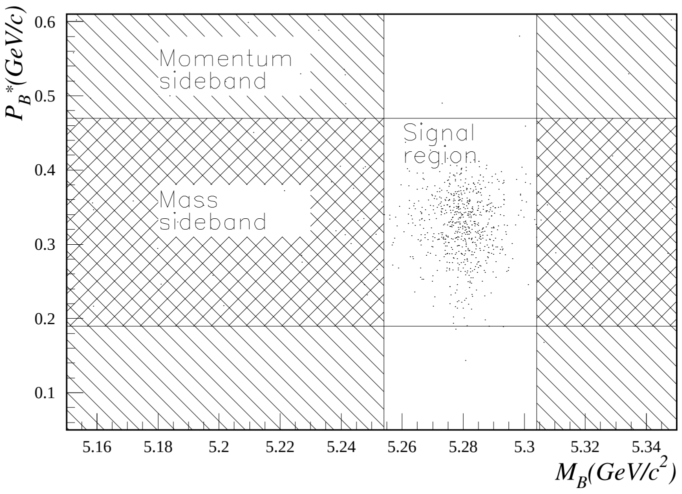

Figure 8.2: *The definition of sideband region. The double hatched area is mass sideband. The hatched area is momentum sideband. Dots are events selected for $B \to J/\psi K_S$ in MC-data.*

Table 8.1: *The estimated number, decay time and CP asymmetry of background.*

	$B \to J/\psi K_S$	$B \to \psi(2S) K_S$	$B \to \chi_{c1} K_S$	$B \to \eta_c K_S$
Decay time, $\tau_{bg}[ps]$	1.36±0.16	1.37±0.11	2.02±0.22	0.68±0.04
CP_{bg}	+0.21±0.21	+0.09±0.15	-0.19±0.16	-0.09±0.13

where τ_{bg} and CP_{bg} were decay time and asymmetry of the background. Figure 8.3 shows the Δz distribution for the mass and momentum sideband events in $B \to J/\psi K_S$ MC-data, together with the background function. In the figures, the distribution of events tagged by B^0 was inverted and added to events tagged by $\bar{B}^0$. In this way a systematic shift of the Δz distribution is canceled out in the fitting of the background function. The estimated CP asymmetry and lifetime of background are summarized in Table 8.1.

8.1.2 Correction factor for flavor tagging

As described in (8.1), the observed asymmetry is diluted with the factor (1-2ω) where ω is the wrong tagging fraction for flavor tagging of B meson . In order to calculate the true $\sin 2\phi_1$, we need to measure the correction factor, (1-2ω)($\equiv A_{tag}$), and its error.

We estimated A_{tag} using the mode where one B is fully reconstructed as $B \to J/\psi K^{*0}$ and $K^{*0} \to K^{\pm}\pi^{\mp}$. The flavor of this B is given by the charge of daughter particles, $K^{\pm}$ and $\pi^{\mp}$, from K^{*0}.

Suppose there was no B^0-$\bar{B}^0$ mixing, the flavor of the other B should be opposite to that of $B \to J/\psi K^{*0}(\to K^{\pm}\pi^{\mp})$. Therefore by applying the standard flavor tagging procedure to the other B, we obtain the following relation;

$$\frac{N_{correct} - N_{wrong}}{N_{correct} + N_{wrong}} = \frac{(1-\omega)N_{OBS} - \omega N_{OBS}}{N_{OBS}} = (1-2\omega), \tag{8.4}$$

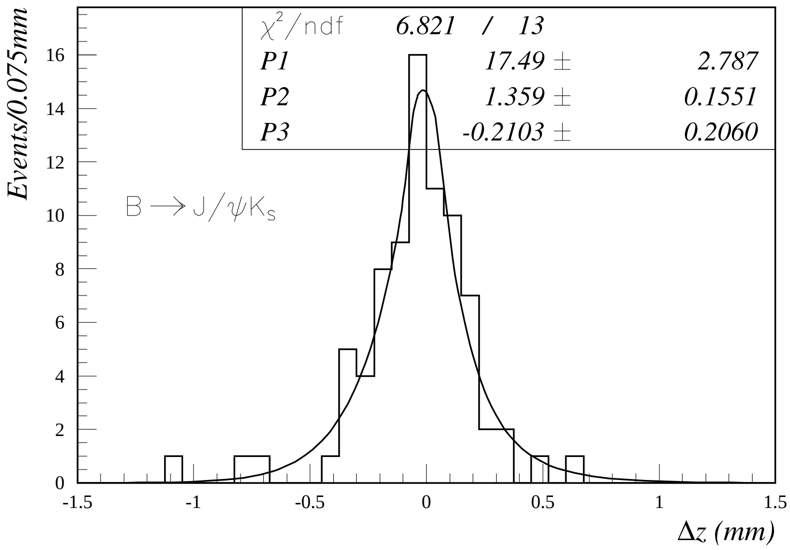

Figure 8.3: *Δz distribution of the mass and momentum sideband events for $B \to J/\psi K_S$ in MC-data. The distribution of events tagged by B^0 is inverted and added to events tagged by $\bar{B}^0$.*

where $N_{correct}(N_{wrong})$ is the number of the events with the correct (wrong) answer and N_{OBS} is the number of observed events. Since the flavor of neutral B mesons change by $B^0\bar{B}^0$ mixing, Equation 8.4 is modified as a function of $\tau(\equiv \Delta t/\tau_B)$. We defined the quantity A_{OBS} as

$$A_{OBS}(\tau) = \frac{N_{correct}(\tau) - N_{wrong}(\tau)}{N_{correct}(\tau) + N_{wrong}(\tau)} = (1-2\omega)\cos x_d\tau + I \simeq A_{tag}\cos x_d\tau, \tag{8.5}$$

where x_d is the $B^0\bar{B}^0$ mixing parameter ($=\Delta m/\Gamma_B$) and I is the intrinsic asymmetry which we ignore in this study[1].

The event selection for $B \to J/\psi K^{*0}$ is described in Appendix E. Since this mode has larger branching ratio than that of $B \to J/\psi K_S$, we obtained 1014 events. The signal to background ratio was estimated to be quite high (~ 40). The observed asymmetry, A_{OBS}, defined as (8.5) is shown in Figure 8.4. Taking the effect of shift with vertex reconstruction into account, the distribution was fitted with the following function;

$$f(\Delta z) = A_{tag} \times \cos(x_d \frac{\Delta z - \delta z}{\tau_B c\beta\gamma}), \tag{8.6}$$

where A_{tag}, x_d and δz are free parameters. We obtained the result

$$A_{tag} = 0.742 \pm 0.029,$$

which is consistent to the value obtained in the analysis of independent Monte Calro events using generator information shown in Table D.2 in Appendix D.

[1]The intrinsic asymmetry arises mainly from the difference in the detector response between positively and negatively-charged particles. This effect, however, cancels by fitting the proper time distributions of B^0 and $\bar{B}^0$-tagged events simultaneously.

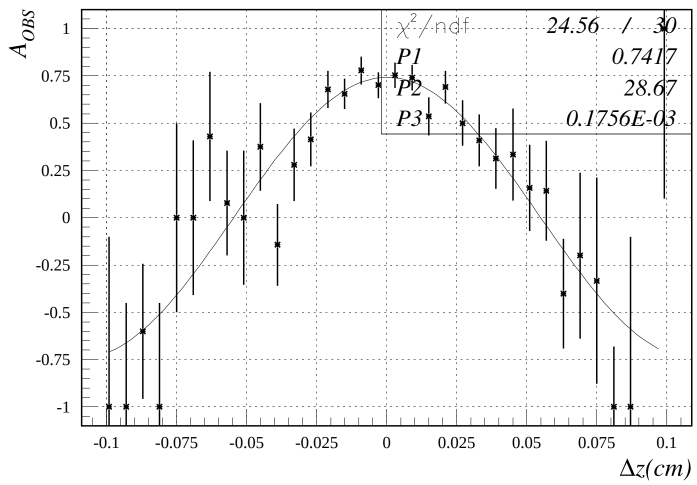

Figure 8.4: *In order estimate the wrong tagging fraction for flavor tagging, the tagging asymmetry, A_{OBS} is fitted for $B \to J/\psi K^{*0}$ in MC-data.*

8.1.3 Response function of vertex reconstruction

In a decay mode where B decays into non CP eigenstate, the proper time distribution, $f(\tau)$, is a simple exponential function since CP asymmetry doesn't appear;

$$f(\tau) = \frac{1}{2\tau_B} \exp(\frac{-|\tau|}{\tau_B}), \tag{8.7}$$

where $\tau(\tau')$ is the normalized proper time, $\Delta t/\tau_B$, Δt is related to the vertex position difference of two B mesons by $\Delta t = \Delta z/c\gamma\beta = (z_{tag} - z_{CP})/c\gamma\beta$. This exponential distribution is smeared due to a finite vertex resolution, which is expressed with the response function, g, which in this study is defined as a single Gaussian function for simplicity:

$$g(\tau, \tau', \sigma, m) = \frac{1}{\sqrt{2\pi}\sigma} \exp(\frac{-(\tau - m - \tau')^2}{2\sigma^2}). \tag{8.8}$$

where m is mean and σ is standard deviation. The proper time distribution is fitted to reproduce the given lifetime of B meson with the convolution of f and g;

$$F(\tau) = \int_{-\infty}^{\infty} d\tau' g(\tau, \tau', \sigma, m) f(\tau'). \tag{8.9}$$

$$\tag{8.10}$$

The fit was performed with σ and m as free parameters. The lifetime of B meson was set to be 1.56 ± 0.04ps[46].

We used the mode $J/\psi K^*$, $K^{*0} \to K^+\pi^-$ studied in Section 8.1.2. This mode has a similar decay topology with $B \to J/\psi K_S$. Although the momentum distribution of J/ψ is not identical due to the mass difference between K_S and K^{*0}, the effect would be small since leptons from J/ψ have high momentum ($\sim 1.0GeV/c$) and the difference of J/ψ momentum is about 150MeV/c.

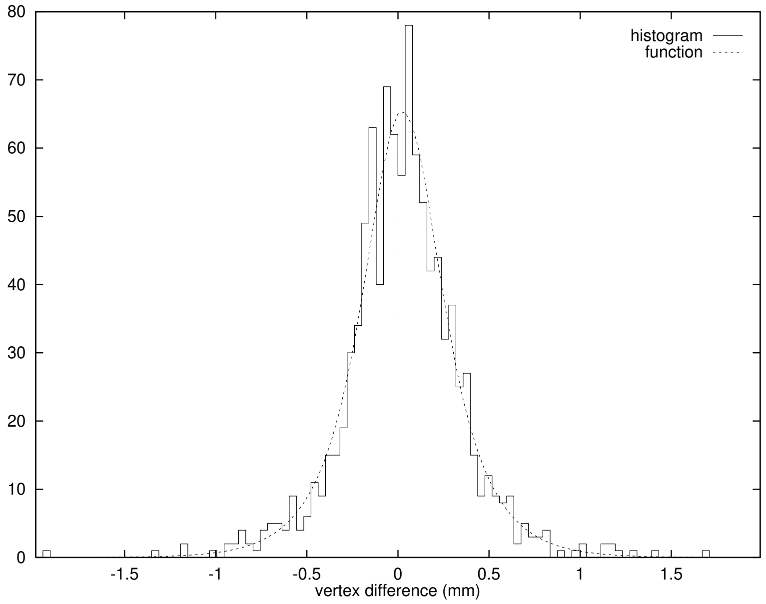

Figure 8.5: *Estimation of response function. The proper time distribution of* $B \to J/\psi K^{*0}$ *was fitted with the exponential function convoluted with the Gaussian response function.*

Also the resolution of Δz is dominated by that of the tagging side which is identical for both decay modes. Therefore we expect that the response function obtained with $B \to J/\psi K^{*0}$ is approximately the same as that for all signal modes.

Figure 8.5 shows the fitting result. The both samples tagged as B^0 and $\bar{B}^0$ were merged in the fit and Δz vertex distribution was fitted with response function. We obtained the following values:

$$\sigma = 124.5 \pm 13.4\mu m, \qquad m = 26.6 \pm 10.9\mu m.$$

This result was consistent to the values obtained in Chapter 6. We use them for all signal modes.

8.2 Fitting Result

The proper time distributions were fitted for the events tagged as B^0 and $\bar{B}^0$ simultaneously with an unbinned maximum likelihood method[95]. The likelihood function for i-th event, $\mathcal{L}_i$, is determined as Equation (8.1). The total likelihood for event sample, $\mathcal{L}_{tot}$, is

$$\begin{aligned} \mathcal{L}_{tot} &= \prod_i^n \mathcal{L}_i \\ &= \prod_i^n \left[(1 - r_{bg}) \int_{-\infty}^{\infty} g(\tau_i, \tau') \left\{ \frac{1}{2} e^{-|\tau'|} (1 \pm A_{tag} \sin 2\phi_1 \sin x_d \tau') \right\} d\tau' + r_{bg} f_{bg}(\tau_i) \right] \end{aligned} \tag{8.11}$$

We calculate the $\sin 2\phi_1$ which maximizes $\mathcal{L}_{tot}$. Fitting was performed for each mode. Figure 8.6 shows the case for $B \to J/\psi K_S$. Table 8.2 summarizes the results with statistical errors. For the combined result, all the distributions were fitted simultaneously.

Since event samples to measure $\sin 2\phi_1$ are independent with that in $B \to J/\psi K^{*0}$ used for measuring A_{tag}, the tagging correction factor has statistical fluctuation which is included in the errors in Table 8.2. We calculated this fluctuation as:

$$\delta(A_{tag}) = \delta(1-2\omega) = 2 \times \sqrt{\frac{\omega(1-\omega)}{N_{OBS}}}, \tag{8.12}$$

where N_{OBS} is the number of observed events, ω is the measured wrong tagging fraction.

Table 8.2: *Fitting result of proper time distribution*

Decay mode	$B \to J/\psi K_S$	$B \to \psi(2S) K_S$	$B \to \chi_{c1} K_S$	$B \to \eta_c K_S$	Combined
$\sin 2\phi_1$	$0.635^{+0.102}_{-0.105}$	$0.617^{+0.209}_{-0.221}$	$0.181^{+0.274}_{-0.278}$	$0.866^{+0.179}_{-0.192}$	$0.632^{+0.080}_{-0.081}$

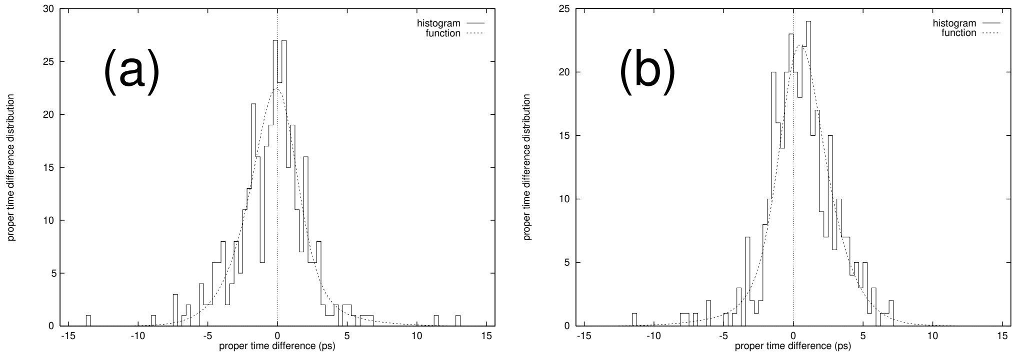

Figure 8.6: An example of CP fitting results. Fitting was performed for the events tagged (a) by B^0 and (b) by $\bar{B}^0$ for $B \to J/\psi K_S$ in MC-data.

8.3 Systematic Errors

8.3.1 Physics parameters

The world average value of the B meson lifetime is [46]

$$\tau_B = (1.56 \pm 0.04) \times 10^{-12}\ sec. \tag{8.13}$$

By varying the lifetime of B meson within the error shown above. σ and mean of the response function varied by $\pm 7.2\mu m$ and $\pm 0.5\mu m$, respectively. Variation of mean value changes $\sin 2\phi_1$ by less than 0.001. In the fitting of proper time distribution, the lifetime of B mesons and σ of response function were varied within above errors. We estimated that the systematic error from B meson lifetime is $\pm 0.009 \sim \pm 0.016$ for each mode.

The effect of $B^0 - \bar{B}^0$ mixing parameter, x_d, was also estimated with the same method. The world average value is

$$x_d = (0.723 \pm 0.032), \tag{8.14}$$

where the error of x_d is mainly due to the ambiguity of τ_B[46]. If we only changed x_d with the above error, variation of $\sin 2\phi_1$ is 0.01 and smaller than that from τ_B. Therefore we ignore the systematic error from x_d.

8.3.2 Flavor tagging

The systematic error from the estimation of the correction factor is calculated as

$$Systematic\ \ Error = \sin 2\phi_1 \times \frac{\Delta(1-2\omega)}{(1-2\omega)}, \tag{8.15}$$

which is $4\%(= 0.029/0.742)$ of the results.

8.3.3 Response function from vertex reconstruction

The errors of the mean and σ have correlation but the effect from the mean was smaller than that from σ. Therefore we varied σ and mean within its errors independently. We calculated the change by the both σ and mean, and added them in quadrature. The systematic error ranges $\pm 0.015 \sim \pm 0.036$.

8.3.4 Background function

The systematic error on $\sin 2\phi_1$ from ambiguity in the background function was estimated by recalculating $\sin 2\phi_1$ with varying the number (N_{bg}) CP asymmetry (CP_{bg}) and decay time (τ_{bg}) of the background events within the range of errors. Although CP_{bg} and τ_{bg} have correlation, it is ignored, since the effect from change of τ_{bg} was small compared to that from CP_{bg} and N_{bg} with the S/N ratio we obtained.

8.3.5 Summary

In table 8.3, systematic errors are summarized. The dominant error is from the estimation of response function in the case of $B \to J/\psi K_S$ and from background function for other modes. The sum of systematic errors was smaller than statistical errors for all modes as well as for the combined result.

8.4 Summary

We obtain the result for the integrated luminosity of 100 fb^{-1} as follows;

$$\begin{aligned}
\sin 2\phi_1 &= 0.635^{+0.102}_{-0.105}(stat.) \pm 0.046(sys.)\ (B \to J/\psi K_S), \\
&= 0.617^{+0.209}_{-0.221}(stat.)^{+0.069}_{-0.037}(sys.) \quad (B \to \psi(2S) K_S), \\
&= 0.181^{+0.274}_{-0.278}(stat.)^{+0.093}_{-0.043}(sys.) \quad (B \to \chi_{c1} K_S), \\
&= 0.866^{+0.179}_{-0.192}(stat.)^{+0.076}_{-0.057}(sys.) \quad (B \to \eta_c K_S),
\end{aligned}$$

Table 8.3: *Sources of systematic errors for the measurement of* $\sin 2\phi_1$.

The source of systematic error	$B \to J/\psi K_S$	$B \to \psi(2S) K_S$	$B \to \chi_{c1} K_S$	$B \to \eta_c K_S$	Combined
B life time	± 0.016	$^{+0.013}_{-0.011}$	$^{+0.008}_{-0.009}$	± 0.020	$^{+0.016}_{-0.014}$
Wrong tagging factor	± 0.025	± 0.024	± 0.007	± 0.034	± 0.025
Response function	± 0.035	$^{+0.019}_{-0.017}$	± 0.016	± 0.036	$^{+0.031}_{-0.029}$
Background function	$^{+0.007}_{-0.003}$	$^{+0.061}_{-0.019}$	$^{+0.091}_{-0.038}$	$^{+0.054}_{-0.019}$	$^{+0.018}_{-0.011}$
Total	± 0.046	$^{+0.069}_{-0.037}$	$^{+0.093}_{-0.043}$	$^{+0.076}_{-0.057}$	$^{+0.047}_{-0.044}$

where the first error is statistical and the second is systematic, respectively. By combining all charmonium modes, we obtain;

$$\sin 2\phi_1 \quad = \quad 0.632^{+0.080}_{-0.081}(stat.)^{+0.047}_{-0.044}(sys.).$$

The result is consistent to the input value($\sin 2\phi_1 = 0.60$).

Chapter 9

Discussion

In this chapter, we discuss the result on the measurement of $\sin 2\phi_1$. In Section 9.1, we make experimental consideration about the results. The impact of the results to the Standard Model and new physics are discussed in Section 9.2.

9.1 Experimental Consideration of the Result

In Chapter 8, we estimated the sensitivity for measurement of $\sin 2\phi_1$ with the integrated luminosity of 100fb^{-1} and $\sin 2\phi_1$ of 0.60. It will take about a year to obtain this integrated luminosity assuming the design luminosity of KEKB accelerator. It is also important to discuss how accurately we can measure $\sin 2\phi_1$ with less amount of data at the early stage of BELLE experiment. Since the systematic error is estimated with experimental data as demonstrated in this thesis, not only statistical but also systematic errors will increase with the smaller luminosity. We estimated the sensitivity of $\sin 2\phi_1$ assuming all errors except that from the uncertainty of τ_B are scaled by $\frac{1}{\sqrt{\mathcal{L}}}$, where $\mathcal{L}$ is the integrated luminosity. Figure 9.1 shows the $\delta(\sin 2\phi_1)$ as a function of integrated luminosity with $\sin 2\phi_1 = 0.60$ with all the $B \to$ charmonium$+K_S$ modes combined. We see that if $\sin 2\phi_1$ is 0.60, we can observe the asymmetry with 3σ significance with the integrated luminosity of 22fb^{-1}.

We also estimated required integrated luminosity for smaller values of $\sin 2\phi_1$. Although the sensitivity for $\sin 2\phi_1$ would change as a function of the value of $\sin 2\phi_1$, the difference is small[1]. Assuming that the sensitivity doesn't depend on the value of $\sin 2\phi_1$, we calculated required integrated luminosities to measure various values of $\sin 2\phi_1$ with a 3σ significance. Figure 9.2 shows the result. We see from the figure that we can measure $\sin 2\phi_1$ larger than 0.28 with 100fb^{-1}. Since the present allowed region is $0.34 \leq \sin 2\phi_1 \leq 0.75$ based on experimental data and the Standard Model, any value of $\sin 2\phi_1$ in the allowed region can be measured.

9.2 Sensitivity to New Physics

9.2.1 General Discussion

If ϕ_1 from measured $\sin 2\phi_1$ is inconsistent to the allowed region with the Standard Model hypothesis, this would be a possible indication of new physics beyond the SM with new CP

[1] Because of the change of the dilution factor(see Section 6.2.4), the sensitivity for $\sin 2\phi_1$ change. With the same number of events, $\delta(\sin 2\phi_1)$ for $\sin 2\phi_1$=0.1 is about 5% smaller than that for $\sin 2\phi_1$=0.6[96].

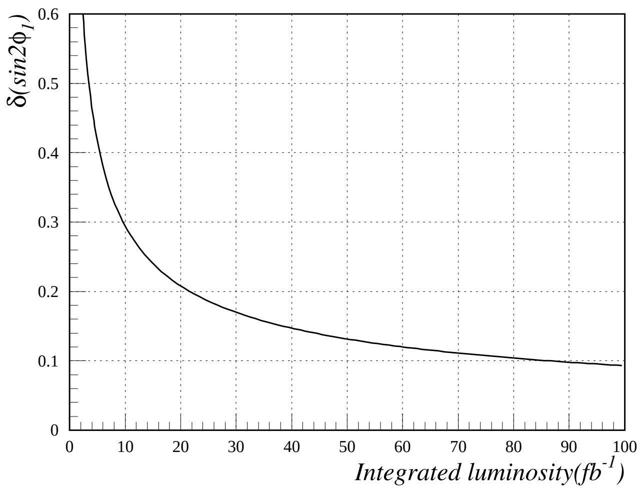

Figure 9.1: *$\delta(\sin 2\phi_1)$ as a function of integrated luminosity with* $\sin 2\phi_1$ *= 0.60 for $B \to$ charmonium $+ K_S$.*

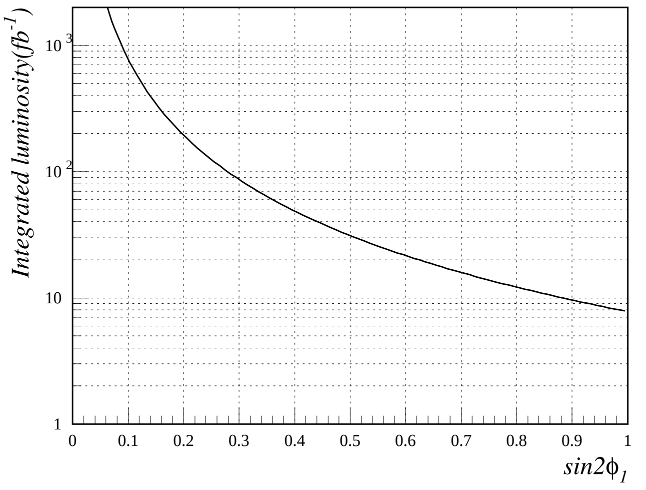

Figure 9.2: *Required integrated luminosity as a function of* $\sin 2\phi_1$ *for $B \to$ charmonium $+ K_S$.*

violation phase. In this section, we concentrate on the impact of the measurement of $\sin 2\phi_1$ to new physics.

Angle ϕ_1 has four-fold ambiguity as

$$\bar{\phi}, \quad \bar{\phi}+\pi, \quad \frac{\pi}{2}-\bar{\phi}, \quad \frac{3\pi}{2}-\bar{\phi}, \tag{9.1}$$

where we assume that $\sin 2\bar{\phi}$ is measured value and $0 \leq |\bar{\phi}| \leq \pi/2$. A measurement of $\sin 2\phi_1$ will specify four regions bounded by two rays in the ($\bar{\rho}$,$\bar{\eta}$) plane, each originating at (1,0)(Figure 9.3 for $\sin 2\phi_1$= 0.632 ± 0.093). In search for new physics, all four solutions need to be considered.

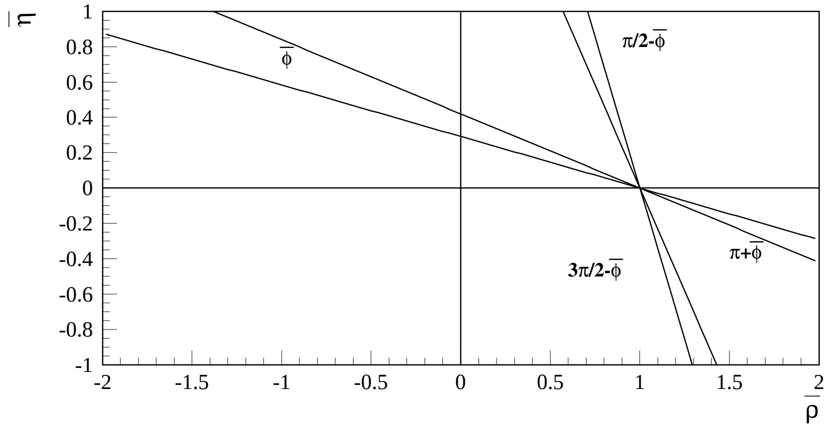

Figure 9.3: *Four fold ambiguity for* ϕ_1.

Figure 9.4 shows the present constraints on the unitarity triangle. The allowed region is constrained with three parameters extracted from individual experiments. $|V_{td}V^*_{tb}|$ is obtained from Δm_{B_d} in $B^0\bar{B}^0$ mixing. $|V_{ub}/V_{cb}|$ is obtained from $B \to X_u l\nu$. ϵ_k is obtained from indirect CP violation in $K^0\bar{K}^0$ mixing (Ref. Section 2.3). In the Standard Model, two solutions of four-fold ambiguity which extend into the negative $\bar{\eta}$ are always inconsistent with allowed region and excluded.

The allowed region with confidence level of 95% is also shown in Figure 9.4 when we obtain $\sin 2\phi_1$= 0.632 ± 0.093. The sensitivity for new physics is provided in the region of $\sin 2\phi_1 < 0.13$ and $0.94 < \sin 2\phi_1 < 1.00$ with confidence level of 95% with 100fb^{-1}. Figure 9.5 shows the region where new physics can be observed.

In an extreme case in that $\sin 2\phi_1$ is negative, all solutions are inconsistent with allowed region determined with ϵ_k within SM assumption. Figure 9.6 shows the case of $\sin 2\phi_1 = -0.632 \pm 0.093$. Some theoretical work on extra quark model shows a possibility that $\sin 2\phi_1$ would be negative[97].

As already mentioned in Chapter 2, we will be able to measure all the angles and sides of unitarity triangle with good accuracy in the BELLE experiment. Therefore it is possible to provide the better sensitivity to new physics by combining other measurements at BELLE. The uncertainty on $|V_{ub}/V_{cb}|$ is expected to decrease from 25% to about 10%[98]. The angle ϕ_3 is expected to be measured for the first time. Figure 9.7 and 9.7 show the new constraint. We used

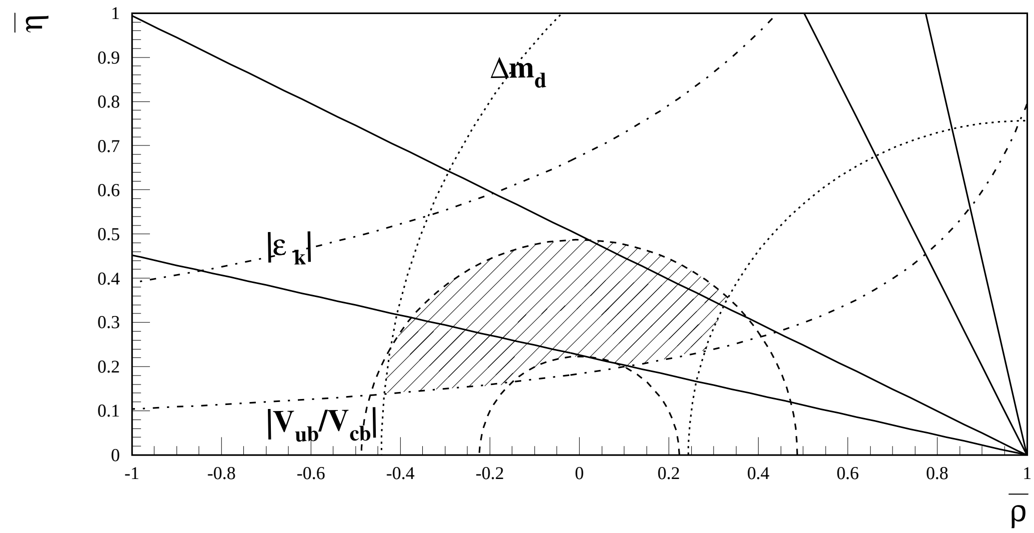

Figure 9.4: *The present constraint in the Standard Model. The region between the dashed (dotted) circles is allowed by the measurement of* $|V_{ub}/V_{cb}|$ (Δm_{B_d}). *The dash-dotted curves show the constraint following from the measurement of the* ε_k *parameter in the kaon system. Allowed region is bounded by 95% confidence level for each parameter. The solid line indicate the region constrained from the measurement of* $\sin 2\phi_1 = 0.632 \pm 0.093$. *We also define this region with 95% confidence level.*

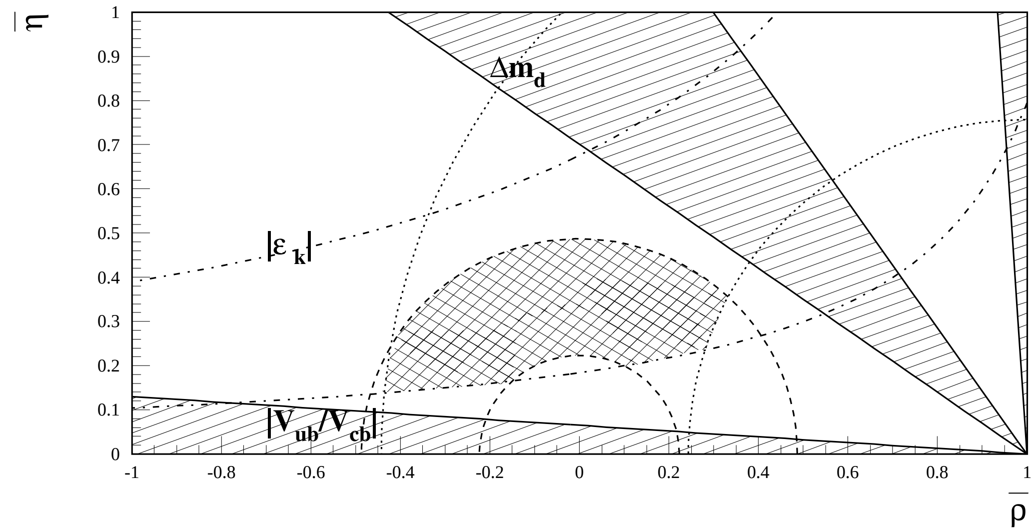

Figure 9.5: *The hatched area is the region where new physics can be observed. The double-hatched area is the region with the present constraint in the Standard Model.*

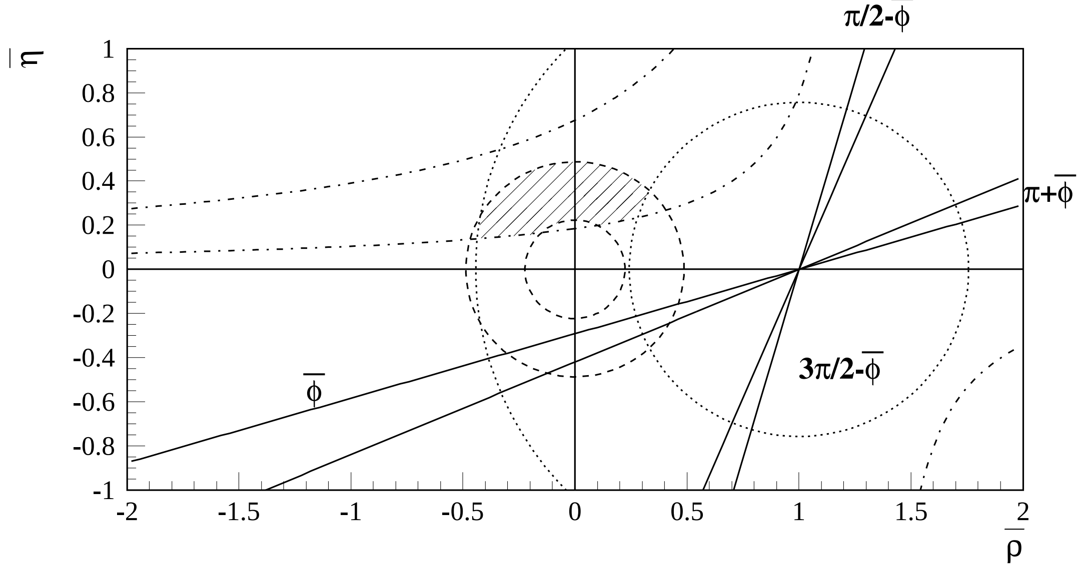

Figure 9.6: *In the case that* $\sin 2\phi_1$ *measured is negative value. The constraints are same definition as that in Figure 9.4. All solutions are inconsistent with allowed region.*

$|V_{ub}/V_{cb}|$ of 0.08 ± 0.01 and ϕ_3 of $70 \pm 15°$ at $100\mathrm{fb}^{-1}$[98][1]. If we add the constraint from new $|V_{ub}/V_{cb}|$, the sensitivity for new physics is provided in the region of $0.86 \leq \sin 2\phi_1 \leq 1.00$ and $\sin 2\phi_1 < 0.13$ with confidence level of 95% with $100\mathrm{fb}^{-1}$. Figure 9.7 shows the region where new physics can be observed. The region would be wider because of the new constraint for $|V_{ub}/V_{cb}|$. If ϕ_3 is measured to be the above value, the sensitivity for new physics is further provided in the region of $0.86 \leq \sin 2\phi_1 \leq 1.00$ and $\sin 2\phi_1 < 0.40$. Figure 9.8 shows the sensitive region for new physics.

9.2.2 ϕ_1 in Physics beyond the Standard Model

In this section, we describe the model on new physics which affect ϕ_1 measurement. The effects from new physics beyond the SM exist in both the decay and the mixing amplitude of B meson. Since the decay of $b \to c\bar{c}s$ is dominated by the tree diagram, the deviation of ϕ_1 from the prediction of SM may originate from the virtual effects of new physics in loop-mediated process in B^0-$\bar{B}^0$ mixing. [2]

The effect from new physics in B^0-$\bar{B}^0$ mixing can also vary the length of the side, especially $|V_{td}V_{tb}^*|$, of unitarity triangle. Even if new physics affect only sides of the unitarity triangle, we can observe this effects by checking that the value of the angles is inconsistent with the measured sides of the triangle. However, the ambiguity for $|V_{td}V_{tb}^*|$ is large because of theoretical uncertainty. Since the inconsistency due to the change of the side is hard to be measured, here we concentrate on the change of ϕ_1.

[1]The uncertainty on $|V_{td}V_{tb}^*|$ is dominated by theoretical one and will not be improved with the data at B-factory.

[2]The effect from new physics in the decay amplitude can be measured with comparison of the ϕ_1 measured in $B \to \phi K_S$ with that measured in $B \to$ charmonium $+ K_S$, since $B \to \phi K_S$ is a pure penguin decay mode.

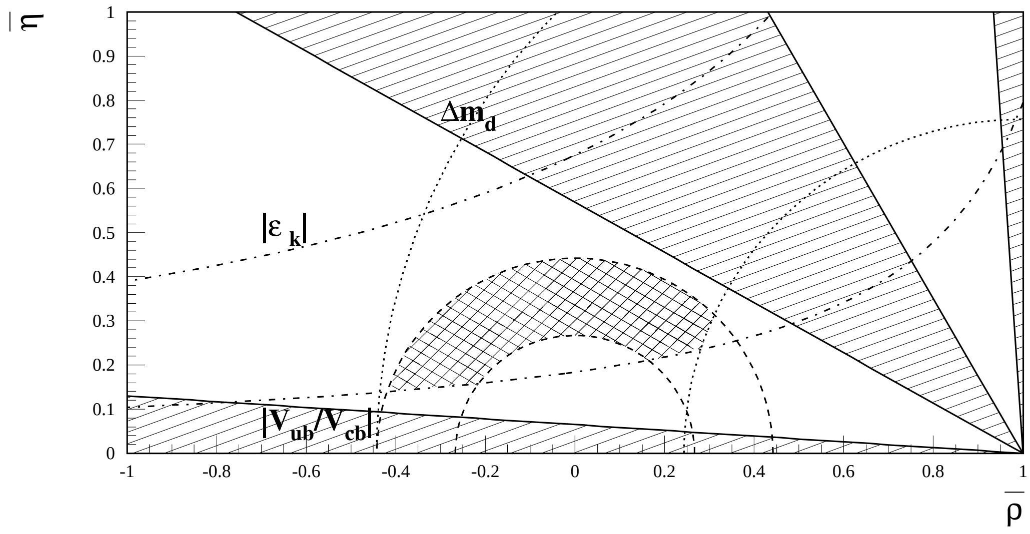

Figure 9.7: *The expected new constraints at the integrated luminosity of 100fb^{-1}. The double hatched area is constrained with new measurement of $|V_{ub}/V_{cb}|$. The hatched area is the region where new physics can be observed.*

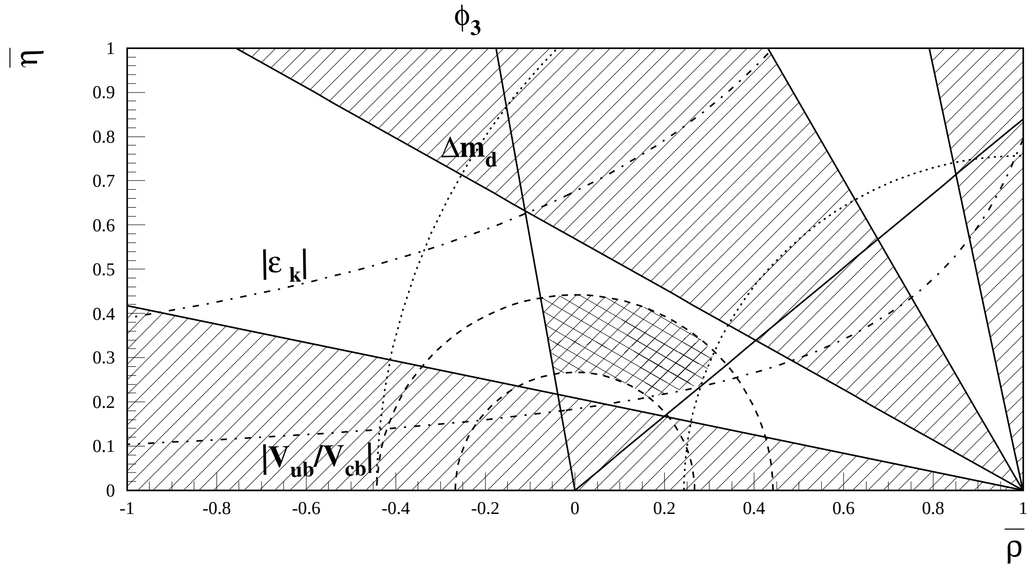

Figure 9.8: *The expected new constraints at the integrated luminosity of 100fb^{-1}. The double hatched area is constrained with new measurement of $|V_{ub}/V_{cb}|$ and ϕ_3. The hatched area is the region where new physics can be observed.*

Following are the descriptions about the variation of ϕ_1 of the unitarity triangle by major new physics beyond the Standard Model.

Multi Higgs doublets

The Higgs sector of the Standard Model, which has a single Higgs doublet, has not yet been experimentally tested. The possibility of extended Higgs sector is certainly consistent with experimental data[99]. The simplest extensions are models with several Higgs doublets.

The B^0-$\bar{B}^0$ mixing amplitude receives extra contributions from box diagrams, where one or two of the W's are replaced by the charged Higgs. When imposing Natural Flavor Conservation(NFC)[100], within the framework of multi-Higgs-doublet model, CP violation could arise in charged scalar exchange if there are at least three Higgs doublets[4]. CP violation from charged scalar exchange, however, may have a small effect on CP asymmetries in neutral B decays, at most 0.02 shift in the measured CP asymmetry in $B \to J/\psi K_S$[101].

The requirement of spontaneous CP violation in Higgs sector forces $a_{f_{CP}}$=0[102]. In this case, CP non-invariance arises solely from charged scalar exchange. However, it seems that with the new limits on scalar masses from LEP, this class of models is phenomenologically excluded.

Extra quark

Although from accelerator experiments, the number of neutrinos lighter than $M_Z/2$ is limited to three, the SM have no reason to rule out the possibility of a fourth sequential generation with a very massive neutrino flavor. If there is a fourth generation, the unitarity triangle becomes a unitarity quadrangle. Since many of the constraints on the KM elements arise from the assumed unitarity of the 3×3 matrix, a value of CP asymmetry inconsistent with allowed region in three generation case may be indicated. Since new 4×4 matrix is parameterized by 6 angles and 3 phases, the evaluation is more complicated compared with three generation case[97]. As already mentioned in previous section, ϕ_1 has a possibility to be significantly different value from the SM prediction.

Supersymmetry(SUSY)

There could be significant new contributions to B^0-$\bar{B}^0$ mixing from box diagrams with intermediate gluinos and squarks.

In the minimal Supersymmetry, only left-handed squarks contribute. The couplings are proportional to the elements of KM matrix and thus no new phases are introduced[103, 104]. CP asymmetry is not modified in minimal SUSY models. The effects in B^0-$\bar{B}^0$ mixing will change only the estimation of $|V_{tb}^* V_{td}|$. ΔM_B can increase by $\sim$ 20% of the Standard Model value[105].

However, in less restrictive SUSY models, there are contributions from box-diagrams with right-handed squarks as well. The mixing matrices are not related to KM-matrix and carry, in general, new phases. Some models predict the deviation of ϕ_1 of order 0.4 from the SM value[106].

To summarize, we have shown that some models beyond the SM predict the deviation of ϕ_1 from that expected by SM. According to SUSY (non-minimal) or extra generation quark model, ϕ_1 can have a significant difference and can be within the region of our sensitivity.

Chapter 10

Conclusion

The primary goal of the KEK B-factory experiment is to measure angles of the unitarity triangle and to perform the test of the Standard Model. The $B \to \text{charmonium} + K_S$ mode is expected to provide the best information to measure angle ϕ_1 with small theoretical uncertainty and a small experimental error. A simulation study was performed to estimate the sensitivity of $\sin 2\phi_1$ measurement for $B \to \text{charmonium} + K_S$ at the KEK B-factory experiment.

Since CP asymmetry appears in the time-independent decay rate of B mesons, silicon vertex detector is the most crucial part of the BELLE detector. The sensitivity to CP violation is directly affected by the vertex resolution. In order to confirm the correctness of the detector simulation and the performance of silicon vertex detector, the testbeam experiment was performed. For the silicon strip detector prototype, the intrinsic spatial resolution was measured with large incident angles to produce a similar condition to BELLE. The result was well consistent to the simulation expectation.

In order to evaluate the vertex resolution of B decays with BELLE SVD, we performed simulation study for $B \to J/\psi K_S$. Using double Gaussian resolution function, we obtained the vertex resolution of Δz of 83.6μm for a narrower component with a fraction of 0.82, which is much smaller than the decay length of B meson in z. Taking the effect of the wider component into account, the dilution factor in $\sin 2\phi_1$ measurement turns out to be compatible with the case of a single Gaussian response function with σ=100μm. Thus we conclude that BELLE SVD has the vertex resolution which is good enough to measure CP asymmetry.

We also performed simulation study to measure $\sin 2\phi_1$. We treated events generated with Monte Carlo simulation as experimental data. We developed the method to measure the parameters such as the wrong tagging probability, the response function of vertex reconstruction and the background function from only experimental data in order to avoid the systematic errors from Monte Carlo information in the real experiment. We obtained 677 events for $B \to J/\psi K_S$, 181 for $B \to \psi(2S)K_S$, 124 for $B \to \chi_{c1}K_S$ and 273 for $B \to \eta_c K_S$ with the integrated luminosity of 100fb^{-1}. The number of background was small and was estimated to be 124 ± 17 events. We calculated the value of $\sin 2\phi_1$ and its statistical error with fitting the proper time distribution of B meson decays. We also estimated the systematic error. For the input value of $\sin 2\phi_1$= 0.60, we obtained the results for the integrated luminosity of 100 fb^{-1} as follows;

$$\begin{aligned}
\sin 2\phi_1 &= 0.635^{+0.102}_{-0.105}(stat.) \pm 0.046(sys.) \quad (B \to J/\psi K_S), \\
&= 0.617^{+0.209}_{-0.221}(stat.)^{+0.069}_{-0.037}(sys.) \quad (B \to \psi(2S)K_S), \\
&= 0.181^{+0.274}_{-0.278}(stat.)^{+0.093}_{-0.043}(sys.) \quad (B \to \chi_{c1}K_S), \\
&= 0.866^{+0.179}_{-0.192}(stat.)^{+0.076}_{-0.057}(sys.) \quad (B \to \eta_c K_S).
\end{aligned}$$

By combining all charmonium modes, we obtain;

$$\sin 2\phi_1 \quad = \quad 0.632^{+0.080}_{-0.081}(stat.)^{+0.047}_{-0.044}(sys.).$$

The systematic error was reduced to the level lower than the statistical error. The dominant systematic error came from the estimation of the response function of vertex reconstruction for $B \to J/\psi K_S$ and the inaccuracy of background function for the other modes.

With the result of simulation, it is found that we can observe CP asymmetry with 3σ significance if the value of $\sin 2\phi_1$ is larger than 0.28 with 100fb^{-1}, which covers the entire allowed region with the present indirect experimental results. Thus assuming the SM and the present allowed region, it is guaranteed that the BELLE experiment observes CP violation in B decays.

Appendix A

Precision Alignment in Testbeam Setup

In the testbeam setup, we have aligned the position of the sample SSD using data of the beam tracks. There are three degrees of freedom of the sample SSD location. Figure A.1 shows these degrees of freedom, *i.e.* (1) a rotation angle(=α), (2) a rotation about z-axis, (3) a displacement in z-direction. To obtain the exact position, we put a "reference plane" near the sample SSD and corrected the difference between the reference plane and the sample SSD in the following way.

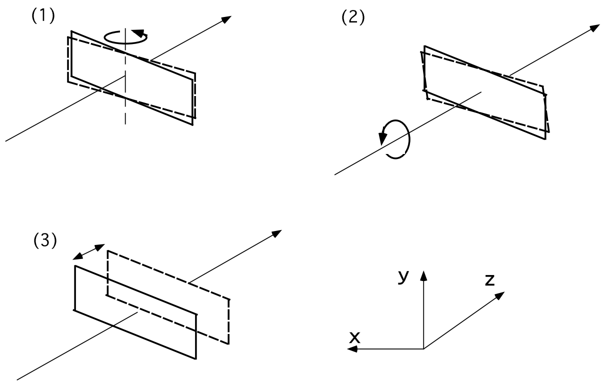

Figure A.1: *Alignment of the sample SSD in space*

First of all, we obtained the rotation angle, α, of the sample SSD about y-axis(Figure A.2). The reference plane was located on the center of the telescope parallel to the reference SSDs. This is the expected position of the sample SSD in case of $\alpha = 0°$. The hitpoint of the reconstructed track on the reference plane, X_r, was then calculated. Figure A.2 shows the correlation between X_r and the position on the sample SSD, X_{SSD}. Each point on the reference plane corresponds to each point on the sample SSD. We obtained the rotation angle(= incident angle), α, of the sample SSD about y-axis by a linear fitting to this plot, since the slope is related to α as below;

$$X_{sampleSSD} = \frac{X_r}{\cos\alpha} + constant. \tag{A.1}$$

Next, we corrected the small rotation, $\delta\phi$, about z-axis due to imperfection of our alignment.

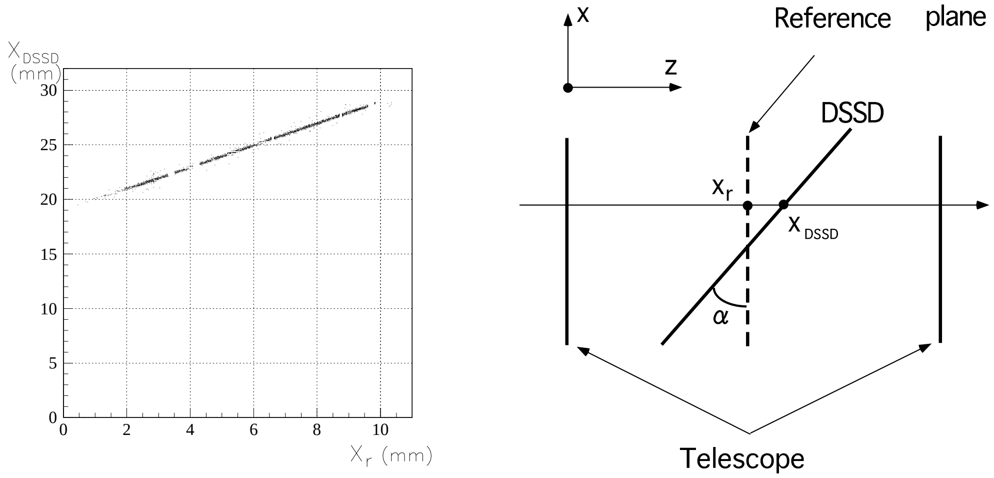

Figure A.2: *Alignment of the sample SSD in the rotation about y-axis.*

The reference plane was located nearer to the sample SSD with using equation (A.1). The residual in x-direction changes as a function of y_r, y position on the reference plane, because of the rotation, $\delta\phi$. Figure A.3 shows the correlation between y_r and the residual on x-direction. By a linear fitting to this figure, we obtained $\delta\phi$ with the following equation;

$$(Residual) = \tan\delta\phi \cdot y_r + constant. \tag{A.2}$$

Finally, we obtained the position of the sample SSD in z-direction(Figure A.4). The reference plane was located nearer to the sample SSD with using equation (A.1) and (A.2). The residual in x-direction changes as a function of the angle of the beam track, which is proportional to the difference between hitpoints upstream and downstream, X_{diff}, as illustrated in Figure A.4. Figure A.4 shows the correlation between X_{diff} and the residual on x-direction. We obtained the difference in z-direction, Δz, of sample SSD with the following equation;

$$(Residual) = \frac{\Delta z}{L} \cdot X_{diff} + constant \tag{A.3}$$

where L is the distance of 90mm between reference SSD upstream and downstream.

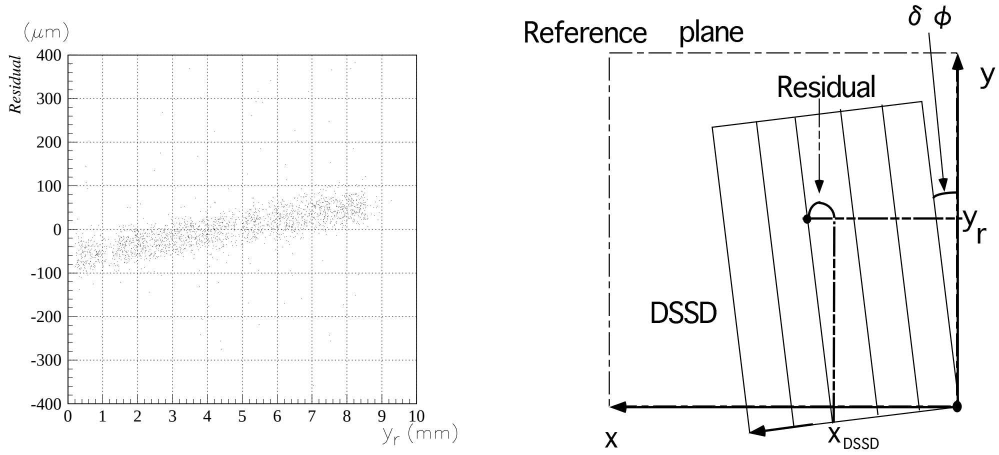

Figure A.3: *Alignment of the small rotation angle of sample SSD about z-axis due to imperfection of alignment.*

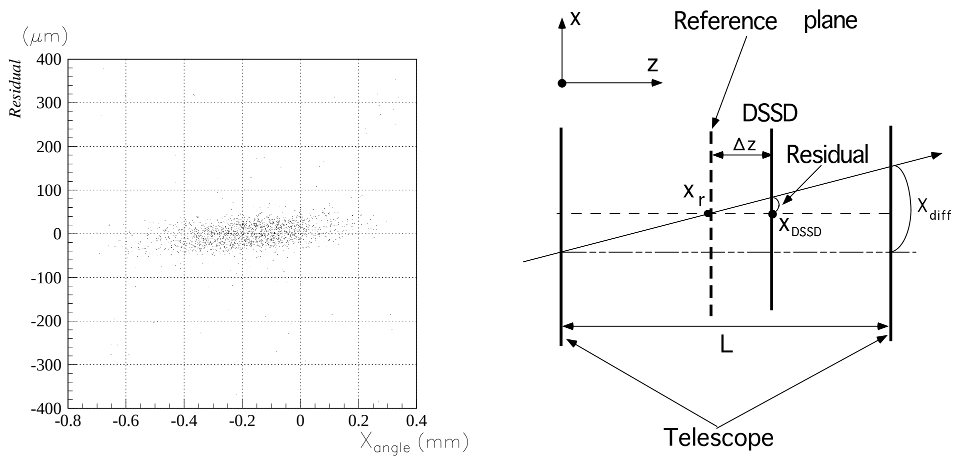

Figure A.4: *Alignment of sample SSD in z-direction.*

Appendix B

Track Finder

In this chapter, we explain a method to find the tracks of charged particles in CDC.

The measurement of momentum and sign of the charge of a charged particle is performed by reconstructing its trajectory in CDC. The trajectory of charged particle form the helical path in the magnetic field. Reconstructed tracks are expressed with five helix parameters(dr, ϕ, ρ, dz, θ). The definition of these parameters are shown in Figure B.1.

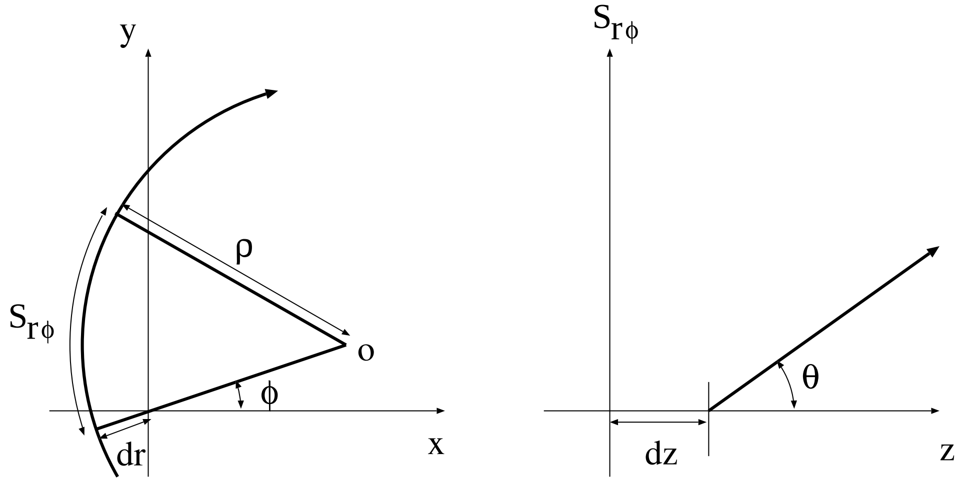

Figure B.1: *Helix parameters. The charged tracks are expressed with five helix parameters, dr, ϕ, ρ, dz and θ. In the figure $S_{r\phi}$ is the arc length.*

The track reconstruction in 3-dimension, which amounts to determination of five helix parameters, is performed in the following order.

1. Track reconstruction in $r - \phi$ plane.
   (a) The drift distance from a wire in each hit cell is reconstructed with TDC data. Each hit form a circle around the wire in r-ϕ plane.
   (b) Hit points are translated to a conformal plane defined with the coordinate (u, v) as

follows;

$$u = \frac{-x}{x^2+y^2}, \qquad v = \frac{y}{x^2+y^2}.$$

The circle, which passes near the origin point, will be mapped to a straight line with this translation (see Figure B.2 and [85]).

(c) Taking a seed point from outer side in the conformal plane, a histogram of number of hit is made around the seed point. The horizontal axis of the histogram is the azimuthal direction around seed point and divided to bins with finite width. (Figure B.3)

(d) A seed track is made with hit points which belong to a bin of the largest number.

(e) Then hits which have smaller distance than threshold[1] from the seed track are collected. The track are fitted using all collected hits with a circle in r-ϕ plane. Parameters ρ, ϕ and dr are determined by this fitting results.

2. Track reconstruction in z-$S_{r\phi}$ plane, where $S_{r\phi}$ is the length of arc along the track in r-ϕ plane.

   (a) Stereo wire hits which are associated with track candidates reconstructed in r-ϕ plane are collected.(Figure B.4(a))

   (b) The position of hits in z and $S_{r\phi}$ is calculated with cross point of stereo wire and r-ϕ track. B.4(b))

   (c) A seed track is reconstructed assuming the track is straight line in $z - S_{r\phi}$ plane (Figure B.4(c)). Then hits on stereo wire which have smaller distance than threshold from the seed track are collected.

3. The track was fitted using all collected hits, axial and stereo wire hits, with helix trajectory in 3 dimension. All helix parameters are determined by this fitting results.

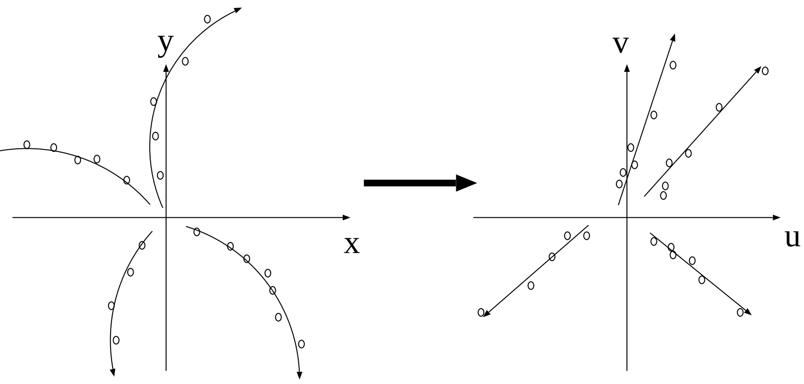

Figure B.2: *Conformal translation. The circle which through the origin point is mapped to a straight line.*

[1]Threshold is 10 times of the error of reconstructed hit position.

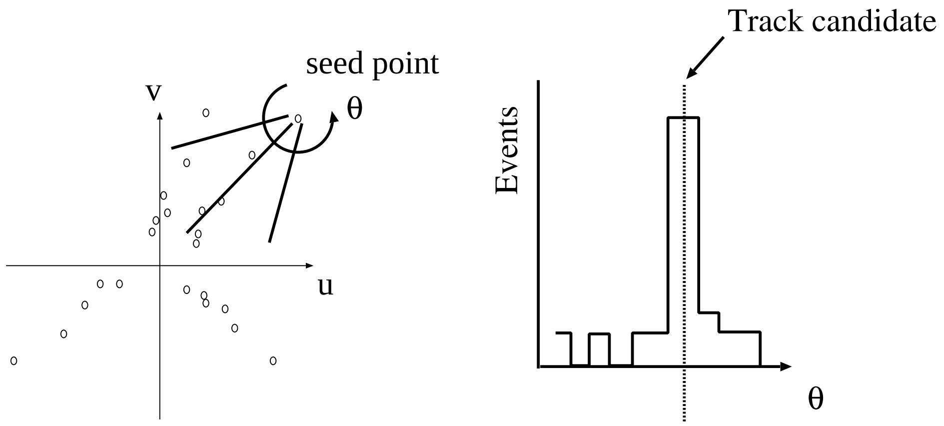

Figure B.3: *In order to make a seed track, the histogram was made around a seed point in conformal plane. The bin which has the largest number of hits is taken as a seed track.*

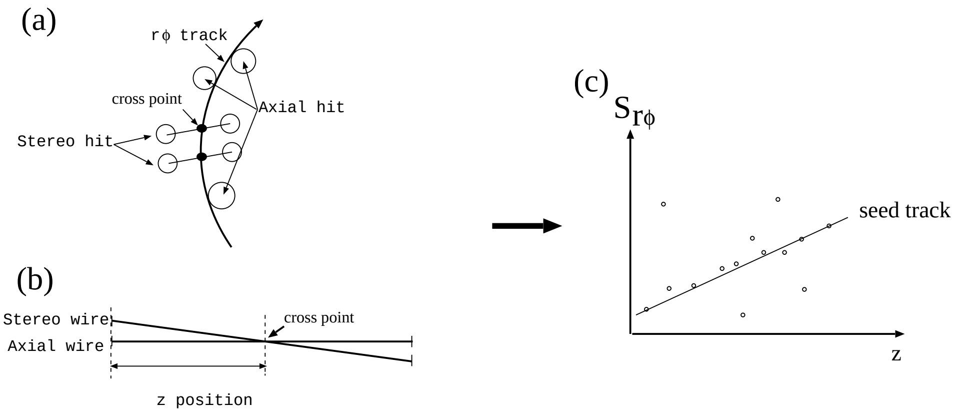

Figure B.4: *Reconstruction of track in z-$S_{r\phi}$ plane. (a) Stereo wire hits which are associated with the track candidate reconstructed in r-ϕ plane are collected. (b)The position of hits in z is calculated with cross point of stereo wire and r-ϕ track. (c) A seed track is reconstructed assuming the track is straight line in $z - S_{r\phi}$ plane.*

Appendix C

Reconstruction of $B \to \psi(2S)K_S$, $B \to \chi_{c1}K_S$ and $B \to \eta_c K_S$

In this chapter, reconstruction of B candidates is described for $B \to \psi(2S)K_S$, $B \to \chi_{c1}K_S$ and $B \to \eta_c K_S$. We also describe cluster finding methods in ECL and particle identification for charged particles.

C.1 Candidate reconstruction

C.1.1 Clustering in ECL

Since an electromagnetic shower made by photons or charged particles generally spreads over several crystals, a clustering algorithm is necessary to obtain the shower energy and its incident position.

A cluster is a group of connected crystals with energy deposit greater than a threshold(5MeV/c^2). The procedure to find all possible clusters are as follows[82, 107].

1. First, we find the first seed by choosing a crystal with the highest energy deposit from all hit crystals. Neighboring crystals are considered as part of the cluster attached to the seed crystal. The seed and its neighboring crystals are removed from candidates of the next seed crystal.

2. Iterating this procedure until no candidates of seed crystal remain(All crystals which have larger energy than threshold are regarded as seed or its neighboring crystals).

3. Two quantities, $E_{5\times5}$ and $E^{excl}_{5\times5}$, are calculated for each seed crystal where $E_{5\times5}$ is energy sum of 5×5 crystals around the seed. $E^{excl}_{5\times5}$ is the same quantity but excluding the crystals whose energies are shared by the two seed crystals.

4. If the ratio, $E^{excl}_{5\times5}/E_{5\times5}$, exceeds a threshold value of 0.95, it is identified as a cluster. If not, it is regarded as part of other clusters and is rejected.

5. The cluster energy is calculated with 5×5 crystals.

The cluster reconstructed with this algorithm is a candidate of photon. If the cluster is not matched to an intersection point of a charged track on ECL within 5.5cm, this cluster is identified as a photon.

The energy resolution of ECL for γ has been studied with our GEANT-based simulation and clustering software[50]. The energy dependence of the resolution is

$$\sigma_{E_\gamma}/E_\gamma = \frac{0.73\%}{\sqrt{E_\gamma(GeV)}} \oplus 2.1\%, \tag{C.1}$$

for the case in which all inner detectors are included. Here "$\oplus$" means quadruple sum. This results are consistent with that measured with a photon beam with BELLE ECL prototype[55].

C.1.2 Particle Identification

We need to identify electrons and muons to reconstruct J/ψ and $\psi(2S)$, and pions and kaons to reconstruct η_c and K_S. Identification of electrons, muons and kaons are also required for flavor tagging.

For electrons, pions and kaons, particle identification is performed combining the particle probability calculated from CDC, ACC, TOF and ECL. The calculation of probability of a track being a particular particle type $i(=e,\pi,K)$ from each sub detector, $CDC\_pid(i)$, $ACC\_pid(i)$, $TOF\_pid(i)$ and $ECL\_pid(i)$, were described in Section 5.3.5. The probability combined, cmb_pid(i), is calculated as:

$$cmb\_pid(i) = CDC\_pid(i) \times ACC\_pid(i) \times TOF\_pid(i) \times ECL\_pid(i). \tag{C.2}$$

Muons were identified with KLM only. PID was performed in the following order.

1. A track tagged by KLM is identified as μ
2. else if *cmb_pid(e)/pid_sum* $\geq$ electron threshold(=0.8), identify it as e
3. else if *cmb_pid(K)/pid_sum* $\geq$ kaon threshold(=0.8), identify it as K
4. else identified as π.

where *"pid_sum"* is defined as follows:

$$pid\_sum = cmb\_pid(e) + cmb\_pid(\pi) + cmb\_pid(K)$$

Leptons from J/ψ and $\psi(2S)$ have high momentum. The lepton used for flavor tagging was required to have high momentum at the Υ(4S) rest frame. In the momentum region higher than 1.2GeV, identification efficiency for muon and electron were 77.8% and 96.8%, respectively. Since pions and kaons from η_c have a momentum lower than 1GeV/c, TOF and CDC(dE/dx) are effective to separate them. The identification efficiency for kaon was about 80.0%. The probability for misidentifying pion as kaon was 1.5%.

C.1.3 Reconstruction of ψ(2S) candidate.

$\psi(2S) \to l^+l^-$ mode

The $\psi(2S)$ reconstruction of the decays to two leptons, $\psi(2S) \to\mu^+\mu^-$and $\psi(2S) \to e^+e^-$, follows the procedure outlined for J/ψ. Resolution of invariant mass distribution of $\psi(2S)$ is about 10MeV(Figure C.1).

Candidates are selected with the criteria:

$$-0.050 < M_{\mu^+\mu^-} - M_{\psi(2S)} < +0.050 GeV.$$
$$-0.150 < M_{e^+e^-} - M_{\psi(2S)} < +0.050 GeV.$$

The reconstruction efficiency for $\psi(2S)$ is 74.6% for $\mu^+\mu^-$and 61.3% for e^+e^-.

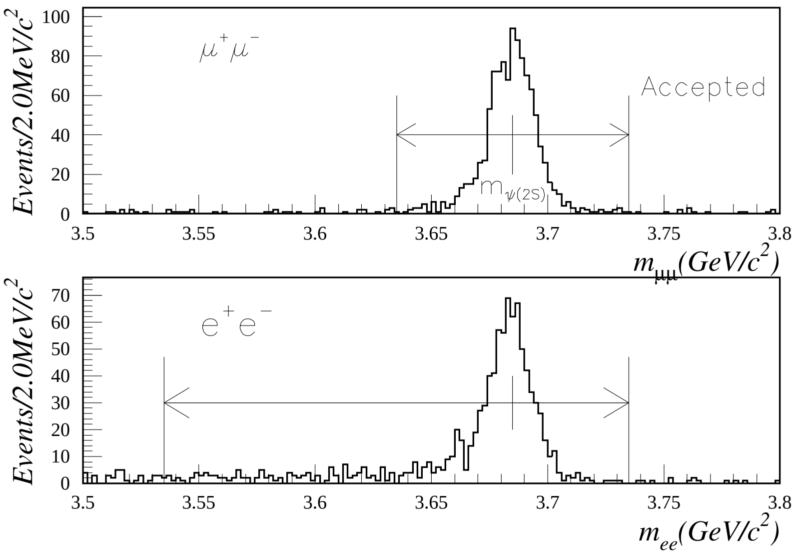

Figure C.1: *Invariant mass distribution of $\psi(2S)$ in $B \to \psi(2S)K_S$, $\psi(2S) \to \mu^+\mu^-$ or e^+e^- MC.*

$\psi(2S) \to J/\psi\pi^+\pi^-$ mode

In order to reconstruct $\psi(2S)$ decaying into $J/\psi\pi^+\pi^-$, J/ψ candidates were selected with wider mass criteria than that for $B \to J/\psi K_S$. We didn't require any particle identification for the pions to have higher reconstruction efficiency for $\psi(2S)$. $\psi(2S)$ were reconstructed through these J/ψ and two tracks which have opposite charge assuming the nominal J/ψ and pion mass.

The pions from $\psi(2S)$ have very low momenta($\sim$ 200MeV/c) and tracking efficiency should be worse($\sim$80%). The momentum distribution of pion from $\psi(2S)$ is shown in Figure C.2. To keep the reconstruction efficiency, we have loosed the criteria of invariant mass of $\psi(2S)$. To reduce the number of tracks misreconstructed or produced by decay in flight, the pions were required to have impact parameter[1] of d$r \leq$ 5mm and d$z \leq$ 5cm.

$$-0.030 < M_{\mu^+\mu^-} - M_{J/\psi} < +0.030 GeV.$$
$$-0.090 < M_{e^+e^-} - M_{J/\psi} < +0.030 GeV.$$

[1]Impact parameter is defined as the distance of particle helix to the origin point(0,0,0). The distance in r-ϕ and z are dr and dz which are defined in Section 6.1.1.

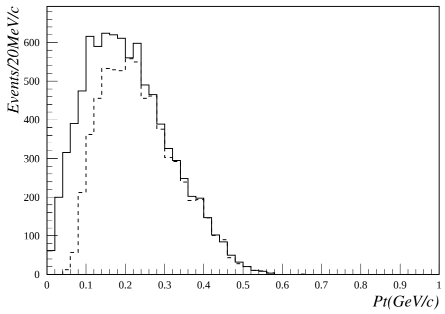

Figure C.2: *Pion Momentum distribution from ψ(2S) for $B \to \psi(2S)K_S$ MC. Only the events where J/ψ from $\psi(2S)$ was reconstructed are shown in order to avoid the effect of acceptance factor.*

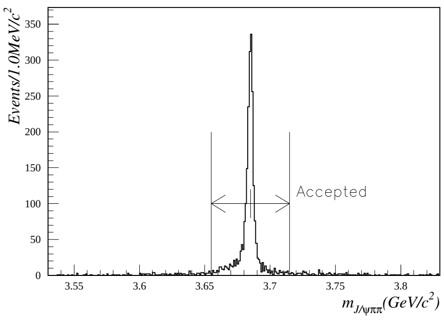

Figure C.3: *Invariant mass distribution of $\psi(2S)$ for $B \to \psi(2S)K_S$, $\psi(2S) \to J/\psi\pi^+\pi^-$ MC.*

$$-0.030 < M_{J/\psi\pi^+\pi^-} - M_{\psi(2S)} < +0.030 GeV.$$

The reconstruction efficiency of $\psi(2S)$ is 31.2% for $\mu^+\mu^-$and 25.8% for e^+e^-.

C.1.4 Reconstruction of χ_{c1} candidate.

χ_{c1} were reconstructed through its decays to $\gamma J/\psi$. J/ψ was selected with the wider mass window than that for $B \to J/\psi K_S$. The reconstructed J/ψ was assumed to have the nominal J/ψ mass. The largest background for the χ_{c1} signal is due to random combination of γ from $\pi^0 \to \gamma\gamma$ associated with correctly reconstructed J/ψ from B meson decays. If γ candidate forms an invariant mass within +10,-20MeV/c^2 of the known π^0 mass when combined with any other γ in the event, it is rejected. If all γ were used for this suppression, the signal γ was occasionally vetoed when it was combined with a low energy γ from uncorrelated π^0. To reduce this effect, γ candidate was required to have at least 150 MeV/c^2. This cut rejects few signal γ. The energy distributions of γ from various sources were shown in Figure C.4. Figure C.5 shows invariant mass with all combination of γ above the threshold.

The invariant mass distribution of χ_{c1} is shown in Figure C.6. The peak of this distribution is slightly shifted from nominal χ_{c1} mass. This shift was due to the correction of a low reconstructed mass of J/ψ with e^+e^- to the nominal J/ψ mass.

The mass resolution of χ_{c1} is degraded by the energy resolution and the production vertex uncertainty for gamma. We have obtained about 10MeV for $J/\psi \to \mu^+\mu^-$and e^+e^-modes. The candidate was required to have the criteria as

$$-0.030 < M_{\mu^+\mu^-} - M_{J/\psi} < +0.030 GeV,$$
$$-0.090 < M_{e^+e^-} - M_{J/\psi} < +0.030 GeV,$$
$$-0.040 < M_{J/\psi\gamma} - M_{\chi_{c1}} < +0.020 GeV.$$

The reconstruction efficiency of χ_{c1} is 46.3% for $\mu^+\mu^-$and 37.7% for e^+e^-.

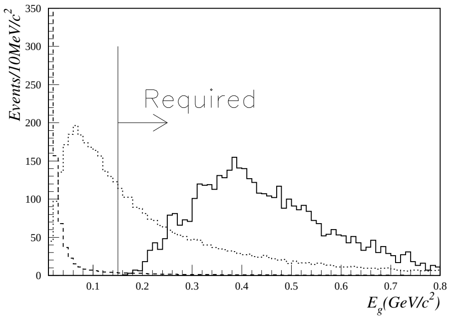

Figure C.4: *Energy distribution of γ. Dashed line is all γ in $B^0\bar{B}^0$ generic MC events. Dotted line is γ from π^0 in $B^0\bar{B}^0$ generic MC events. Solid line is γ from χ_{c1} in $B \to \chi_{c1}K_S$ MC.*

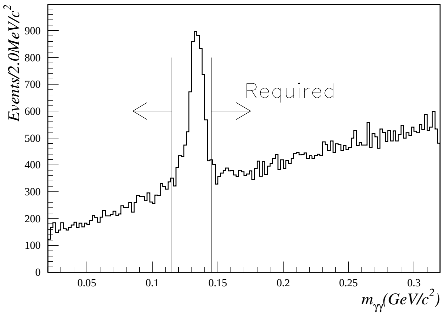

Figure C.5: *π^0 mass distribution in $B^0\bar{B}^0$ generic MC event.*

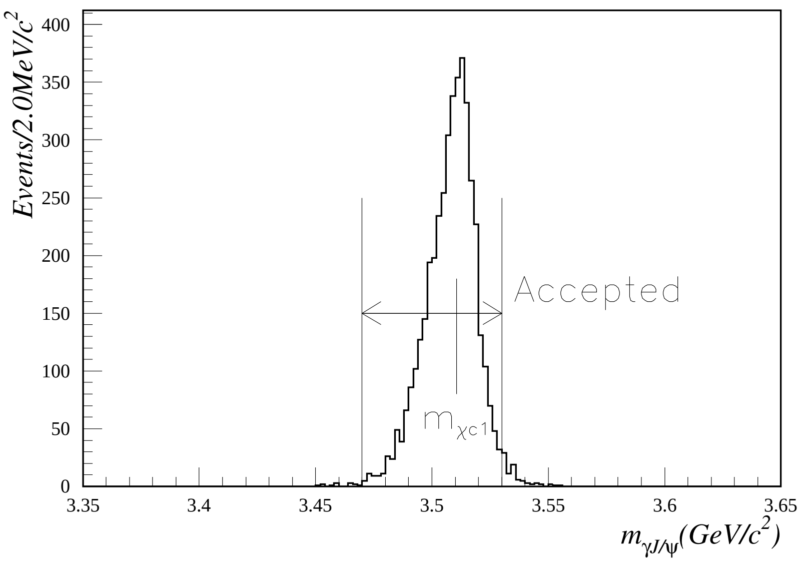

Figure C.6: *Invariant mass distribution of χ_{c1} in $B \to \chi_{c1}K_S$ MC.*

C.1.5 Reconstruction of η_c candidate.

The η_c candidate was reconstructed through its decays to four charged hadrons, $K^{\pm}$ and $\pi^{\pm}$. To reduce the combinatorial backgrounds, we performed cuts on the impact parameters: dr $\leq$5mm and dz $\leq$5cm(Figure C.7). These cut parameters were determined from the beam bunch size and the flight length of B mesons. This requirement also rejects the tracks which were from decay in flight as well as misreconstructed tracks.

We have used three decay modes, $\eta_c \to K^+K^-\pi^+\pi^-$, $\eta_c \to 2(\pi^+\pi^-)$ and $\eta_c \to 2(K^+K^-)$. We reconstruct η_c with daughter particles identified as specific particle kind except $\eta_c \to 2(K^+K^-)$ mode. In order to improve the reconstruction efficiency for $\eta_c \to 2(K^+K^-)$, the η_c candidates were also reconstructed with three identified K and a not-identified track (=π), where all tracks are assumed to have nominal kaon mass.

Invariant mass of η_c was required to be within about 3σ around the nominal mass, where σ is the width obtained by fitting the distribution with the Gaussian function. This width was wider than resolution because of the finite mass width of η_c. Figure C.8 shows the distribution of η_c invariant mass. We have required to have the invariant mass to be

$$0.040 \leq |M_{\eta_c} - M_{K^+K^-\pi^+\pi^-}| \leq 0.030GeV,$$
$$0.040 \leq |M_{\eta_c} - M_{2(\pi^+\pi^-)}| \leq 0.030GeV,$$
$$0.050 \leq |M_{\eta_c} - M_{2(K^+K^-)}| \leq 0.030GeV.$$

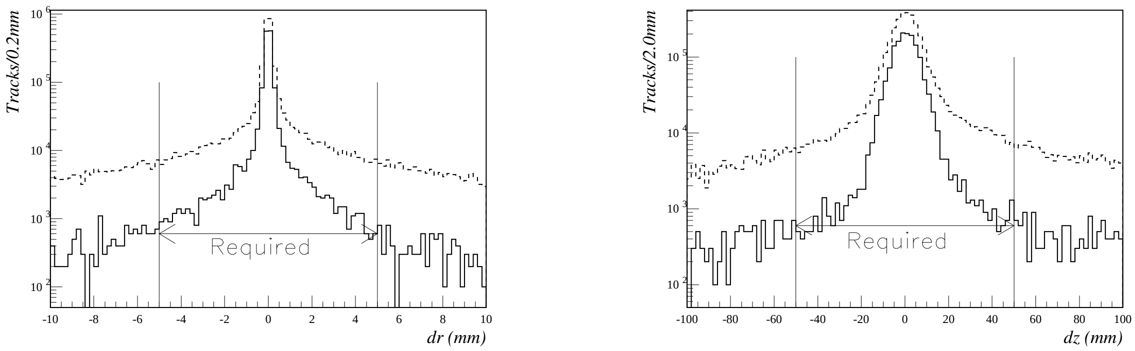

Figure C.7: *Impact parameter distribution of daughters of η_c candidates for $B \to \eta_c K_S$ MC. Solid line is track from the true η_c and dashed line is all tracks.*

C.1.6 Reconstruction of B^0 candidate.

The B^0 candidates were reconstructed with the combination of K_S and charmonium candidates. The reconstruction of K_S follows the same line of $B \to J/\psi K_S$. K_S, J/ψ, $\psi(2S)$ and χ_{c1}, candidates were assumed to have their nominal mass value. The mass of η_c was not constrained in order to take the wide mass width of η_c into account. The invariant mass and momentum at the $\Upsilon(4S)$ rest frame for all modes are shown in Figure C.9. The candidates were selected with the following criteria:

$$|M_{B^0} - M_{\psi(2S)K_S}| \quad < \quad 0.025GeV, (B \to \psi(2S)K_S)$$

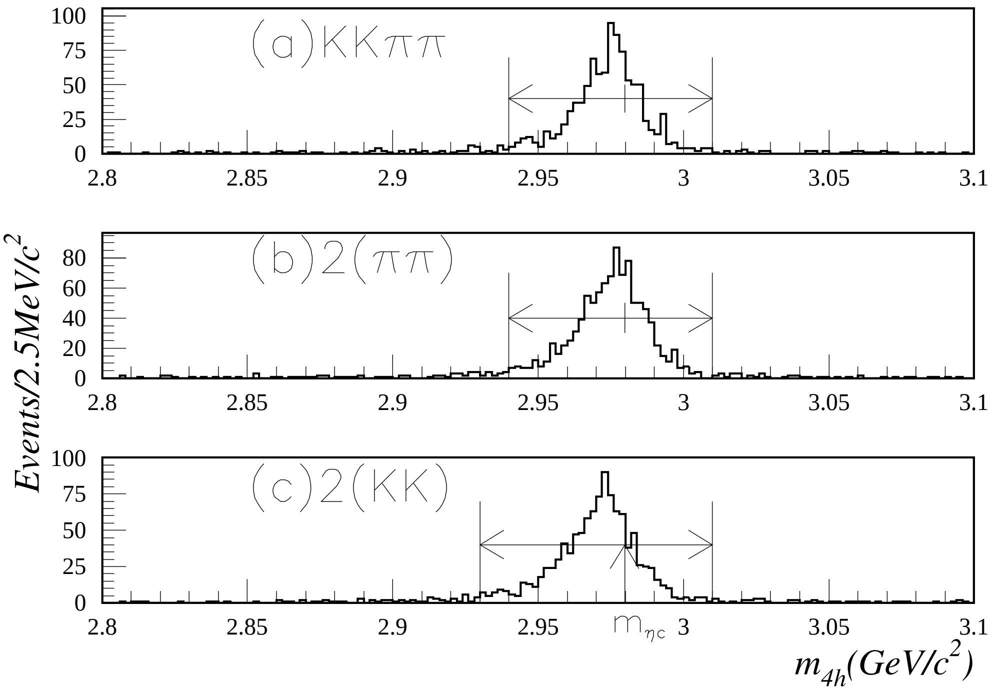

Figure C.8: *Invariant mass distribution of η_c in $B \to \eta_c K_S$ MC.*

$$
\begin{aligned}
|M_{B^0} - M_{\chi_{c1}K_S}| &< 0.030 GeV, (B \to \chi_{c1} K_S) \\
|M_{B^0} - M_{4h^\pm K_S}| &< 0.050 GeV, (B \to \eta_c K_S) \\
0.19 < P^*_{B^0} &< 0.47 GeV.
\end{aligned}
$$

Since the mass of charmonium and K_S were constrained except $B \to \eta_c K_S$, the mass resolutions of B meson depend on the mass of charmonium.

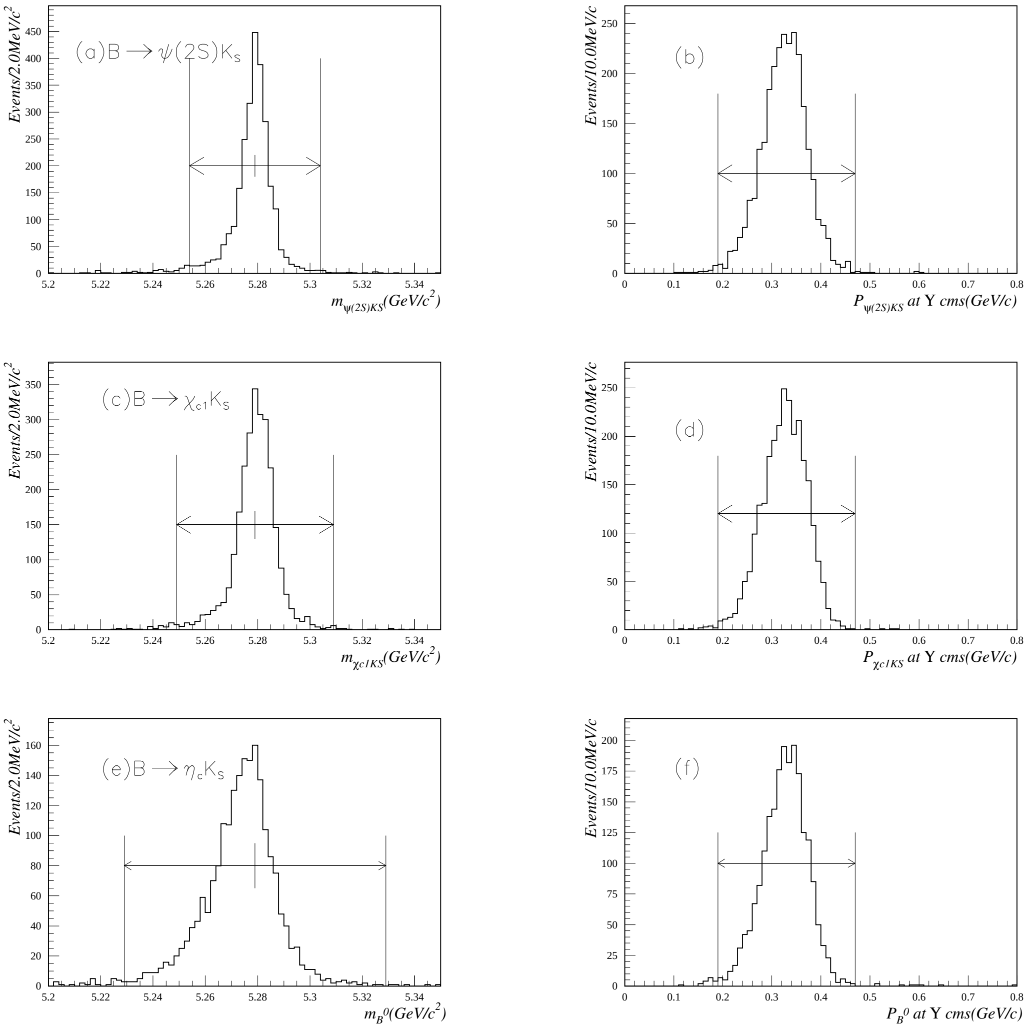

Figure C.9: *(a)(c)(e) Invariant mass distributions and (b)(d)(f) Momentum at $\Upsilon(4S)$ rest frame of the reconstructed B in MC of the following channels: (a)(b) $B \to \psi(2S) K_S$, (c)(d) $B \to \chi_{c1} K_S$ and (e)(f) $B \to \eta_c K_S$.*

C.2 Mass and vertex constrained fit

For $B \to \eta_c K_S$, the mass of η_c was not constrained because of its larger width. In order to obtain the better mass resolution of B meson for this mode, we further performed mass and vertex[1] constraint fit with FITVER[108], which was developed by DELPHI collaboration. FITVER reconstructs B_{CP} with helix parameters of daughter particles directly. The mass of η_c and K_S candidate were constrained to its nominal value taking its mass width into account. Three decay vertices, K_S, η_c and B_{CP}, were constrained. Fitting mass and vertex simultaneously, we could reduce background events. Figure C.10 shows the results of mass and vertex constrained fit for $B \to \eta_c K_S$. The resolution of B mass was improved. The following criteria were required:

$$\begin{aligned} |M_{B^0} - M_{Fit}| &< 0.025 GeV, \\ 0.24 &< P^*_{B^0 Fit} < 0.40 GeV/c, \end{aligned}$$

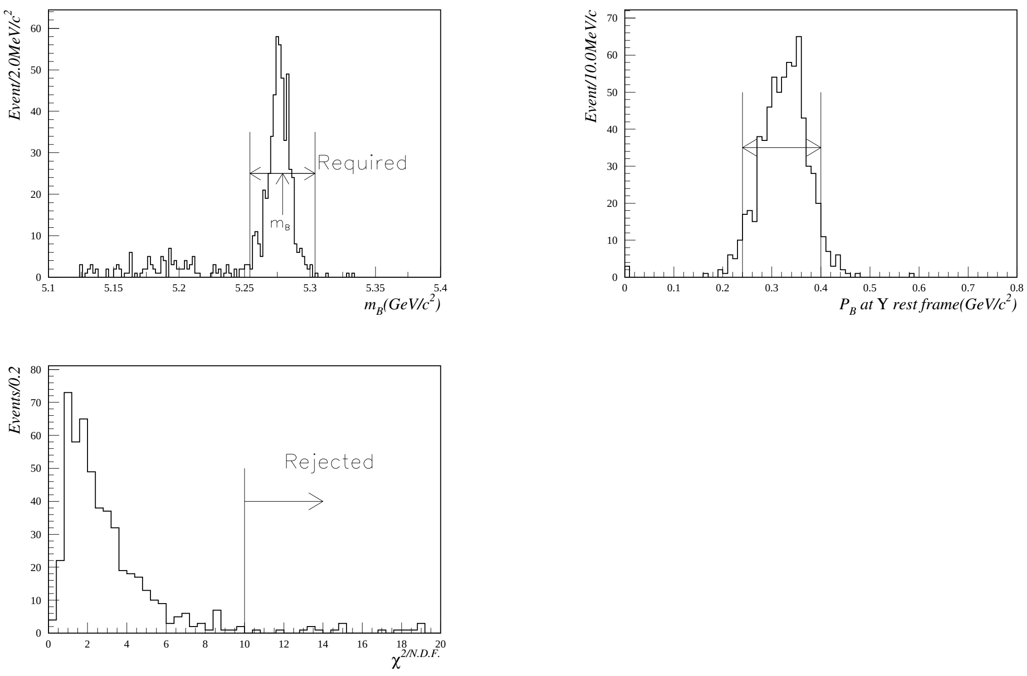

Figure C.10: *Fitting results of mass and vertex constraint fit in $B \to \eta_c K_S$ MC.*

C.3 Background Rejection

To reject a certain kind of background, simple event selections were performed.

[1]Except the case of K_S reconstruction, we have ignored the effect of the difference between production and closest point to beam axis of particles. This effect is serious for low momentum tracks as it's the case for η_c.

C.3.1 Fox-Wolfram parameter cut

Candidates of $B \to \psi(2S)K_S$ and $B \to \chi_{c1}K_S$, were selected with larger mass criteria than that of $B \to J/\psi K_S$ in order to improve the reconstruction efficiency. For $B \to \eta_c K_S$, backgrounds from continuum were not reduced with mass cut alone. To reduce the continuum background events for these modes, we have adopted a cut with Fox-Wolfram parameter[109]. First, we define the k-th Fox-Wolfram moment as:

$$H_k = \frac{1}{s}\sum_i^N \sum_j^N [|\vec{p_i}| \cdot |\vec{p_j}| P_k(\cos\phi_{ij})] \tag{C.3}$$

where N is the number of particles, s is the square of the center-of-mass energy, $P_k(\cos\phi_{ij})$ is the Legendre polynomial of order k and ϕ_{ij} is the angle between the vector momenta of the i and j particles. Then the Fox-Wolfram parameter R_2 is defined as H_2/H_0. R_2 is close to 1 for jetlike events and to 0 for spherical events. Figure C.11 shows the distribution of Fox-Wolfram parameter, R_2, for $B \to \psi(2S)K_S$, $B \to \eta_c K_S$ and continuum events. We rejected the events which had R_2 larger than 0.5 for $B \to \psi(2S)K_S$ and $B \to \chi_{c1}K_S$, and 0.38 for $B \to \eta_c K_S$. Since $B \to \eta_c K_S$ mode has more continuum background events, we set a smaller cut value than that of $B \to \psi(2S)K_S$ and $B \to \chi_{c1}K_S$.

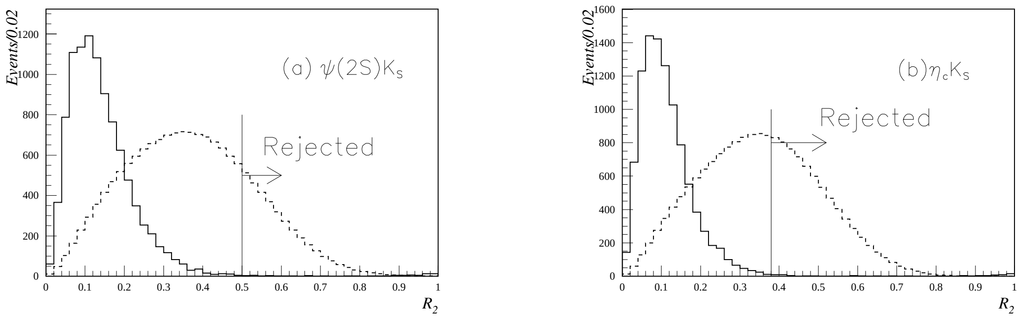

Figure C.11: *The distribution of Fox-Wolfram parameter R_2. Left: $B \to \psi(2S)K_S$, Right: $B \to \eta_c K_S$. Solid line is signal MC and dashed line is continuum MC events.*

C.3.2 Thrust angle cut

In order to remove the remaining continuum background for $B \to \eta_c K_S$, thrust angle cut was performed. The quantity called thrust[110], T, is defined as

$$T = max\left(\frac{\sum_i^N |\vec{P_i}\vec{n}|}{\sum_i^N |\vec{P_i}\ |}\right), \tag{C.4}$$

where $\vec{P_i}$ is the momentum vector of the i-th particle. The axis along the unit vector $\vec{n}$ is defined as the thrust axis. The definition is only valid in the c.m. frame. The thrust angle is chosen for each event so that the value T is maximized. Then we calculate the angle θ_T between the thrust axis of candidate B^0 mesons and that of the remaining charged and neutral particles in an event. Since the continuum $q\bar{q}$ events have a jetty structure whereas the $B^0\bar{B}^0$ events have

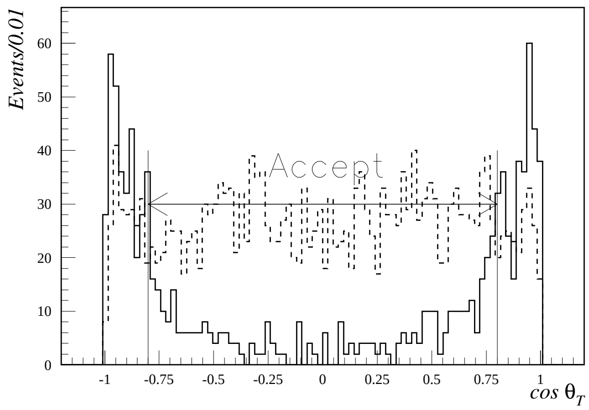

Figure C.12: *Thrust cut. The solid line is signal MC and dashed line is continuum MC events.*

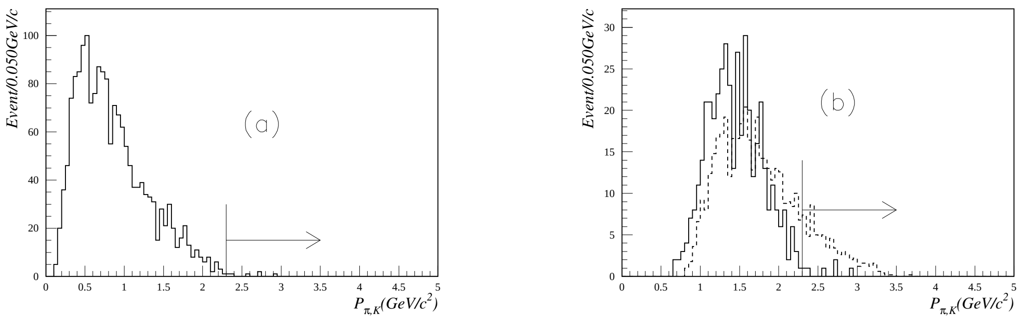

Figure C.13: *The distribution of momentum of (a) all daughters from η_c in $B \to \eta_c K_S$ MC. (b) The distribution of maximum momentum of daughters from η_c. Solid line is $B \to \eta_c K_S$ MC. Dotted line is continuum MC events.*

no axis correlation, the distribution of $\cos\theta_T$ is strongly peaked near $\cos\theta_T = \pm 1$ for $q\bar{q}$ events and nearly flat for signal events as shown in Figure C.12. We have required the candidate to have $\cos\theta_T < 0.9$.

C.3.3 Momentum distribution of π/K from η_c

The momentum of the η_c daughters was constrained kinematically. We can reduce fake η_c with checking the daughter momentum. Fig. C.13(a) shows the momentum distribution of η_c daughters for all signal modes. Fig.C.13(b) shows the distributions of the highest momenta among four η_c daughters for signal events and for the continuum background events, which survived the fiducial selection and the Fox-Wolfram cut. We rejected a η_c candidate if at least one of η_c daughters had momentum larger than 2.3 GeV/c. The cut with the η_c daughters' momenta reduced the continuum background events by 30% whereas the loss of signal events was only a few %.

Appendix D

Efficiency and background Analysis with MC

In this thesis, we treat the event generated by Monte Carlo simulation as real experimental data. In chapter 7 and 8, we called that "MC-data" and distinguish from usual Monte Carlo simulation.

We also generated independent Monte Carlo events for each signal mode($B \to J/\psi K_S$, $B \to \psi(2S)K_S$, $B \to \chi_{c1}K_S$ and $B \to \eta_c K_S$) and the background events. For each signal mode, 10^4 events are generated. background events were generated with the statistics corresponding to an integrated luminosity of 100fb^{-1}.

In this chapter, we describe the evaluation of the efficiency, the vertex resolution, the wrong tagging fraction and remaining background which are studied only with using generator information.

D.1 Efficiency for candidate reconstruction

In the reconstruction of K_S, charmonium and B candidate, we evaluated the reconstruction efficiencies for all signal modes. The reconstruction efficiencies and the fitting width of mass distribution with Gaussian are summarized in Table D.1. Since the mass of η_c has wide width and was not constrained, the mass width of B meson is larger than that of other three modes.

D.2 Flavor tagging

Table D.2 summarize the results of flavor tagging for all signal modes with the method described in Section 7.3.4.

D.3 Vertex resolution

For $B \to \psi(2S)K_S$ and $B \to \chi_{c1}K_S$, we used the same method as that for $B \to J/\psi K_S$ described in Section 6.

For $B \to \eta_c K_S$, we used the decay vertex of η_c as the decay vertex of B^0_{CP}. The vertex of η_c was reconstructed with using four daughter particles. In order to keep the high efficiency, we required at least three tracks matched SVD. The beam constraint was not adopted.

Table D.1: *B mesons reconstruction efficiency(ϵ) and mass resolution(ΔM; unit in MeV/c^2) at fiducial sample selection.*

	K_S	Charmonium		B	
$B \to J/\psi K_S$		$\mu^+\mu^-$	e^+e^-	$\mu^+\mu^-$	e^+e^-
	$\epsilon=$ 71.4%	69.0%	52.9%	48.3%	35.5%
	ΔM= 2.4	8.0	9.2	6.1	6.4
$B \to \psi(2S) K_S$		$\psi(2S) \to l^+l^-$		$\psi(2S) \to l^+l^-$	
		$\mu^+\mu^-$	e^+e^-	$\mu^+\mu^-$	e^+e^-
	66.4%	74.6%	61.3%	48.6%	37.9%
	2.2	10.0	10.0	4.2	4.7
		$\psi(2S) \to J/\psi\pi^+\pi^-$		$\psi(2S) \to J/\psi\pi^+\pi^-$	
		$\mu^+\mu^-$	e^+e^-	$\mu^+\mu^-$	e^+e^-
		31.2%	25.8%	20.8%	16.3%
		2.3	2.3	4.4	5.3
$B \to \chi_{c1} K_S$		$\mu^+\mu^-$	e^+e^-	$\mu^+\mu^-$	e^+e^-
	68.6%	46.3%	37.7%	28.9%	23.1%
	2.4	8.6	8.4	5.5	5.7
$B \to \eta_c K_S$		$\eta_c \to K^+K^-\pi^+\pi^-$		$\eta_c \to K^+K^-\pi^+\pi^-$	
		24.3%		17.7%	
		10.8		10.3	
		$\eta_c \to 2(\pi^+\pi^-)$		$\eta_c \to 2(\pi^+\pi^-)$	
		43.0%		30.6%	
	70.4	12.1		11.9	
	2.6	$\eta_c \to 2(K^+K^-)$		$\eta_c \to 2(K^+K^-)$	
		24.6%		17.5%	
		12.6		12.3	

Table D.2: *Results of flavor tagging.*

	Lepton tag			Kaon tag			Total			
	ϵ_l	ω_l	$\epsilon_{l,eff}$	ϵ_K	ω_l	$\epsilon_{K,eff}$	ϵ_t	ω_t	$\epsilon_{t,eff}$	$(1-2\omega)$
$J/\psi K_S$	0.116	0.045	0.096	0.336	0.134	0.180	0.413	0.109	0.253	0.782 ± 0.015
$\psi(2S) K_S$	0.111	0.074	0.081	0.329	0.135	0.176	0.404	0.118	0.236	0.764 ± 0.020
$\chi_{c1} K_S$	0.105	0.081	0.077	0.339	0.139	0.177	0.412	0.124	0.233	0.753 ± 0.020
$\eta_c K_S$	0.109	0.071	0.080	0.326	0.163	0.148	0.399	0.138	0.210	0.725 ± 0.025

Table D.3: *Results of vertex reconstruction. The fraction of narrow component is f_n. The mean and width are m_n (m_w) and σ_n (σ_w) for narrow (wide) component, respectively. The units for mean and width are μm.*

Mode	CP vertex					Tagging vertex					Δz vertex				
	f_n	m_n	σ_n	m_w	σ_w	f_n	m_n	σ_n	m_w	σ_w	f_n	m_n	σ_n	m_w	σ_w
$B \to J/\psi K_S$	0.89	0.24	44.3	-0.40	211.4	0.83	17.4	61.8	85.8	222.6	0.82	21.4	83.6	60.7	272.0
$B \to \psi(2S) K_S$	0.84	0.56	41.5	6.53	186.5	0.77	4.2	58.9	57.8	242.5	0.79	5.7	80.9	67.9	283.7
$B \to \chi_{c1} K_S$	0.91	-2.42	46.8	-30.5	245.6	0.88	19.0	73.6	94.3	241.2	0.89	25.4	93.1	84.6	343.1
$B \to \eta_c K_S$	0.91	3.17	50.6	0.46	151.3	0.78	9.2	50.7	48.2	157.4	0.82	11.0	82.8	47.5	212.0

We have fitted the residual distribution with double Gaussian function. The parameter of the fitted function obtained is summarized in Table D.3.

D.4 Background Estimation

In this section, we estimate the number of background events and categorize them. We also estimate the decay time of background for each category. A possible CP asymmetry of these background is briefly mentioned. At the integrated luminosity of 100fb^{-1}, the number of events of 1.15×10^8 for $\Upsilon(4S)$ and 2.8×10^8 for continuum will be generated. Since it takes too much time to generate the required number of events with the GEANT-based simulator(hereafter GSIM). We used the fast smearing simulator(hereafter FSIM) to generate large amount of background events.

D.4.1 Remaining background

For the background samples, we have adopted the same selection criteria as that developed for the signal selection. The number of remaining background events for 100fb^{-1} is summarized in Table D.4. In the table, "Others" include the mis-reconstruction of J/ψ with random leptons from semileptonic decay or misidentified leptons.

For $B \to J/\psi K_S$, $B \to \psi(2S) K_S$ and $B \to \chi_{c1} K_S$, continuum events are much reduced with the reconstruction of J/ψ or $\psi(2S)$ from two leptons. Therefore for these modes, the background is dominated by $B^0\bar{B}^0$ and B^+B^- events. In the case of $B \to \eta_c K_S$, however, continuum background events has a sizable contribution.

The backgrounds from continuum and B^+B^- have no CP asymmetry. These are uncorrelated backgrounds[1]. If J/ψ or $\psi(2S)$ was reconstructed correctly, some background events from

[1]Here we have ignored the small CP asymmetry of charged B mesons.

Table D.4: *The number of remained background*

	$B \to J/\psi K_S$		$B \to \psi(2S) K_S$		$B \to \chi_{c1} K_S$		$B \to \eta_c K_S$
$B^0\bar{B}^0$	$J/\psi K^{*0}$	2	$J/\psi K_S \pi^+\pi^-$	2	$J/\psi K_S \pi^0$	3	
			$\psi(2S) K_S \pi^0$	1	$J/\psi K^{*0}$	1	
					$\chi_{c2} K_S$	1	
	Others	0	5		1		36
B^+B^-	1		6		3		6
Continuum	2		6		0		44
Sum	5		20		9		86

B^0 to CP eigenstate shows CP asymmetry we can't ignore for $B \to J/\psi K_S$, $B \to \psi(2S) K_S$ and $B \to \chi_{c1} K_S$.

For $B \to \eta_c K_S$, almost of the remaining background events from$B^0\bar{B}^0$are not CP eigenstates. For example, the decay chain of such one background are shown in Figure D.1. Then all backgrounds remained for $B \to \eta_c K_S$ can be treated as uncorrelated.

D.4.2 Decay Time of Background

We define the decay time including the smearing due to the finite resolution. We fit Δz distribution with the following function:

$$f(\Delta z) = \frac{1}{2\tau_B c\beta\gamma} \exp(\frac{-|\Delta z|}{\tau_B c\beta\gamma}). \tag{D.1}$$

Figure D.2 shows the Δz distributions of (a) signal and (b) background from $\Upsilon(4S)$ for $B \to \chi_{c1} K_S$ mode. We obtained $\tau_B = 1.852$ps for signal and 2.085ps for background, respectively. Due to the finite resolution of vertex reconstruction, larger decay time was obtained even for the signal.

Figure D.2(c) shows the distribution of Δz of $B^0\bar{B}^0$ and B^+B^- backgrounds for $B \to \eta_c K_S$ mode. We obtained $\tau_B = 1.402$ps. The shorter life time is attributed to the fact that the combinatorial B_{CP}, which is the dominant source for this mode, is reconstructed with higher probability when the distance of two B mesons are smaller. Finally Figure D.2 is the Δz distribution of continuum background events for $B \to \eta_c K_S$, which gives us the smallest lifetime(0.622ps).

D.5 Summary

In Figure D.3, the invariant mass distributions of B_{CP} for all modes are shown at the integrated luminosity of 100fb^{-1}. Table D.5, D.6, D.7 and D.8 show the selection criteria and efficiencies for signal and the number of survived background events.

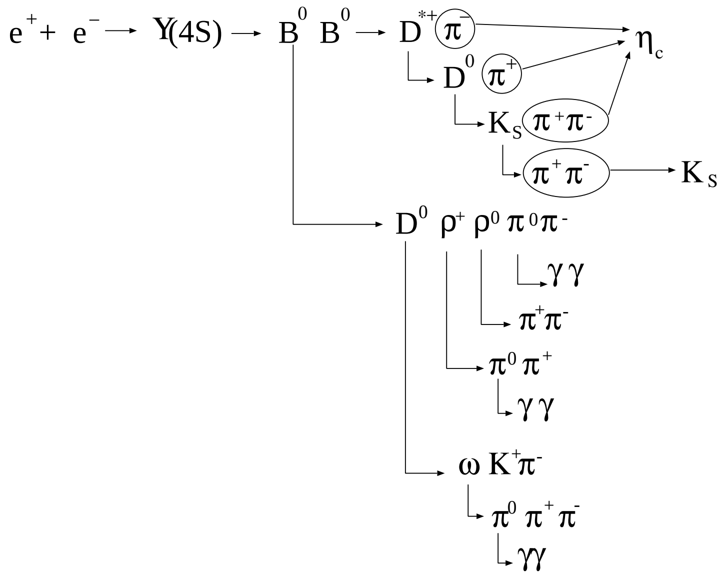

Figure D.1: An example of the $B^0\bar{B}^0$ background events in $B \to \eta_c K_S$ MC. The particles marked with circle were regarded as daughters from B^0 candidate. K_S are correctly reconstructed. All daughters consist B_{CP} were from one B meson.

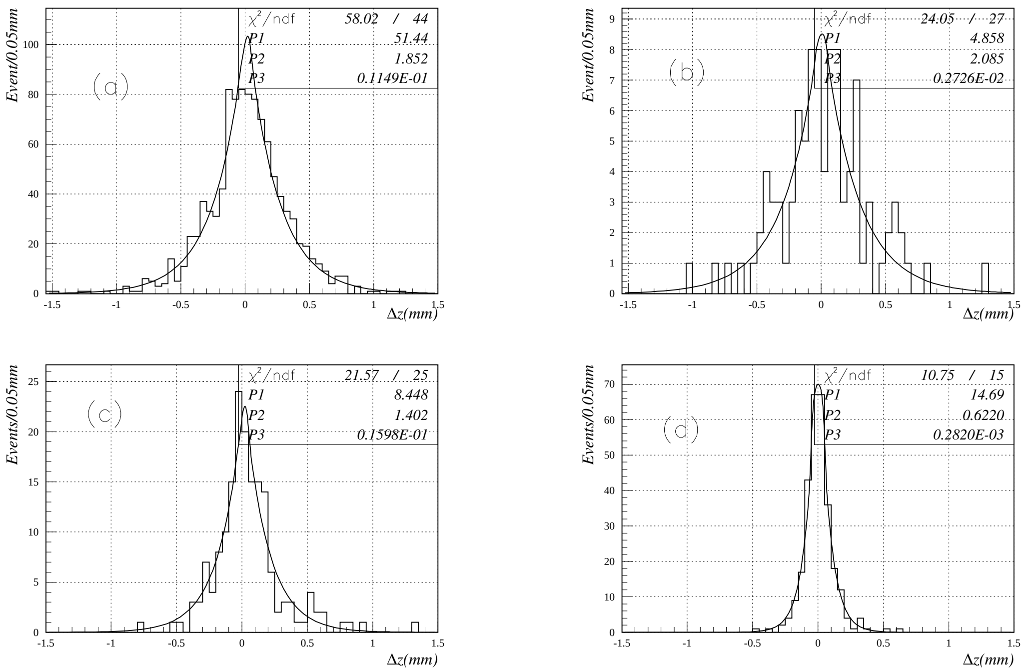

Figure D.2: *Δz distribution. (a) Signal mode in $B \to \chi_{c1} K_S$ MC. (b) $B^0\bar{B}^0$ and B^+B^- MC background for $B \to \chi_{c1} K_S$. (c) $B^0\bar{B}^0$ and B^+B^- MC background for $B \to \eta_c K_S$. (d) Continuum MC background for $B \to \eta_c K_S$.*

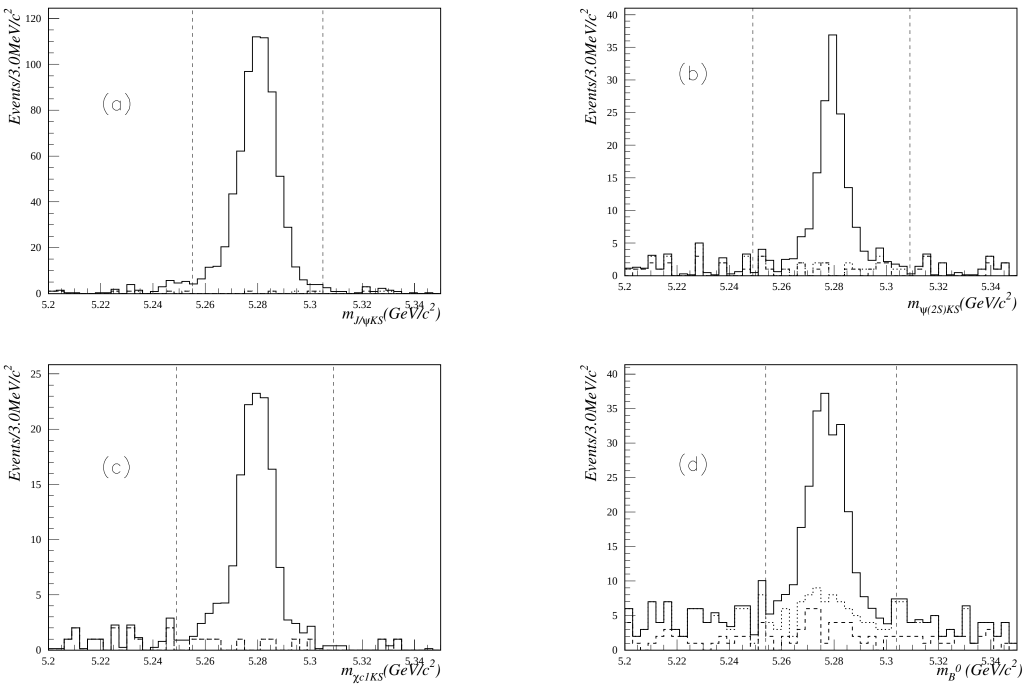

Figure D.3: *The mass distribution of B mesons with MC events for (a) $B \to J/\psi K_S$, (b) $B \to \psi(2S)K_S$, (c) $B \to \chi_{c1}K_S$ and (d) $B \to \eta_c K_S$. The mass at $B \to \eta_c K_S$were obtained by mass constraint fit. The number of all signal and background events are normalized to that at the luminosity of 100fb^{-1}. The solid histogram is signal events. The dashed one is $B^0\bar{B}^0$ and B^+B^- MC background events. The dotted one is continuum MC background events.*

Table D.5: *Results for $B \to J/\psi K_S$ MC.*

Cut	Signal	B^0B^0	B^+B^-	Continuum
Generated	1.000(eff.)	5.75×10^7	5.75×10^7	2.8×10^8
B^0 recon	0.429	14	4	15
Flavor Tagging	0.177	4	1	4
CP vertex	0.165	3	1	2
TAG vertex	0.163	3	1	2
K_S vertex	0.160	2	1	2
survived	0.160	2	1	2

Table D.6: *Results for $B \to \psi(2S)K_S$ MC.*

Cut	Signal	B^0B^0	B^+B^-	Continuum
Generated	1.000(eff.)	5.75×10^7	5.75×10^7	2.8×10^8
B^0 recon	0.316	49	21	67
Fox-Wolfram	0.314	49	20	32
Flavor Tagging	0.126	16	9	15
CP vertex	0.114	16	8	14
TAG vertex	0.109	16	8	14
K_S vertex	0.106	8	6	6
survived	0.106	8	6	6

Table D.7: *Results for $B \to \chi_{c1}K_S$ MC.*

Cut	Signal	B^0B^0	B^+B^-	Continuum
Generated	1.000(eff.)	5.75×10^7	5.75×10^7	2.8×10^8
B^0 recon	0.281	25	11	5
Fox-Wolfram	0.280	25	11	2
Flavor Tagging	0.116	7	6	2
CP vertex	0.108	7	5	2
TAG vertex	0.107	7	5	2
K_S vertex	0.104	6	3	0
survived	0.104	6	3	0

Table D.8: *Results for $B \to \eta_c K_S$ MC.*

Cut	Signal	B^0B^0	B^+B^-	Continuum
Generated	1.000(eff.)	5.75×10^7	5.75×10^7	2.8×10^8
B^0 recon	0.214	556	4406	4347
Fox-Wolfram cut	0.213	521	383	1974
Thrust angle cut	0.192	460	338	1315
Flavor tagging	0.077	177	110	403
CP-vertex	0.067	148	91	326
Tagging-vertex	0.067	147	91	324
Mass constraint fit	0.044	55	16	65
K_S vertex cut	0.043	45	11	49
η_c daughter momentum	0.043	36	6	44
survived	0.043	36	6	44

Appendix E

Reconstruction of $B \to J/\psi K^{*0}$

We have generated the MC-data events using the value of Br($B \to J/\psi K^{*0}$)=1.35×10^{-3} and $K^{*0} \to K^+\pi^-$=66.6%[46] for an integrated luminosity of 100fb^{-1}.

The K^{*0}'s were reconstructed with identified $K^\pm$ and $\pi^\mp$. The invariant mass of $K^\pm\pi^\mp$ system was required to be within 200MeV of the nominal K^{*0} mass ($M_{K^*} = 891.6MeV/c^2$) taking the wide mass width of K^{*0} (50MeV) into account. Figure E.1 shows the invariant mass distribution of K^{*0} reconstructed.

The selection criteria for J/ψ and B are the same as the case of $B \to J/\psi K_S$(Figure E.2). In the reconstruction of B^0, only J/ψ mass was constrained to nominal J/ψ mass (Figure E.3).

The criteria for the invariant mass and momentum at $\Upsilon(4S)$ rest frame are as follows;

$$
\begin{aligned}
|M_{K^*} - M_{K^\pm\pi^\mp}| &< 0.200GeV, \\
|M_{J/\psi} - M_{l^+l^-}| &< 0.025GeV, \\
|M_{B^0} - M_{J/\psi K^\pm\pi^\mp}| &< 0.025GeV, \\
0.19 < P^*_{B^0} &< 0.47GeV.
\end{aligned}
$$

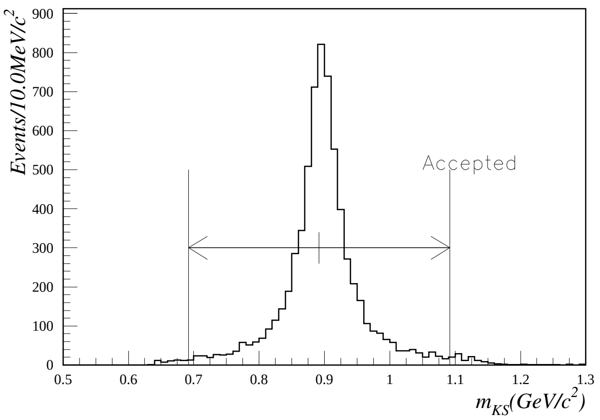

Figure E.1: *Invariant mass distribution of K^{*0} in $B \to J/\psi K^{*0}$, $K^* \to K^\pm\pi^\mp$ MC.*

In order to reduce fake K^{*0}'s from wrong combination, we took both $K^{\pm}$ and $\pi^{\mp}$ tracks originated from the J/ψ vertex requiring that the distance of closest approach be less than 500μm.

Finally 1014 events remained, which corresponds to an efficiency of 8.0%. The reconstruction efficiency is lower than that for $B \to J/\psi K_S$ since particle identification was required for both $K^{\pm}$ and $\pi^{\mp}$ from K^{*0}. The background events were simulated with smearing simulator and 26 events remained for $B^0\bar{B}^0$ and B^+B^- events. Since the S/N ratio was quite high ($\sim$ 40), we ignored these backgrounds. The continuum background was estimated to be also small.

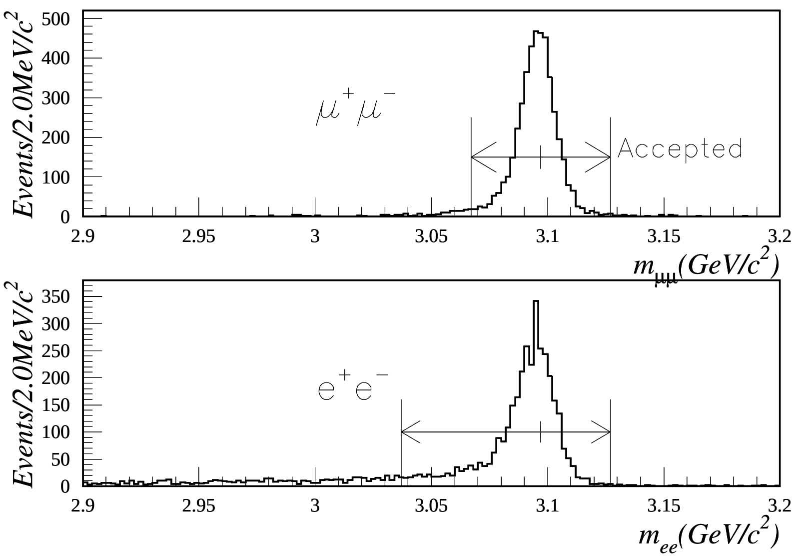

Figure E.2: *Invariant mass distribution of J/ψ in $B \to J/\psi K^{*0}$, $K^* \to K^{\pm}\pi^{\mp}$ MC.*

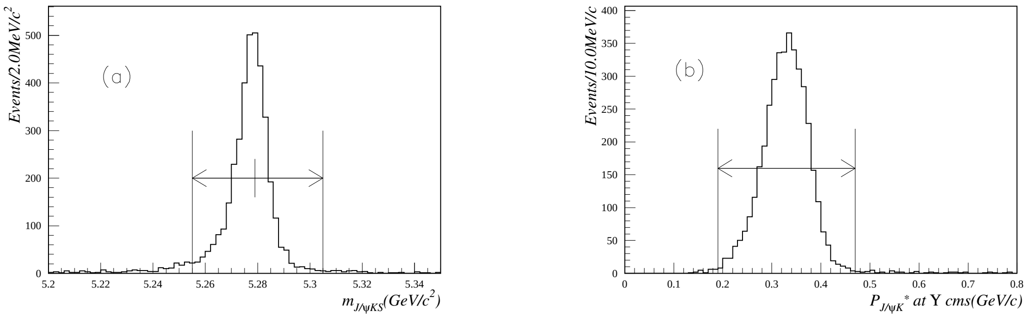

Figure E.3: *The distribution of invariant mass and momentum at $\Upsilon(4S)$ rest frame of B in $B \to J/\psi K^{*0}$, $K^* \to K^{\pm}\pi^{\mp}$ MC.*

Appendix F

Result of CP fitting

F.1 Estimation of the decay time and CP asymmetry of background

We fitted the Δz distribution of background events for all modes in MC-data. We have already shown the fitting of decay time distribution of background for $B \to J/\psi K_S$ in Figure 8.3. Figure F.1 shows the fitting results. In the figures, the distribution of events tagged by B^0 was inverted and added to events tagged by $\bar{B}^0$. In this way a systematic shift of the Δz distribution is canceled out in the fitting.

F.2 Results of fit to calculate $\sin 2\phi_1$

We have already shown the fitting of proper time distribution for $B \to J/\psi K_S$ in Figure 8.6. For all signal modes, Figure F.2 and F.3 show the fitting of proper time distribution of selected events. We performed fitting for each signal mode, $B \to J/\psi K_S$, $B \to \psi(2S)K_S$, $B \to \chi_{c1}K_S$ and $B \to \eta_c K_S$(Figure F.2). We calculated $\sin 2\phi_1$ for each mode.

We also performed fitting for all modes with each background function simultaneously(Figure F.3).

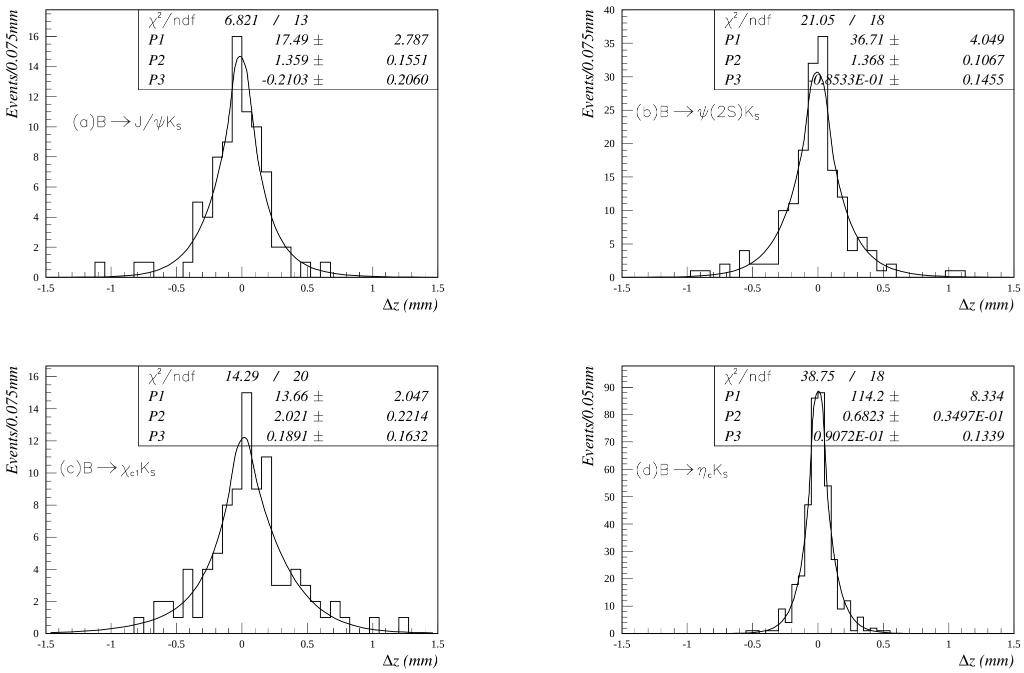

Figure F.1: *Δz distribution of the sideband events in MC-data. For (a)$B \to J/\psi K_S$, (b)$B \to \psi(2S)K_S$ and (c)$B \to \chi_{c1}K_S$, the mass and momentum sideband events are used. For (d)$B \to \eta_c K_S$, the mass sideband events are used. The distribution of events tagged by B^0 is inverted and added to events tagged by $\bar{B}^0$.*

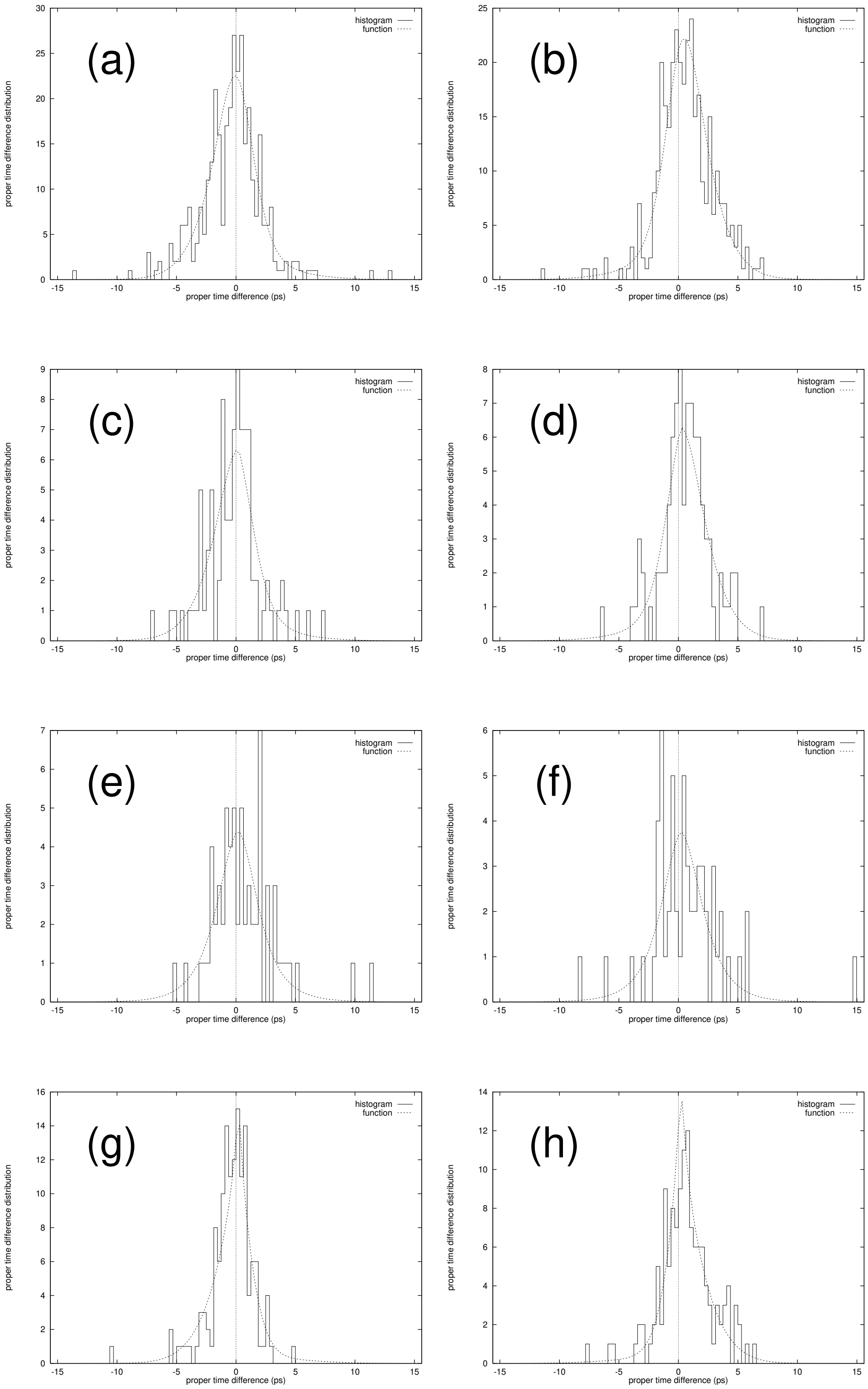

Figure F.2: CP fitting results. Fitting was performed for each signal mode. Events are tagged (a)(c)(e)(g) by B^0 and (b)(d)(f)(h) by $\bar{B}^0$ in MC-data of the following channels: (a)(b) $B \to J/\psi K_S$, (c)(d) $B \to \psi(2S) K_S$, (e)(f) $B \to \chi_{c1} K_S$, (g)(h) $B \to \eta_c K_S$.

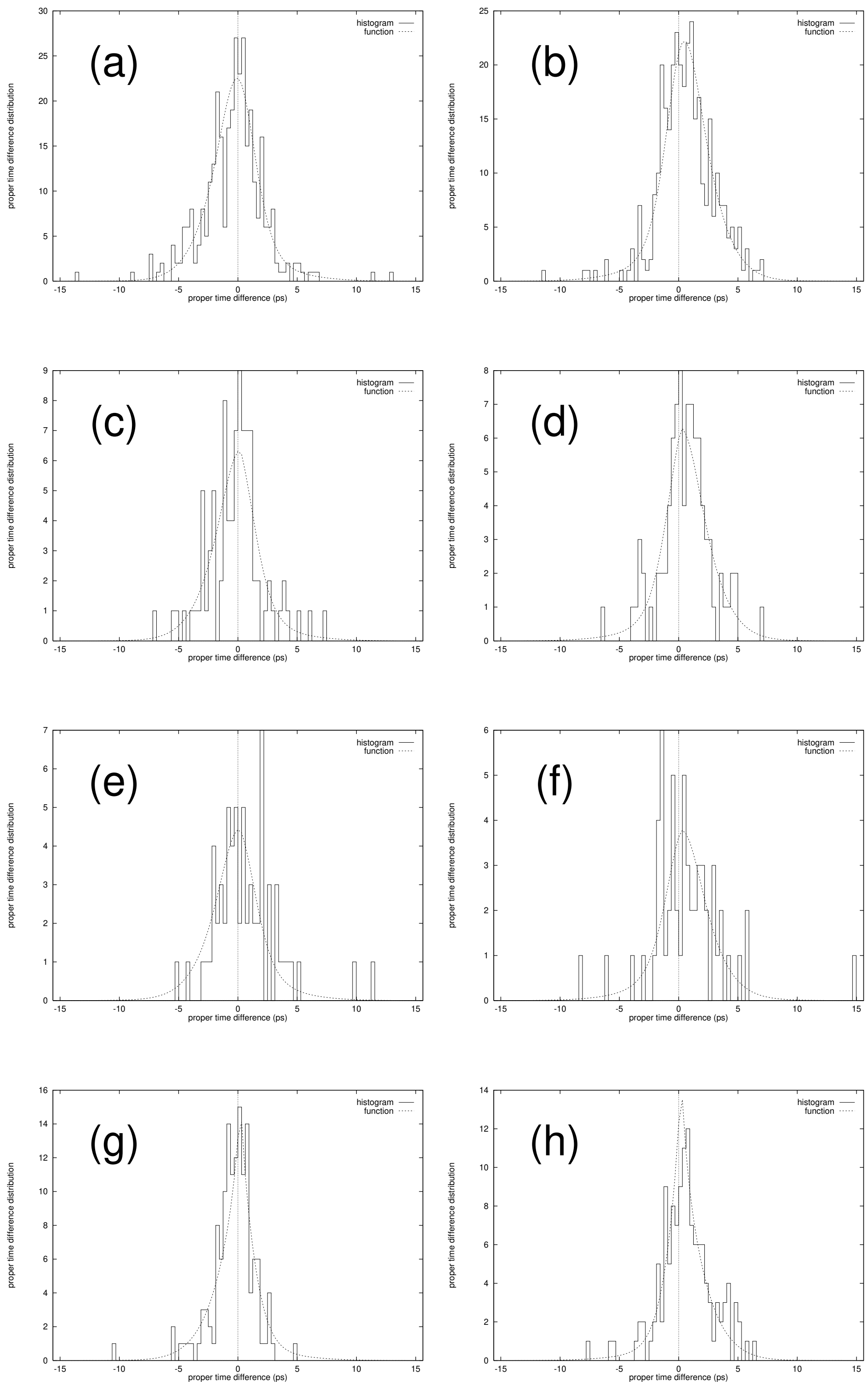

Figure F.3: CP fitting result for the all modes combined. All distributions were fitted simultaneously. Events were tagged (a)(c)(e)(g) by B^0 and (b)(d)(f)(h) by $\bar{B}^0$ in MC-data of the following channels: (a)(b) $B \to J/\psi K_S$, (c)(d) $B \to \psi(2S) K_S$, (e)(f) $B \to \chi_{c1} K_S$, (g)(h) $B \to \eta_c K_S$.

Bibliography

[1] A. D. Sakharov, JETP Lett. 5, 24 (1967).

[2] J. H. Christensen *et al.*, Phys. Rev. Lett. **13**, 138 (1964).

[3] S. Weinberg, Phys. Rev. Lett. **19**, 1624 (1967).

[4] S. Weinberg, Phys. Rev. Lett. **37**, 657 (1976).

[5] M. N. Mohapatra and J. C. Pati, Phys. Rev. *D11*, 566 (1975); J. C. Pati and A. Salam, Phys. Rev. *D10*, 275 (1974).

[6] I. I. Bigi and F. Gabbiani, Nucl. Phys. *B352*, 309 (1991).

[7] M. Kobayashi and T. Maskawa, Prog. Theor. Phys. **49**, 652 (1973).

[8] A. Carter and A. I. Sanda, Phys. Rev. Lett. **45**, 952 (1980); Phys. Rev. **D23**, 1567 (1981); I. I. Bigi and A. I. Sanda, Nucl. Phys. **193**, 851 (1981).

[9] P. Oddone, Proceedings of the UCLA Workshop: Linear Collider $B\bar{B}$ Factory Conceptual Design, edit by D. Stork, World Scientific, 243 (1987).

[10] The BaBar collaboration, Technical Design Report, (1995).

[11] T.Lohse *et al.*, DESY-PRC 94/02, (1994).

[12] "The CDF II Detector, Technical Design Report", FERMILAB-Pub-96/390-E, November 1996;The D0 Upgrade: "The Detector and its Physics", FERMILAB-Pub-96/357-E, October 1996.

[13] LHC-B Letter of Intent, CERN/LHCC 95-5, LHCC/18, August 1995.

[14] W. Pauli, In Niehls Bohr and the Development of Physics, Oxford, Pergamon 2nd edition (1955).

[15] T. D. Lee and C. N. Yang, Phys. Rev. **104**, 254 (1956).

[16] M. A. Shifman, A. I. Vainshtein and V. I. Zakharov, Nucl. Phys. **B120**, 316 (1977).

[17] M. Bander, D. Silverman and A. Soni, Phys. Rev. Lett. **43**, 242 (1979).

[18] D. London and R. D. Peccei, Phys. Lett. **B223**, 257 (1989).

[19] M. Gronau, Phys. Rev. Lett. **63**, 1451 (1989).

[20] B. Grinstein, Phys. Lett. **B229**, 280 (1989).

[21] Peter Shawhan, talk given for the new result of KTeV experiment at "Wine and Cheese Seminar at Fermilab", February 24, 1999: The result solved the problem at the results of the previous two experiments; L. K. Gibbons *et al.* (E731 Collaboration) Phys. Rev. Lett. **70**, 1203 (1993); G. D. Barr *et al.* (NA31 Collaboration), Phys. Lett. **B317**, 233 (1993).

[22] R. Aleksan, to appear in: Proceedings of the International Europhisics Conference on High Energy Physics, Brussels, Belgium, September 1995.

[23] I. Dunietz and J. L. Rosner, Phys. Rev. **34**, 1404 (1986).

[24] C. Jarlskog, in: CP Violation, edit by C. Jarlskog (World Scientific, Singapore, 1989).

[25] C. Jarlskoog, Phys. Rev. Lett. **55**, 1039 (1985); Z. Phys. C **29**, 491(1985).

[26] L. Wolfenstein, Phys. Rev. Lett. **51**, 1945 (1983).

[27] H. Albrecht *et al.* (ARGUS Collaboration), Phys. Lett. **B234**, 409 (1990); **B255**, 297 (1991).

[28] R. Fulton *et al.* (CLEO Collaboration), Phys. Rev. Lett. **64**, 16 (1990).
J. Bartelt *et al.* (CLEO Collaboration), Phys. Rev. Lett. **71**, 4111 (1993).

[29] A. J. Buras, M. Jamin, and P. H. Weisz, Nucl. Phys. **B347**, 491 (1990).

[30] T. Inami and C. S. Lim, Prog. Theor. Phys. **65**, 297 and 1772 (1981); A. J. Buras, Phys. Rev. Lett. **46**, 1354 (1981).

[31] M. Neubert, Phys. Rev. **D51**, 5101 (1995).

[32] S. Stone, in: B decays, edit by S. Stone (World Scientific, Singapore, 1994).

[33] A. Abada *et al.*, Nucl. Phys. **B376**, 172 (1992).

[34] A. J. Buras and M. K. Harlander, in: Heavy Flavours, edited by A. J. Buras and M. Lindner (World Scientific, Singapore, 1992), p. 58.

[35] J. Alexander, talk given at 29th International Conference on High Energy Physics in Vancouver, July 22-29, (1998).

[36] C. Sachradja, "Heavy Flavour Physics", XVIII International Symposium on Lepton and Photon Interactions, July 1997, Hamburg, Germany.

[37] G.D.Barr *et al.* (NA31 Collaboration), Phys. Lett. **B317**, 233 (1993).

[38] L. K. Gibbons *et al.* (E731 Collaboration), Phys. Rev. Lett. **70**, 1203 (1993).

[39] G. Buchalla, A. J. Buras, and M. K. Harlander, Nucl. Phys. **B337**, 313 (1990).

[40] S. Chan *et. al.* (OPAL Collaboration), CLEO CONF 98-24 (1998).

[41] D. S. Hwang, G. H. Kim, Z. Phys. **C76**, 107 (1997).

[42] N. G. Deshpande and J. Trampetic, Phys. Lett. **B339**, 270 (1994).

[43] I. Dunietz, Phys. Rev. **D43**, 2193 (1991).

[44] M. S. Alam *et. al.* (CLEO Collaboration), Phys. Rev. **D50**, 43 (1994).

[45] M. Ciuchini *et. al.*, Phys. Rev. Lett. **79**, 978 (1997).

[46] Review of Particle Physics, C. Caso *et al*, The European Physics Journal, **3**, 1 (1998).

[47] K. Ackerstaff *et al.* (OPAL Collaboration), CERN-EP-98-001, Jan 1998.

[48] F. Abe *et al.* (CDF Collaboration), FERMILAB-PUB-98-189-E, Jun 1998.

[49] "KEKB B-Factory Design Report", KEK Report 95-7, (1995).

[50] BELLE Collaboration, "Technical Design Report", KEK Report 95-1.

[51] K. Emi, PhD thesis, Tokyo University of Agriculture and Technology, March 1996.

[52] BELLE Collaboration, "BELLE Progress Report", KEK Report 96-1.

[53] R. Suda, PhD thesis, Tokyo Metropolitan University, February 1998.

[54] BELLE Collaboration, "BELLE Progress Report", KEK Report 97-1.

[55] A. S. Kuzmin *et al.*, Nucl. Instr. and Meth. **A379**, 491 (1996).

[56] A. Satpathy, PhD thesis, Utkal University, Bhubaneswar, India, October 1998.

[57] A. S. Schwarz, Phys. Rept. **238**, (1994).

[58] "BELLE SVD Technical Design Report": http://bsunsrv1.kek.jp/ svd/tdr/tdr.ps, (1998).

[59] V. Chabaud *et al.*, Nucl. Instr. and Meth. **A368**, 314 (1996).

[60] Hamamatsu Photonics., Si Photodiodes and Charge Sensitive Amplifiers for Scintillation Counting and High Energy Physics., January (1997).

[61] IDE AS company, Oslo, Norway.

[62] K. Adachi, Master thesis, Osaka University, February 1995.

[63] H. Hanai *et al.*, Nucl. Inst. and Meth. **A314**, 455 (1992).

[64] M. Hazumi *et al.*, IEEE NSS 233-18, October 1995.

[65] R. Turchetta Nucl. Instr. and Meth. **A335**, 44 (1993).

[66] G. R. Lynch Nucl. Instr. and Meth. **B58**, 6 (1991).

[67] H. Ozaki, BELLE internal note No. 166 (1995).

[68] O. Toker *et al.*, Nucl. Inst. and Meth. **A340**, 572 (1994).

[69] T. Kawasaki, BELLE internal note No. 66 (1995).

[70] S. Nagayama, "Panther User's Manual": http://bsunsrv1.kek.jp/ nagayama/panther/ , (1996).

[71] GEANT Detector Description and Simulation Tool, CERN Program Library Long Writeup W0513.

[72] H. Ozaki, BELLE internal note No. 99 (1996).

[73] "CLEO software document home page": http://www.lns.cornell.edu/public/CLEO/soft/QQ/index.html, (1998).

[74] T. Sjštrand, CERN-TH **93-7112** (1993).

[75] T. Sjštrand, Comp. Phys. Comm. **39**, 347 (1986).

[76] B. Andersson, G. Gustafson, G. Ingelman and T. Sjöstrand, Phys. Rep. **97**, 31 (1983).

[77] C. Peterson *et al.*, Phys. Rev. **D27**, 105 (1983).

[78] K. L. Brown and Ch. Iselin, DECAY TURTLE, CERN Program Library Long Writeup, CERN 74-2.

[79] S. M. Selzer and M. J. Berger, Technical Report SP3012, NASA, (1964).

[80] P. V. Vavilov, Soviet Physics JETP, 5, 749 (1957); B. Schorr, Comp. Phys. Comm. 7, 216 (1974).

[81] P. A. Aarnio *et al.*, Fluka user's guide, Technical Report TIS-RP-190, CERN, (1987,1990).

[82] S. Nagayama, BELLE internal note No. 37 (1994).

[83] K. Neichi, BELLE internal note No. 48 (1995).

[84] M. Tomoto, Master thesis, Nagoya University, February 1996; T. Takegai, Master thesis, Osaka University, February 1997.

[85] R. K. Bock, H. Grote, D. Notz and M. Regel,"Data analysis techniques for high-energy physics experiments", (Cambridge University Press, U.K.).

[86] R. E. Kalman, Tras. ASME, J. Bas. Eng. 82D 35(1960); and R. E. Kalman and R. S. Bucy, Trans. ASME, J.Bas. Eng. 83D 95(1961).

[87] P. Billoir and S. Qian, Nucl. Instr. Meth **A294** 219(1990); P. Billoir and S. Qian, Nucl. Instr. Meth **A295** 492(1990);

[88] T. Houjo, Master thesis, Osaka university, February 1999.

[89] T. Nozaki, BELLE internal note No. 79 (1995).

[90] A. G. Frodesen *et al.*, "Probability and Statistics in Particle Physics," Universitesforlaget, p.217.

[91] T. A. Armstrong *et al*, Phys. Rev. **D52**(1995), 4839

[92] R. M. Baltrusaitis *et al.* (MARK III Collaboration), Phys.Rev. **D33**, 629 (1986).

[93] H. Albrecht *et al.* (ARGUS Collaboration), Phys.Lett. **B338**, 390 (1994).

[94] D. Bisello *et al.* (DM2 Collaboration), Nucl.Phys. **B350**, 1 (1991).

[95] For example; Philip. R. Bevington and D. Keith. Robinson,"Data Reduction and Error Analysis for the Physical Science", McGrowHill.

[96] H. Ozaki, BELLE internal note No. 111 (1996).

[97] T. Hasuike *et al.*, Phys. Rev. **D41**, 1691 (1990).

[98] BELLE Collaboration, "Letter of Intent for the Belle Collaboration", KEK Report 94-2.

[99] Y. Grossman, Nucl. Phys. **426**, 355 (1994).

[100] S. L. Glashow and S. Weinberg, Phys. Rev. **D15**, 1958 (1977).

[101] Y. Grossman and Y. Nir, Phys. Lett. **B313**, 126 (1993).

[102] G. C. Branco, Phys. Rev. Lett. **44**, 504 (1980).

[103] Y. Grossman *et al.*, hep-ph/9701231 (1997).

[104] T. Kurimoto, Mod. Phys. Lett. **A10**, 1577 (1995).

[105] T. Goto *et al.*, Phys. Rev. **D53**, 5233 (1996).

[106] Y. Nir, hep-ph/9309325, (1993); hep-ph/9607415, (1996).

[107] S.Ichizawa, Master thesis, Tokyo Institute of Technology, February 1997.

[108] A. Ouraou, http://infodan.in2p3.fr/delphi/user/ouraou/fitver.html

[109] G. C. Fox and S.Wolfram, Nucl. Phys. **B149**, 413 (1979).

[110] S. Brandt *et al*, Phys. Lett. **12**, 57 (1964); E.Fahri, Phys. Rev. Lett. **39**, 1587 (1977).